Intense Extreme Ultraviolet Pulses for Attosecond Pump-Probe Experiments

Plach, Marius

2025

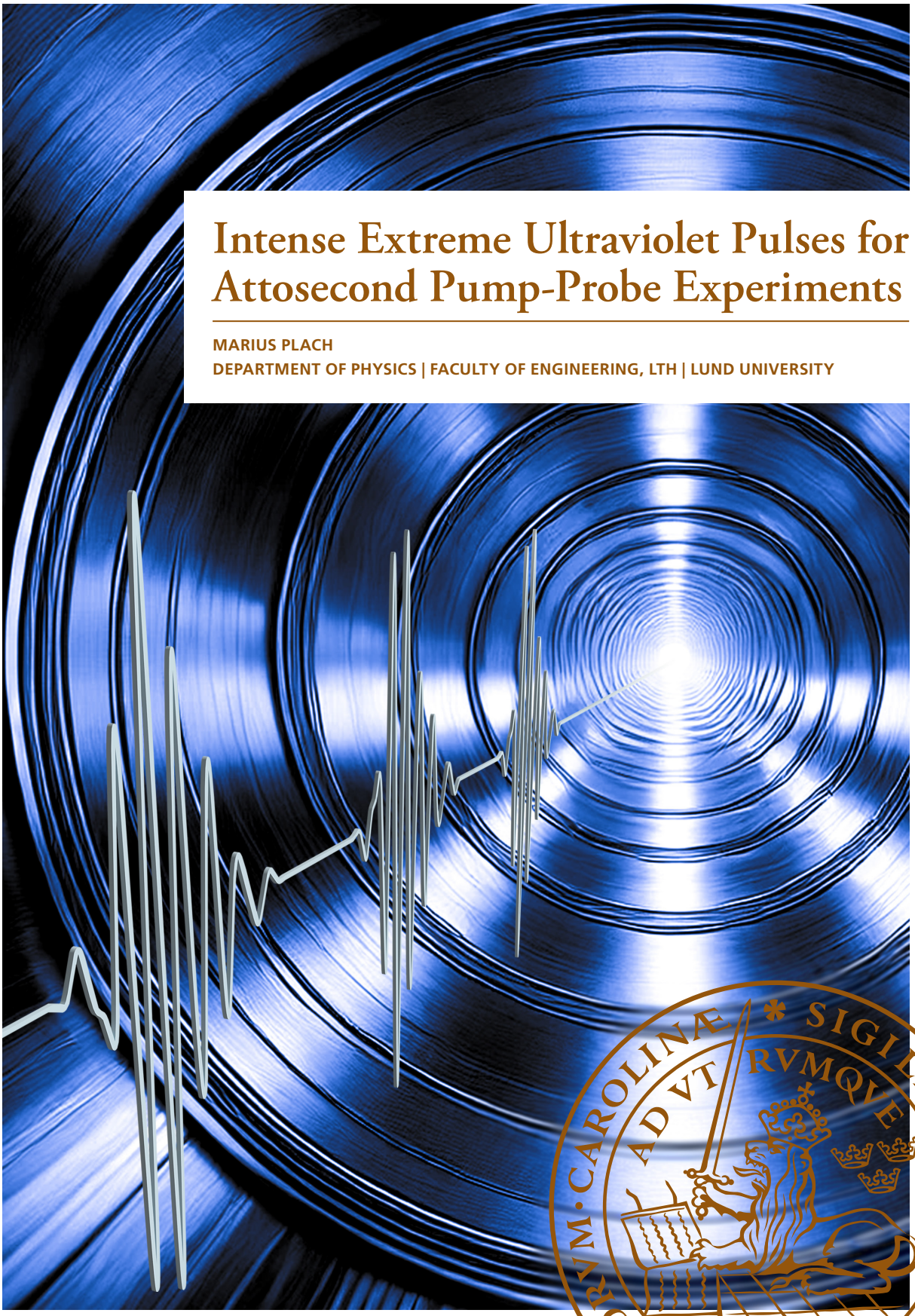

Intense Extreme Ultraviolet Pulses for Attosecond Pump-Probe Experiments

MARIUS PLACH
DEPARTMENT OF PHYSICS | FACULTY OF ENGINEERING, LTH | LUND UNIVERSITY

Intense Extreme Ultraviolet Pulses for Attosecond Pump-Probe Experiments

Intense Extreme Ultraviolet Pulses for Attosecond Pump-Probe Experiments

by Marius Plach

LUND
UNIVERSITY

Thesis for the degree of PhD in Physics
Thesis advisors: Prof. Per Eng-Johnsson, Assoc. Prof. Cord Arnold, Prof. Anne L'Huillier
Faculty opponent: Prof. Stefan Witte

To be presented, with the permission of the Faculty of Engineering, LTH of Lund University, for public criticism at Rydbergsalen (Fysikum, Professorsgatan 1, Room H418)
on Friday, 28 March 2025 at 13:15.

Organization	Document name
LUND UNIVERSITY Department of Physics Box 118 SE–221 00 LUND Sweden	**Doctoral Dissertation** Date of disputation 2025-03-28 Sponsoring organization
Author(s) Marius Plach	

Title and subtitle

Intense Extreme Ultraviolet Pulses for Attosecond Pump-Probe Experiments

Abstract

Attosecond science enables the study of ultrafast dynamics on atomic scales, providing fundamental insights into light–matter interaction. This thesis work aims to advance the development and application of an attosecond light source capable of delivering extreme ultraviolet (XUV) pulses with exceptionally high intensity.

High-order harmonic generation (HHG) is a nonlinear process where a strong laser—typically in the infrared (IR) spectral region—is focused into a gas target, producing attosecond pulses in the XUV spectral region. These pulses are commonly used in pump-probe experiments, where a pump pulse excites the system and a probe pulse interrogates the induced dynamics, allowing for time-resolved measurements of ultrafast processes.

XUV–IR pump-probe schemes investigate electron dynamics via interactions that involve a single XUV and several infrared photons. However, infrared-driven processes can add complexity to the interpretation of the induced dynamics. In contrast, XUV–XUV pump-probe schemes provide a more direct approach, in which single-photon-induced dynamics are probed by a single second photon. Reaching the regime in which two XUV photons are absorbed requires high intensities, but the inherently low conversion efficiency of HHG poses a major challenge. To overcome this limitation, generation conditions, phase-matching conditions, and the wavefront characteristics of the driving field must be optimized.

This thesis demonstrates advancements in generating intense attosecond XUV pulses by optimizing the HHG process. Additionally, it explores how generation conditions affect the harmonic focus position and waist, influencing the ability to refocus the XUV pulses to a high-intensity spot. Beyond source optimization, applications of intense attosecond pulses in XUV–XUV and XUV–IR pump-probe experiments are investigated, enabling studies of electron dynamics upon photoionization. These experiments provide new insights into photoionization and ultrafast charge migration, enhancing our understanding of attosecond dynamics.

By refining attosecond pulse generation, this thesis contributes to the next generation of high-intensity ultrafast light sources, opening new possibilities for time-resolved studies in atomic and molecular physics.

Key words

Attosecond Science, Ultrafast Science, High-Order Harmonic Generation, XUV Pulses, Photoionization Dynamics, Intense XUV Beamline

Classification system and/or index terms (if any)

Supplementary bibliographical information	Language
	English
ISSN and key title 0281-2762	ISBN 978-91-8104-396-9 (print) 978-91-8104-397-6 (pdf)
Recipient's notes	Number of pages 205 / Price
	Security classification

Intense Extreme Ultraviolet Pulses for Attosecond Pump-Probe Experiments

by Marius Plach

LUND
UNIVERSITY

A doctoral thesis at a university in Sweden takes either the form of a single, cohesive research study (monograph) or a summary of research papers (compilation thesis), which the doctoral student has written alone or together with one or several other author(s).

In the latter case the thesis consists of two parts. An introductory text puts the research work into context and summarizes the main points of the papers. Then, the research publications themselves are reproduced, together with a description of the individual contributions of the authors. The research papers may either have been already published or are manuscripts at various stages (in press, submitted, or in draft).

Cover illustration front: Extreme ultraviolet attosecond pulses propagating through a vacuum tube. Background generated with DALL·E; E-field overlay from MATLAB simulations, with amplitudes and phases derived from experiment.

Funding information: The thesis work was financially supported by the Helmholtz Foundation through the Helmholtz-Lund International Graduate School (HELIOS, HIRS-0018).

Use of Artificial Intelligence: Certain aspects of the writing, idea development, and text refinement of this thesis were assisted by generative language models. The final interpretation, analysis, and conclusions presented in this work remain the sole responsibility of the author.

Faculty of Engineering, LTH, Department of Physics, Division of Atomic Physics

Lund Reports on Atomic Physics, LRAP 607 (2025)
ISBN: 978-91-8104-396-9 (print)
ISBN: 978-91-8104-397-6 (pdf)
ISSN: 0281-2762

Printed in Sweden by Media-Tryck, Lund University, Lund 2025

Abstract

Attosecond science enables the study of ultrafast dynamics on atomic scales, providing fundamental insights into light–matter interaction. This thesis work aims to advance the development and application of an attosecond light source capable of delivering extreme ultraviolet (XUV) pulses with exceptionally high intensity.

High-order harmonic generation (HHG) is a nonlinear process where a strong laser—typically in the infrared (IR) spectral region—is focused into a gas target, producing attosecond pulses in the XUV spectral region. These pulses are commonly used in pump-probe experiments, where a pump pulse excites the system and a probe pulse interrogates the induced dynamics, allowing for time-resolved measurements of ultrafast processes.

XUV–IR pump-probe schemes investigate electron dynamics via interactions that involve a single XUV and several infrared photons. However, infrared-driven processes can add complexity to the interpretation of the induced dynamics. In contrast, XUV–XUV pump-probe schemes provide a more direct approach, in which single-photon-induced dynamics are probed by a single second photon. Reaching the regime in which two XUV photons are absorbed requires high intensities, but the inherently low conversion efficiency of HHG poses a major challenge. To overcome this limitation, generation conditions, phase-matching conditions, and the wavefront characteristics of the driving field must be optimized.

This thesis demonstrates advancements in generating intense attosecond XUV pulses by optimizing the HHG process. Additionally, it explores how generation conditions affect the harmonic focus position and waist, influencing the ability to refocus the XUV pulses to a high-intensity spot. Beyond source optimization, applications of intense attosecond pulses in XUV–XUV and XUV–IR pump-probe experiments are investigated, enabling studies of electron dynamics upon photoionization. These experiments provide new insights into photoionization and ultrafast charge migration, enhancing our understanding of attosecond dynamics.

By refining attosecond pulse generation, this thesis contributes to the next generation of high-intensity ultrafast light sources, opening new possibilities for time-resolved studies in atomic and molecular physics.

Popular Science Summary

Studying the interplay of light, time, and matter has fascinated humankind for millennia. As early as 2000 BCE, the ancient Egyptians made this connection by harnessing the Sun's light and tracking the shadows cast by obelisks. They observed how the position of these shadows correlated with time, enabling predictions and shaping their understanding of natural cycles.

In modern times, attosecond science takes this exploration of light and time to an entirely new level. Ultrashort light pulses—lasting mere attoseconds—are used to investigate light–matter interactions with extraordinary precision. To extend the Egyptian analogy: the attosecond flashes of light replace the Sun, atoms and molecules take the place of the obelisks, and the "shadows" observed help scientists predict the timing of ultrafast events. The key difference? The timescales are unimaginably shorter.

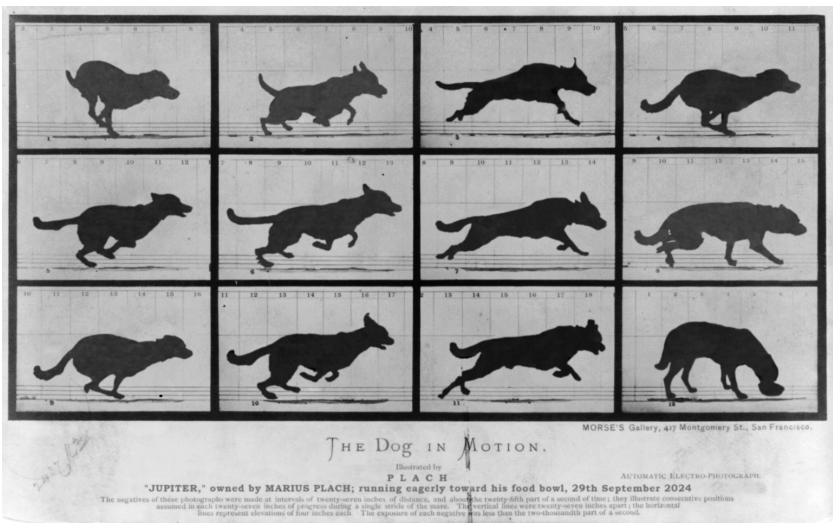

Figure 1: The Dog in Motion. Modified image based on *The Horse in Motion* (1878), Library of Congress, Prints and Photographs Division. Observing very fast processes requires tools that operate on the same timescale as the events themselves. Increasing the number of images captured per second allows the dog's movement to be observed with greater detail.

How short? To put it into perspective, the relationship between one attosecond and one second is the same as that between a second and the entire age of the universe. In attosecond science, this extreme shortness enables scientists to study processes that occur on the atomic timescale, such as electron motion, the breaking or formation of molecular bonds, and photon absorption. These processes, previously assumed to occur instantaneously, can now be observed in a time-resolved manner.

To investigate processes with high temporal resolution, capturing fine details within

a short time span is essential. A useful analogy is the recording of a running dog in motion. Just as a film captures multiple frames per second to record the details of the dog's gait, attosecond pulses enable the observation of atomic-scale "frames" of events that occur in femtoseconds—1,000 times longer than an attosecond. Figure 1 illustrates this concept with a high-speed sequence of a dog in motion.

Attosecond pulses are created through a phenomenon that can be compared to the interference of ocean waves. When waves of different frequencies travel through the sea, they sometimes align to form a large peak at a specific moment. Similarly, a broad range of light waves can overlap in time, producing a single attosecond pulse when their peaks align. This interplay of overlapping light waves is shown in Figure 2.

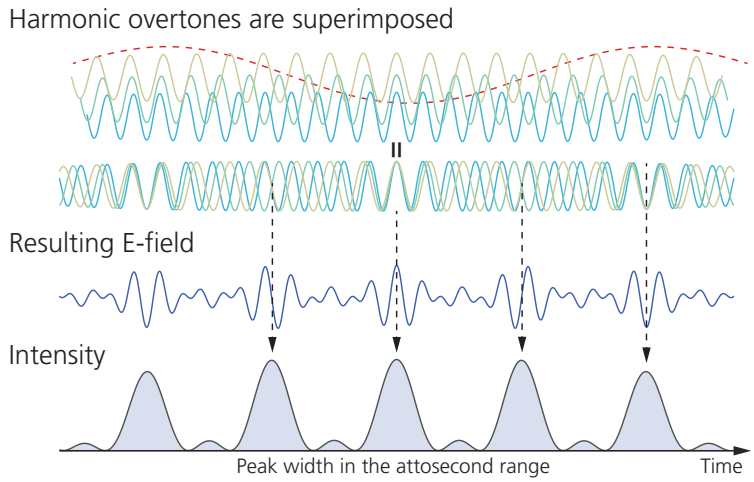

Figure 2: Creation of Attosecond Pulses. The overlap of multiple oscillations, known as overtones, at specific points in time produces an ultrashort attosecond light pulse.

This thesis focuses on the characterization and optimization of an attosecond light source. These ultrashort pulses enable experiments on photoionization, providing a platform to investigate fundamental processes in light–matter interaction. The distinctiveness of this work lies in the generation of pulses with exceptionally high intensity, which is essential for observing processes that cannot occur at lower intensity levels.

Populärvetenskaplig sammanfattning

Att studera samspelet mellan ljus, tid och materia har fascinerat mänskligheten i årtusenden. Redan omkring år 2000 f.v.t. gjorde de forntida egyptierna denna koppling genom att använda solens ljus och följa de skuggor som kastades av obelisker. De observerade hur skuggornas position förändrades över tid, vilket gjorde det möjligt att förutsäga naturens cykler och samtidigt formade deras förståelse av dem.

I modern tid tar attosekundvetenskapen denna utforskning av ljus och tid till en helt ny nivå. Ultrakorta ljuspulser—som varar blott attosekunder—används för att undersöka ljus–materia–interaktioner med enastående precision. För att fortsätta den egyptiska analogin: attosekundens ljusblixtar ersätter solen, atomer och molekyler tar obeliskernas plats, och de ”skuggor” som observeras hjälper forskare att förutsäga tidpunkten för ultrasnabba händelser. Den stora skillnaden? Tidsskalorna är ofattbart mycket kortare.

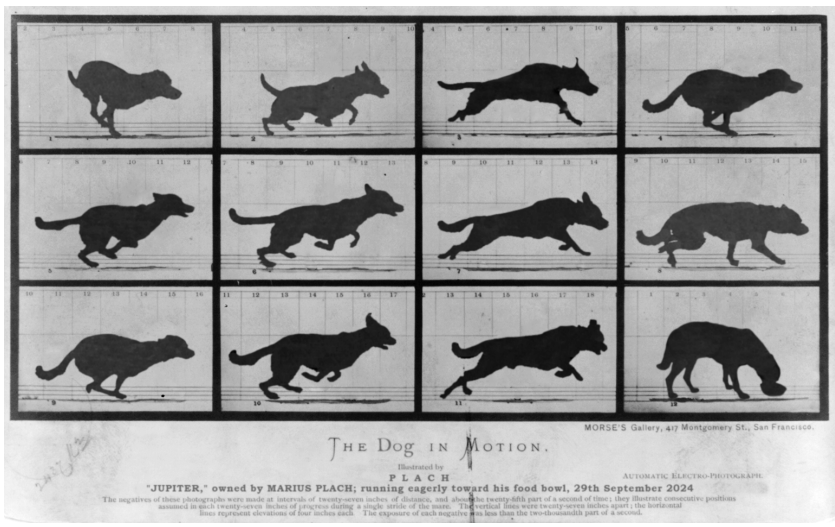

Figure 3: The Dog in Motion. Modifierad bild baserad på *The Horse in Motion* (1878), Library of Congress, Prints and Photographs Division. För att observera mycket snabba processer krävs verktyg som verkar på samma tidsskala som händelserna själva. Genom att öka antalet bilder som fångas per sekund kan hundens rörelser observeras med större detaljrikedom.

Hur korta då? För att sätta det i perspektiv: förhållandet mellan en attosekund och en sekund är detsamma som mellan en sekund och hela universums ålder. Inom attosekundvetenskapen gör denna extremt korta tid det möjligt att studera processer på atomär tidsskala, såsom elektronrörelser, bindningsbrott och bindningsbildning i molekyler samt fotonabsorption. Dessa processer, som tidigare antogs ske omedelbart, kan nu observeras på ett tidsupplöst sätt.

För att undersöka processer med hög tidsupplösning är det nödvändigt att fånga detaljer inom mycket korta tidsintervall. En användbar analogi är inspelningen av en springande hund i rörelse. Precis som en film spelar in flera bilder per sekund för att fånga detaljer i hundens rörelsemönster, möjliggör attosekundspulser observation av ”bilder” på atomär skala av händelser som sker på femtosekundsskalan—vilket är 1 000 gånger längre än en attosekund. Figur 3 illustrerar detta koncept med en högupplöst sekvens av en hund i rörelse.

Attosekundspulser skapas genom ett fenomen som kan liknas vid interferens av havsvågor. När vågor med olika frekvenser färdas genom havet, kan de stundtals sammanfalla och bilda en hög topp vid ett specifikt ögonblick. På liknande sätt kan ett brett spektrum av ljusvågor överlappa varandra i tiden och skapa en enskild attosekundpuls när deras toppar sammanträffar. Detta samspel mellan överlappande ljusvågor visas i Figur 4.

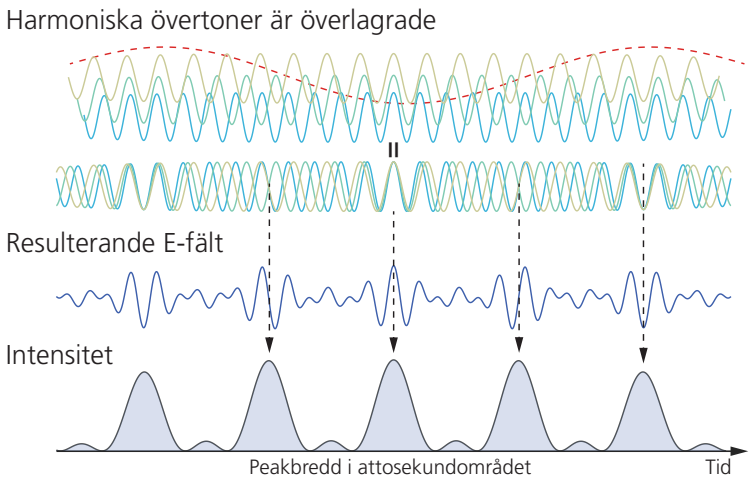

Figure 4: Skapandet av attosekundspulser. Överlappningen av flera svängningar, betecknade som övertoner, vid specifika tidpunkter genererar en ljuspuls med attosekunders varaktighet.

Denna avhandling handlar om karakterisering, optimering och tillämpning av en attosekundsljuskälla. Dessa ultrakorta pulser möjliggör experiment inom fotojonisering och erbjuder en plattform för att studera fundamentala atomära processer. Det som utmärker detta arbete är genereringen av pulser med exceptionellt hög intensitet, vilket är nödvändigt för att kunna observera processer som inte kan inträffa vid lägre intensitetsnivåer.

Populärwissenschaftliche Zusammenfassung

Seit Jahrtausenden sind die Menschen vom Zusammenspiel zwischen Licht, Zeit und Materie fasziniert. Bereits im 2. Jahrtausend v. Chr. hatten die alten Ägypter verstanden, dass sich durch den Schatten eines Obelisken, der in der Sonne steht, Zeit messen lässt. Basierend auf ihren Beobachtungen entwickelten sie Skalen, um Vorhersagen treffen und zum Beispiel Jahreszeiten verstehen zu können.

Heute sind wir durch Attosekundenforschung in der Lage in völlig neue Zeitspannen einzutauchen. Extrem kurze Lichtpulse, die nur wenige Attosekunden dauern, werden verwendet, um das Zusammenwirken von Licht und Materie zu untersuchen. Um es mit den alten Ägyptern zu vergleichen: Die Lichtpulse ersetzen die Sonne, der Obelisk wird durch Atome oder Moleküle verkörpert und die Interaktion stellt den Schatten dar – mit dem Unterschied, dass die Zeitskalen, die sich auf diese Weise untersuchen lassen, *unfassbar* kurz sind.

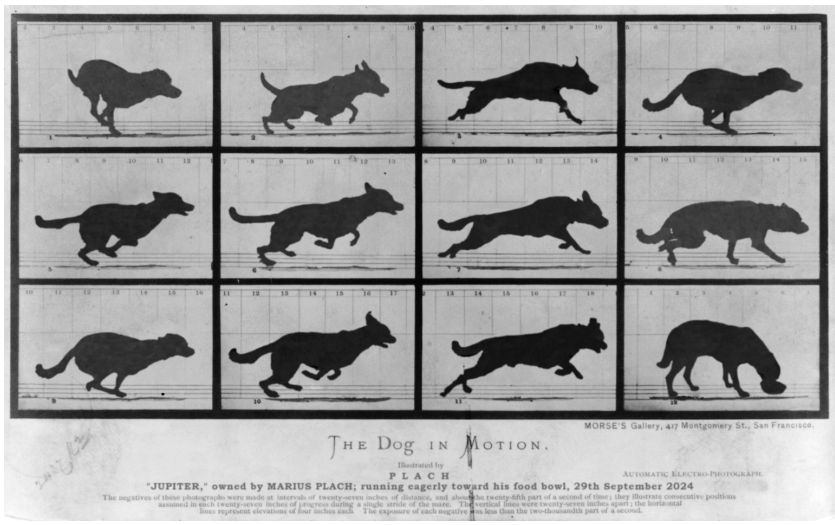

Abbildung 5: The Dog in Motion. Fotomontage basierend auf *The Horse in Motion* (1878), Library of Congress, Prints and Photographs Division. Um sehr schnelle Abläufe zu beobachten, benötigt man eine hohe zeitliche Auflösung. Je mehr Bilder pro Sekunde man für die Aufzeichnung des sprintenden Hundes verwendet, desto detaillierter lassen sich dessen Bewegungen beobachten.

Um ein Bild der Zeitskalen zu geben: Eine Attosekunde steht im Verhältnis zu einer Sekunde wie eine Sekunde zum Alter des gesamten Universums. Diese kurzen Zeitskalen erlauben es Wissenschaftlern, atomare Vorgänge wie Elektronenbewegungen, das Auseinanderbrechen und Formen von chemischen Verbindungen oder die Photonenabsorption zu beobachten. Viele dieser Prozesse galten bisher als instantan, weil sie nicht messbar waren.

Eine weitere Analogie, die das Prinzip solcher Messungen verdeutlicht, ist das Filmen eines rennenden Hundes. Je mehr Bilder pro Sekunde aufgezeichnet werden, desto genauer lassen sich Bewegungen darstellen und schnelle Abläufe erkennen, die mit dem bloßen Auge nicht zu erkennen wären. Attosekundenpulse ermöglichen die Beobachtung atomarer Vorgänge, die im Bereich von Femtosekunden ablaufen, also 1000-mal länger als eine Attosekunde. Abbildung 5 veranschaulicht dieses Konzept durch die Darstellung eines Hundes im Sprint.

Um Attosekundenpulse zu erzeugen, nutzt man ein Prinzip, das sich erklären lässt, wenn es mit dem Prinzip der Wellenüberlagerung wie zum Beispiel im Ozean verglichen wird. Verschieden große Wellen aus unterschiedlichen Richtungen können sich überlagern und besonders hohe Wellen formen. Ähnlich überlagern sich Lichtwellen verschiedener Frequenzen, wodurch extrem kurze Pulse im Attosekundenbereich entstehen. Dieser Vorgang wird in Abbildung 6 gezeigt.

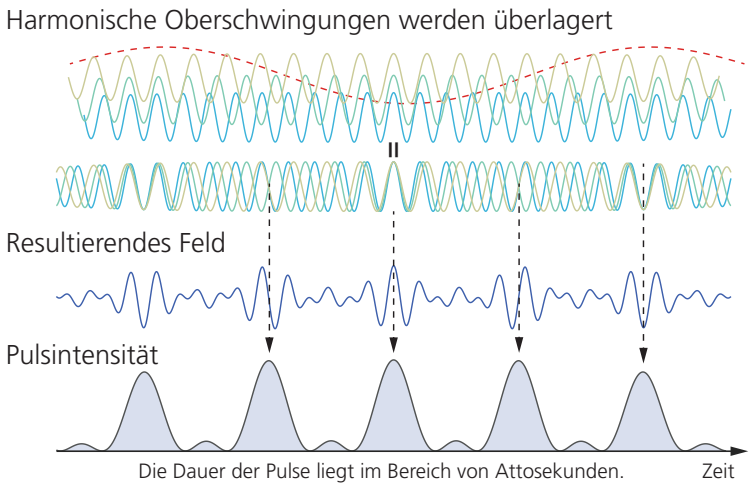

Abbildung 6: Entstehung von Attosekundenpulsen. Durch das Überlagern von harmonischen Oberschwingungen, die in bestimmter Phasenbeziehung zueinander stehen, können Pulse entstehen, deren Dauer im Attosekundenbereich liegt.

Diese Arbeit behandelt die Vermessung von verschiedenen optischen Eigenschaften einer Attosekunden-Lichtquelle und ihrer Optimierung. Darüber hinaus werden die so erzeugten ultrakurzen Pulse angewendet, um Photoionisationsexperimente durchzuführen und in der Folge Rückschlüsse auf die grundlegende Atomphysik gezogen. Das Besondere dieses experimentellen Aufbaus im Vergleich zu anderen Attosekundenexperimenten ist die Erzeugung von Pulsen besonders hoher Intensität, wodurch sich Prozesse beobachten lassen, die bei niedrigerer Intensität nicht stattfinden.

List of publications

This thesis is based on the following publications:

I **Spatial Aberrations in High-Order Harmonic Generation**

M. Plach, F. Vismarra, E. Appi, V. Poulain, J. Peschel, P. Smorenburg, D. P. O'Dwyer, S. Edward, Y. Tao, R. Borrego-Varillas, M. Nisoli, C. L. Arnold, A. L'Huillier, and P. Eng-Johnsson
Ultrafast Science, 2024, 4, 0054

II **Chromatic aberrations correction of attosecond high-order harmonic beams by flat-top spatial shaping of the fundamental beam**
K. Veyrinas, **M. Plach**, J. Peschel, M. Hoflund, F. Catoire, C. Valentin, P. Smorenburg, H. Dacasa, S. Maclot, C. Guo, H. Wikmark, A. Zaïr, V. Strelkov, C. Picot, C. Arnold, P. Eng-Johnsson, A. L'Huillier, E. Mével and E. Constant
New Journal of Physics, 2023, 25(2), 023017

III **Focusing Properties of High-Order Harmonics**

M. Hoflund, J. Peschel, **M. Plach**, H. Dacasa, K. Veyrinas, E. Constant, P. Smorenburg, H. Wikmark, S. Maclot, C. Guo, C. Arnold, A. L'Huillier, and P. Eng-Johnsson
Ultrafast Science, 2021, 2021, 797453

IV **Two phase-matching regimes in high-order harmonic generation**

E. Appi, R. Weissenbilder, B. Nagyillés, Z. Diveki, J. Peschel, B. Farkas, **M. Plach**, F. Vismarra, V. Poulain, N. Weber, C. L. Arnold, K. Varjú, S. Kahaly, P. Eng-Johnsson, and A. L'Huillier
Opt. Express, 2023, 31, pp. 31687-31697

V **Attosecond dynamics of multi-channel single photon ionization**

J. Peschel, D. Busto, **M. Plach**, M. Bertolino, M. Hoflund, S. Maclot, J. Vinbladh, H. Wikmark, F. Zapata, E. Lindroth, M. Gisselbrecht, J. M. Dahlström, A. L'Huillier, P. Eng-Johnsson
Nature Communications, 2022, 13, 5205

Paper I and Paper II have been co-authored with equal contributions from the first authors. All papers are reproduced with permission of their respective publishers.

Publications not included in this thesis:

Ultrafast dynamics of fluorene initiated by highly intense laser fields

D. Garg, P. Chopra, J. WL Lee, D. Tikhonov, S. Kumar, O. Akcaalan, F. Allum, R. Boll, A. A Butler, B. Erk, E. Gougoula, S. P Gruet, L. He, D. Heathcote, E. Jones, M. M Kazemi, J. Lahl, A. K Lemmens, Z. Liu, D. Loru, S. Maclot, R. Mason, J. Merrick, E. Müller, T. Mullins, C. C Papadopoulou, C. Passow, J. Peschel, **M. Plach**, D. Ramm, P. Robertson, D. Rompotis, A. Simao, A. L Steber, A. Tajalli, S. H Trippel, A. Tul-Noor, N. Vadassery, Ivo S Vinklarek, S. Techert, J. Küpper, A. M Rijs, D. Rolles, M. Brouard, S. Bari, P. Eng-Johnsson, C. Vallance, M. Burt, B. Manschwetus, M. Schnell
Phys. Chem. Chem. Phys., 2024, **26**, 20261-20272

Abbreviations

AI Artificial Intelligence

ATI Above Threshold Ionization

APT Attosecond Pulse Train

CPA Chirped Pulse Amplification

DDI Direct Double Ionization

DM Deformable Mirror

DVMIS Double-Sided Velocity Map Imaging Spectrometer

FEL Free Electron Laser

GDD Group Delay Dispersion

HHG High-order Harmonic Generation

MCP Micro-Channel Plate

NOPA Noncollinear Optical Parametric Amplification

OPCPA Optical Parametric Chirped-Pulse Amplification

OPA Optical Parametric Amplification

PAD Photoelectron Angular Distribution

RABBIT Reconstruction of Attosecond Beating by Interference of Two-Photon Transitions

SDU Split-and-Delay Unit

SDI Sequential Double Ionization

SFA Strong-Field Approximation

SHG Second Harmonic Generation

SNR Signal-to-Noise Ratio

SWORD Spectral Wavefront Optical Reconstruction by Diffraction

TBP Time-Bandwidth Product

TDSE Time-Dependent Schrödinger Equation

TOD Third-Order Dispersion

ToF Time of Flight

VMI Velocity Map Imaging

VMIS Velocity Map Imaging Spectrometer

XUV Extreme Ultraviolet

Contents

Part I: Thesis

Chapter 1

Introduction

Time is a fundamental dimension of evolution, and defines the duration over which physical and chemical processes take place. Investigating these processes resolved in time provides conceptual insight into their mechanisms, enabling control, optimization, or suppression of specific phenomena, benefiting applications on a macroscopic scale.

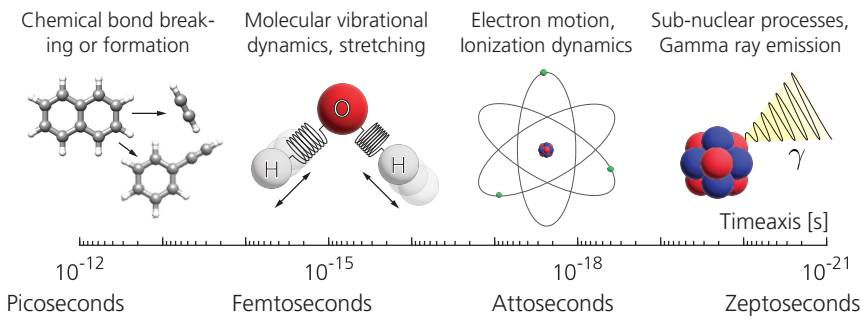

Figure 1.1: Timescales of physical and chemical processes ranging from picoseconds to zeptoseconds. Different processes occur on distinct characteristic timescales. Attosecond timescales are associated with ultrafast electron dynamics, including motion around the nucleus, photoionization, and tunneling processes.

Physical and chemical processes unfold across a wide range of timescales. Figure 1.1 illustrates examples of processes that occur over defined durations, spanning from picoseconds down to zeptoseconds.

- Picosecond and femtosecond scale: The formation and breaking of chemical bonds take place on the picosecond and femtosecond timescale, depending on the molecule size and the dissociation process. The example in the figure shows

the bond-breaking and fragmentation of naphthalene into acetylene-benzene and acetylene occurring within approximately 100 ps [1]. Molecular vibrations occur on a femtosecond scale. For example, the OH stretching of water has a frequency of $\approx 3500\,1/\mathrm{cm}$ [2], which corresponds to a period of about 10 femtoseconds.

- Attosecond scale: Electron motion within atoms, including tunneling processes and ionization dynamics, occurs on attosecond timescales. The illustrated example depicts an electron's motion around the nucleus in a classical model, where the orbital period falls within the attosecond range. For example, in hydrogen, the orbital period can be calculated to approximately 150 attoseconds.

- Zeptosecond scale: Subnuclear processes involving high-energy transitions occur on zeptosecond scales. This includes interactions within the atomic nucleus, such as gamma-ray emission during nuclear de-excitation, as illustrated in the figure. As a consequence of the energy-time uncertainty principle, the emission of a 100 keV gamma ray occurs within approximately 3.3 zeptoseconds.

Observing these processes requires tools with temporal resolutions shorter than the event's duration. Interestingly, as the temporal scale shortens, so does the spatial extent of the process, ranging from molecular oscillations at the nanometer scale to nuclear interactions within femtometers.

1.1 Historical development of short pulses

The discovery of the laser in 1960 [3] provided access to unprecedented light intensities, enabling numerous scientific breakthroughs, technological innovations, and consumer applications. It also sparked a race to produce light pulses with the highest intensity and the shortest duration. Figure 1.2 illustrates the development of the shortest laser pulse durations over time.

Shortly after the laser's discovery, several methods were developed to shorten pulse durations and increase peak intensities. In 1962 and 1964, the techniques of Q-switching and mode-locking were introduced [4, 5], serving as the key technologies for achieving progressively shorter pulse durations, with advancements continuing into the early 1980s.

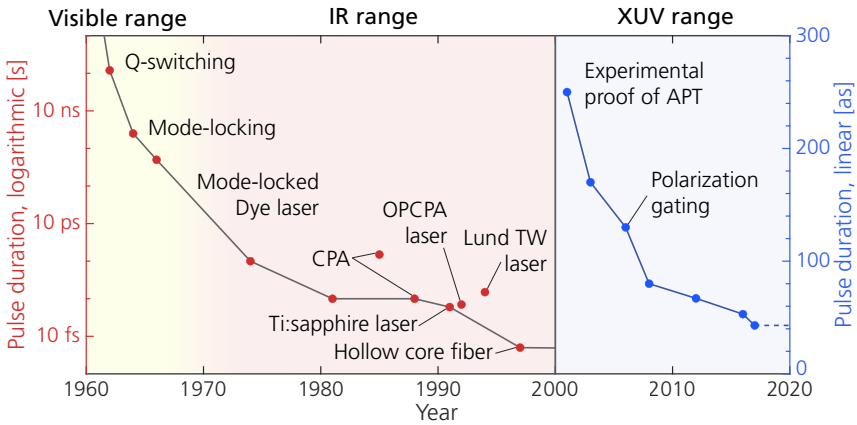

Figure 1.2: Historical development of laser pulse durations and attosecond pulses. The curve up to the year 2000 shows the progress of laser sources toward shorter pulse durations (left axis), highlighting key technological milestones, including the specifications of the Lund TW laser system in 1994 [6]. The timeline from the year 2000 onward (right axis) illustrates the development of attosecond pulses, with the first experimental proof in 2001. This is followed by multiple record-breaking achievements in generating shorter pulses, with the current shortest attosecond pulse spanning 43 as. While laser sources primarily operate in the visible and infrared (IR) spectral regions, attosecond pulses fall within the extreme ultraviolet range. Data points extracted from [3–21] in chronological order.

However, a major breakthrough came in 1985 when Strickland and Mourou introduced Chirped Pulse Amplification (CPA) [10]. This technique enabled the generation of laser intensities at unprecedented levels. Its impact was further amplified with the introduction of titanium-doped sapphire (Ti:Sapphire) as a gain medium in 1986 [22]. The combination of CPA and Ti:Sapphire quickly became the standard for ultrafast lasers due to its broad tunable bandwidth, high gain, and efficient amplification.

By the 2000s, advances in ultrafast optics brought laser amplifiers close to their fundamental limit—the duration of a single optical cycle[1]. Since then, substantial progress has been made in improving laser system stability and increasing peak power. The current highest reported peak power is 10 petawatts (PW) [23], with concepts for 100 PW lasers under active development [24].

By 2024, a total of 12 Nobel Prizes had been awarded for laser-related research and innovations [25], averaging about one every five years since the laser's initial discovery.

[1]The optical cycle duration depends on the wavelength; for instance, a $\lambda = 800\,\text{nm}$ infrared (IR) laser has a cycle duration of 2.7 femtoseconds.

1.1.1 Pathway to attosecond pulses

As ultrafast laser technology pushed pulse durations toward their fundamental limit, new methods were required to overcome this constraint. A breakthrough came with the discovery of High-order Harmonic Generation (HHG). Figure 1.3 illustrates the concept: a high-intensity laser is focused into a gas medium, where strong-field interactions generate odd-order harmonics of the driving laser frequency ω. In 1987 and 1988, this phenomenon was first observed and it was reported that these harmonics reach into the extreme ultraviolet region [26, 27].

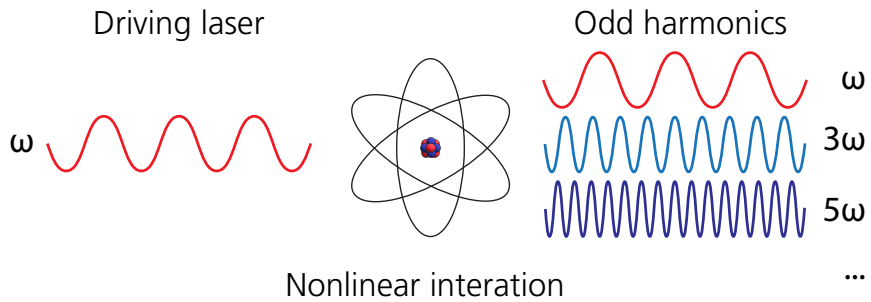

Figure 1.3: Conceptual schematics of harmonic generation. The driving laser with the frequency ω undergoes a nonlinear interaction with the atom, generating odd multiples of the incoming laser frequency, denoted as harmonics.

Additionally, in 1992, it was observed that this radiation had a duration shorter than the pump pulse [28]. Following this discovery, theories emerged to describe the underlying phenomenon [29–31], leading to predictions that this radiation could reach unprecedentedly short pulse durations in the attosecond range [32].

It was not until 2001 that the first experimental evidence of attosecond pulses was obtained [15, 33], confirming these predictions and marking the advent of attosecond science as an established research domain. The progress toward ever-shorter attosecond pulses is illustrated in Figure 1.2. The first experimental studies confirming attosecond pulse generation reported pulse trains with individual pulses as short as 250 attoseconds [15], while another study demonstrated isolated pulses of 650 attoseconds by filtering high-energy harmonics [33].

Subsequent advancements, such as the 2006 demonstration of polarization gating [17], enabled the generation of even shorter pulses by restricting high-harmonic generation to a sub-cycle window. Since then, the record for the shortest pulse has been broken multiple times, standing at 43 attoseconds since 2017 [21].

Although experiments with even higher temporal resolution in the zeptosecond range

have been reported [34], their timescale is indirectly deducted from interference, thus differing significantly from the approach used in HHG.

Attosecond science has advanced our understanding of ultrafast processes by providing tools to explore timescales that were previously assumed to be instantaneous. These advancements provide new insights into processes involving electrons, atoms, and molecules. For this reason, the contributions of Agostini, Krausz, and L'Huillier were recognized with the 2023 Nobel Prize in Physics [35], underscoring the field's importance to science.

1.2 Motivation and thesis outline

This thesis aims at advancing the development and application of an attosecond light source capable of delivering Extreme Ultraviolet (XUV) pulses with exceptionally high intensity. High-intensity XUV pulses are required to access the nonlinear regime in the XUV spectral range, where multiple photons interact simultaneously with a system. Specifically, processes such as two-XUV-photon ionization, where the combined energy of two photons overcomes the ionization barrier, become experimentally accessible.

Conventional XUV–IR pump-probe experiments often introduce additional dynamics through the IR field, complicating the interpretation of ultrafast processes. In contrast, an XUV-pump–XUV-probe scheme allows for direct investigation of the system's dynamics through purely XUV interactions, enabling unprecedented insights into ultrafast processes.

The nonlinear XUV regime is extremely challenging to access experimentally. It requires either large-scale free-electron laser facilities or specifically designed HHG sources, such as the Intense XUV Beamline in Lund. The HHG process, however, is inherently inefficient, with conversion efficiencies on the order of 10^{-5} and lower. Achieving the intensities necessary for nonlinear interactions thus demands careful optimization of the HHG process, including control over the driving laser's wavefront and intensity profile, as well as the gas medium's density and pressure distribution [36]. Additionally, tight refocusing of the generated XUV pulses is essential to reach the high intensities required for nonlinear interactions.

Chapter 2 of this thesis introduces the fundamental principles of high-harmonic generation, outlining the physical processes behind attosecond pulse generation. Attention is given to the scaling laws that govern harmonic yields and the strategies for overcoming the inherent inefficiencies of the HHG process. These foundations provide the theoretical framework for the optimization efforts described in subsequent

chapters.

Chapter 3 presents the experimental framework for high-order harmonic generation of intense XUV pulses. It begins by introducing fundamental laser amplification techniques to clarify the key differences between the decommissioned CPA system and the newly installed laser system in Lund, which was implemented during this thesis. The chapter then outlines the Intense XUV Beamline which serves as the central experimental setup for this thesis, including its pulse generation and application sections. The SYLOS GHHG LONG beamline is briefly introduced, a larger-scale facility at ELI-ALPS in Hungary at which experiments have been conducted.

Chapter 4 explores the spatial, temporal, and chromatic properties of the harmonics generated in the HHG process. Particular focus is placed on understanding the spatial beam profiles, divergence, and chromatic aberrations of the different harmonic orders as they propagate through the experimental setup. These studies provide critical insights into how the properties of the harmonics can be optimized for high-intensity applications.

Finally, Chapter 5 highlights the techniques and applications of attosecond pulses, focusing on experiments probing ultrafast electron dynamics. It begins with the methods for scan alignment and data processing, followed by pulse reconstruction and the characterization of angle-resolved photoelectron emission in XUV–IR pump-probe scans. These techniques form the basis for Paper V, where the single-photon ionization of neon has been characterized. Additionally, the chapter provides an outlook on similar measurements conducted in other noble gases. Finally, it concludes with the observation and analysis of nonlinear double ionization in neon, enabled by the use of optimized high-intensity attosecond pulses.

Chapter 2

Fundamentals of Attosecond Pulse Generation

Focusing a strong, pulsed laser into a gas medium generates radiation composed of odd-order multiples of the driving laser frequency ω. This radiation is emitted in bursts of extremely short duration, on the order of attoseconds. In this chapter, the fundamental principles and theoretical models that underlie the generation of such attosecond pulses through HHG are discussed.

2.1 High-order harmonic generation

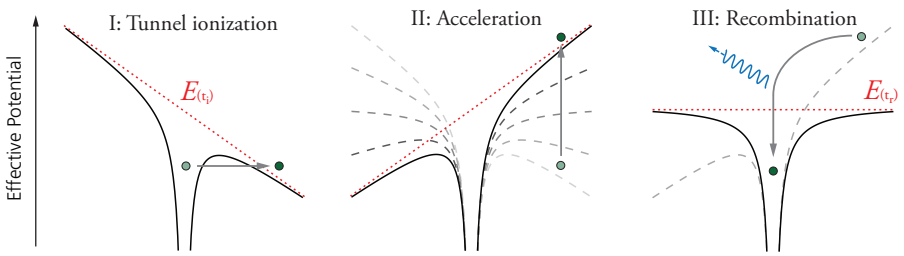

Figure 2.1: Three-step model of high-order harmonic generation: Visualization of the three-step model, with tunnel ionization (Step I), acceleration (Step II), and recombination (Step III) with photon emission. The effective potential (black solid line) represents the Coulomb potential distorted by the time-dependent laser field (red dashed line). The three graphics illustrate the sequence of events over time, shown from left to right.

The three-step model by Kulander et al. [29] and Corkum [30] is a simplified approach to describe the generation of high-order harmonics in a semiclassical picture. The

model characterizes the response of an electron bound to its parent ion when exposed to a strong laser field that meets the intensity criteria for the tunneling regime.

In the first step of the model, the electron tunnels through the Coulomb barrier (Figure 2.1, Step I). Once exposed to the laser's electric field, the electron is accelerated away from the ion (Step II). As the laser potential evolves over time, its sign switches, and the electron is accelerated back toward its parent ion. For specific ionization times, the electron can recombine with the ion, releasing the sum of kinetic energy it gained during acceleration and the ionization energy as a photon (Step III).

The electron's acceleration $\ddot{x}$ after tunneling through the potential barrier is driven by the Lorentz force:

$$m_e \ddot{x} = -eE(t) \ , \tag{2.1}$$

where m_e is the electron mass and e is the electron's charge. The laser's electric field follows $E(t) = E_0 \sin(\omega t)$, where E_0 is the amplitude of the oscillating electric field. Integrating Equation (2.1) from the ionization time t_i (when the electron first tunnels through the barrier) to time t yields the electron's velocity

$$\dot{x}(t) = \frac{eE_0}{m_e \omega} \left[\cos \omega t - \cos \omega t_i\right] \ . \tag{2.2}$$

A second integration, using the initial conditions $\dot{x}(t_i) = 0$ and $x(t_i) = 0$ (indicating no initial displacement or velocity at the time of tunneling), yields the electron's trajectory:

$$x(t) = \frac{eE_0}{m_e \omega^2} \left[\sin(\omega t) - \sin(\omega t_i) - \omega \left(t - t_i\right) \cos(\omega t_i)\right] \ . \tag{2.3}$$

The ionization time determines the electron's trajectory through the continuum; only specific ionization times allow the electron to return to the parent ion, as in other cases, it will be driven away by the field. Once in the continuum, the electron follows one of several possible trajectories that depend on both the laser intensity and ionization time. These trajectories determine the duration the electron spends in the continuum and the amount of kinetic energy it acquires until it recombines with its parent ion. Figure 2.2 shows selected electron trajectories for different ionization times within half a laser cycle.

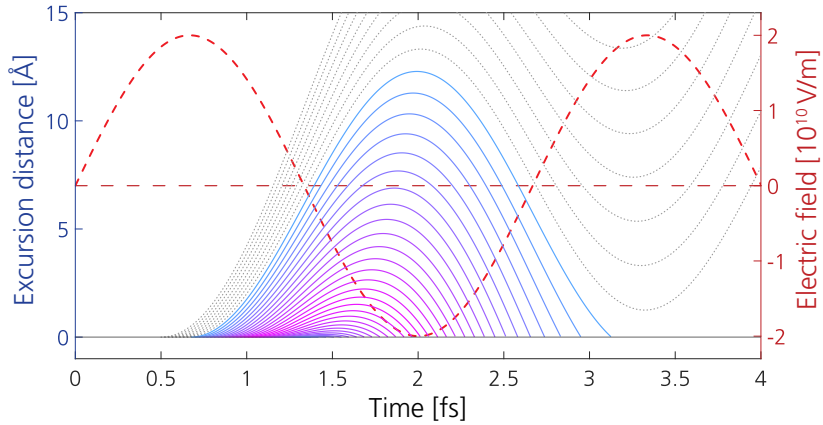

Figure 2.2: Excursion trajectories for selected ionization times. Only electrons ionized within a specific time window can recombine (colored), while the others are being driven away from their parent ion (grey dotted lines). The trajectories' energy is color-coded from blue (low kinetic energy) to purple (high kinetic energy). This pattern repeats every half cycle in both directions of the potential, though only shown here for a single half cycle as an example.

When the electron recombines, the energy it has accumulated during its excursion through the potential is released as a photon. The emitted photon's energy E_{ph} is equal to the sum of the electron's kinetic energy E_{kin} plus the atom's ionization potential I_{p}:

$$E_{\mathrm{ph}}(t_{\mathrm{r}}) = E_{\mathrm{kin}} + I_{\mathrm{p}} = \frac{1}{2}\, m_{\mathrm{e}}(\dot{x}(t_{\mathrm{r}}))^2 + I_{\mathrm{p}} \quad . \tag{2.4}$$

Figure 2.3 illustrates the electron kinetic energy as a function of ionization and recombination time for trajectories that recombine with the parent ion. The kinetic energy can be expressed in terms of ponderomotive potential $U_{\mathrm{p}} = \frac{e^2 E_0^2}{4 m_{\mathrm{e}} \omega^2}$, representing the average quiver energy of an electron in the laser field. Notably, the kinetic energy reaches a maximum, corresponding to the highest possible energy of emitted photons. This maximum photon energy is expressed by the cutoff law [37]:

$$E_{\mathrm{cutoff}} = 3.17 \frac{e^2 E_0^2}{4 m_{\mathrm{e}} \omega^2} + I_{\mathrm{p}} = 3.17 U_{\mathrm{p}} + I_{\mathrm{p}} \; . \tag{2.5}$$

The trajectories that can lead to recombination are further distinguished by the duration the electron spends in the continuum. Trajectories that recombine before reaching the 3.17 U_{p} energy peak are referred to as short trajectories, while those that recombine afterward are called long trajectories [38, 39]. In Figure 2.3, short and long trajectories are indicated by green and blue shaded areas, respectively.

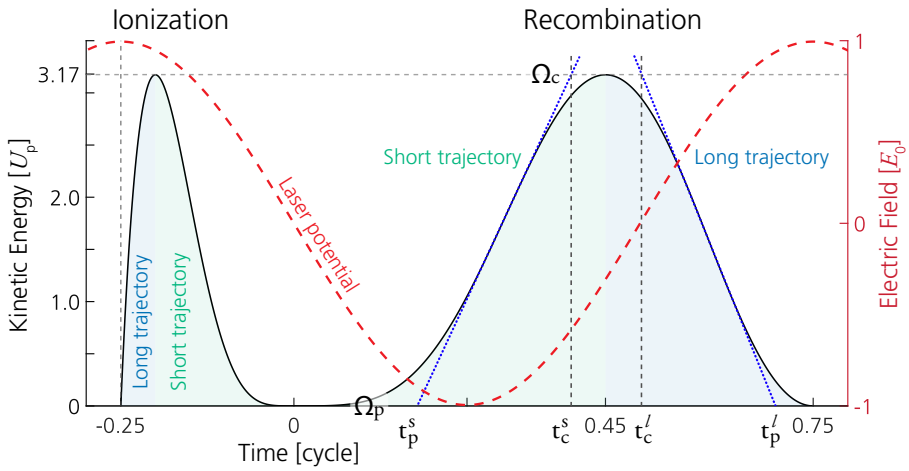

Figure 2.3: Kinetic energy as a function of recombination and ionization times: Trajectories characterized by a late ionization and early recombination times correspond to the short trajectories (green-shaded area), whereas those with early ionization and late recombination represent the long trajectories (blue-shaded). The maximum kinetic energy marks the separation between the trajectories. The blue dotted lines indicate the linear approximation for the γ-model. For reference, the laser potential is indicated by the red dashed line.

Depending on the trajectory taken, radiation of different energies is released at different times, resulting in a chirp of the emitted radiation, commonly referred to as the intrinsic attochirp [40]. Figure 2.3 illustrates that short trajectories correspond to a rising slope, where higher-energy photons are emitted later than lower-energy photons, resulting in a positive chirp. In contrast, long trajectories show the opposite behavior, where lower-energy photons are emitted later than higher-energy ones, leading to a negative chirp.

The energy-dependent continuum time determines the phase of the emitted radiation, known as the dipole phase. The dipole phase depends on the intensity of the driving laser, and its description is crucial as it influences both the temporal and spatial properties of the emitted radiation. The γ-model (see Section 2.3) provides an analytical description of the dipole phase, based on a linear approximation of the kinetic return energy function, as indicated by the blue dashed lines in Figure 2.3. Here, Ω denotes the frequency of the emitted radiation, while $t^{s,l}$ represents the return time for the short and long trajectories, respectively. The subscript specifies whether the variable corresponds to the ionization potential (p) or the cutoff (c).

At the single-atom level, recombination in the three-step model theoretically produces a spectrally broad, continuous XUV emission within each laser half-cycle. However, the electric field amplitude of the driving laser reverses signs between the two emissions within one cycle. Due to the inversion symmetry of the atom, the two emitted bursts within one cycle have a π-phase difference. As a result, only odd-order multi-

ples of the laser frequency ω constructively interfere, whereas even-order contributions cancel out. This interference between successive half-cycles gives rise to the characteristic comb-like structure in the harmonics spectrum, first observed by Ferray et al. in 1988 [27], with 2ω harmonic spacing, as visualized in Figure 2.4.

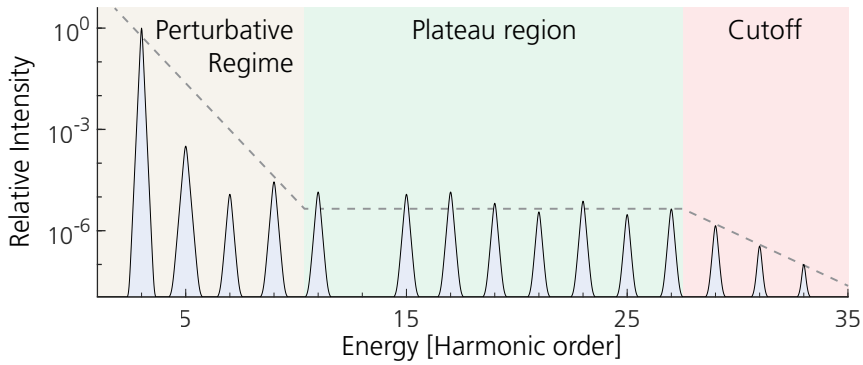

Figure 2.4: Illustration of a typical HHG emission spectrum. Characteristic comb spectrum of HHG generated in argon, showing the perturbative regime, plateau region and the harmonic cutoff. The amplitudes are extracted from [27]. The 13th order is missing as a result of reabsorption within the generation medium. Figure concept adapted from [41].

Low-order harmonics are generated during phases of the driving laser cycle when the instantaneous electric field strength is insufficient to ionize the atom, such that it remains bound and harmonic generation results from multiphoton interactions rather than strong-field tunneling or Above Threshold Ionization (ATI). In this perturbative regime, the harmonic yield rapidly decreases, scaling as I^q, with q being the harmonic order [42–44].

However, higher-order harmonics deviate from this expectation. Instead of rapidly decreasing, their intensity follows a steady distribution known as a plateau, as predicted by [37]. Perturbation theory no longer applies and harmonic generation is governed by the three-step model. These harmonics are generated during phases of the laser cycle when the instantaneous electric field strength approaches its peak, reaching a level where the atomic Coulomb barrier is sufficiently suppressed to allow tunneling ionization.

The plateau ends at the cutoff, corresponding to the maximum kinetic energy an electron can gain during its excursion in the laser field, as derived in Equation (2.5). These three distinct regimes of harmonic generation are indicated in Figure 2.4.

2.2 Strong field approximation

The semiclassical model is an intuitive approach that gives reasonable qualitative predictions for several aspects of HHG, such as ionization and return times or the photon energy at the cutoff. Yet, it is a semiclassical approximation, as for example, tunneling is a quantum mechanical phenomenon that is not described correctly in this approach.

The full quantum mechanical description is provided by the solution of the Time-Dependent Schrödinger Equation (TDSE) [45–47]. There, HHG is described as the process of a bound electron wave packet interacting with the strong laser field by tunneling through a potential wall, propagating in the continuum, and interfering with the part of the wave packet that remained in the bound state. The TDSE is expressed as

$$i\hbar\frac{\partial}{\partial t}|\Psi(t)\rangle = \hat{H}|\Psi(t)\rangle \ , \tag{2.6}$$

with $|\Psi(t)\rangle$ the electron wavefunction and the Hamiltonian $\hat{H}$,

$$\hat{H} = -\frac{\hbar^2\nabla^2}{2m_\mathrm{e}} + \hat{V}(\mathbf{r}) - e\mathbf{E}(t)\cdot\mathbf{r} \ , \tag{2.7}$$

with the electron mass m_e, the effective atomic potential $\hat{V}(\mathbf{r})$ assuming only a single electron is interacting with the driver, and the electron charge e. The first two terms describe the Hamiltonian of the electron and the atomic potential, and the third term is a time-dependent perturbation, given by the interaction with the laser electric field $\mathbf{E}(t)$. This full description with its many degrees of freedom demands a large computational effort and provides numerical results with nontrivial physical interpretation.

The Strong-Field Approximation (SFA) is a commonly used approach for numerically solving the TDSE introducing analytical approximations that simplify the complexity of the problem [48, 49]. The following assumptions are made:

I The atom is described only by its ground state.

II Ground-state depletion is neglected, as the driving laser intensity is below the saturation intensity.

III The electron in the continuum behaves as a free particle and is not affected by the atomic potential.

Using these approximations to solve the TDSE (2.6), the time-dependent dipole is used as a means to derive the emitted field. For a detailed discussion of the dipole

moment, see [49]. Here, we focus on the phase factor of the dipole moment, as this is necessary to determine the spectral and spatial characteristics of the generated harmonics. From SFA, the harmonic dipole phase $\Phi\left(t_\mathrm{i}, t_\mathrm{r}, \mathbf{p}\right)$ for a particular order q is derived from the semiclassical action integral:

$$\Phi\left(t_\mathrm{i}, t_\mathrm{r}, \mathbf{p}\right) = q\omega_0 t_\mathrm{r} - \frac{1}{\hbar}\int_{t_\mathrm{i}}^{t_\mathrm{r}} \mathrm{d}t \left\{\frac{\left[\mathbf{p} + e\mathbf{A}(t)\right]^2}{2m_\mathrm{e}} + I_\mathrm{p}\right\}, \tag{2.8}$$

with the momentum $\mathbf{p}$ and $\mathbf{A}(t)$ the vector potential and the ionization potential I_p. The dependence of the dipole phase on the laser intensity is approximately linear for both short and long trajectories, and commonly approximated by

$$\Phi^{\mathrm{s,l}} = \Phi_0^{\mathrm{s,l}} + \alpha^{\mathrm{s,l}} I \tag{2.9}$$

with the phase offset $\Phi_0^{\mathrm{s,l}}$, and $\alpha^{\mathrm{s,l}}$ the slope coefficient, which depends on the harmonic order [50].

2.3 The γ-model

To model the dipole phase without relying on numerical SFA calculations, we apply a simplified analytical approach, known as the γ-model, originally proposed in [51] and [52]. In the first step of this model, the kinetic return energy and its associated frequency, Ω, are approximated by linear relationships, as illustrated in Figure 2.3. The return time, t_r, associated with either the short or long (s/l) trajectory, is given by

$$t_\mathrm{r}^{\mathrm{s,l}}(\Omega) = t_\mathrm{p}^{\mathrm{s,l}} + \frac{t_\mathrm{c}^{\mathrm{s,l}} - t_\mathrm{p}^{\mathrm{s,l}}}{\Omega_\mathrm{c} - \Omega_\mathrm{p}}\left(\Omega - \Omega_\mathrm{p}\right) \ , \tag{2.10}$$

with the times $t_\mathrm{c}^{\mathrm{s,l}}$ / $t_\mathrm{p}^{\mathrm{s,l}}$ defined by the offset of the slope, depicted in Figure 2.3, Ω_p the frequency corresponding to the ionization potential, thus, $\hbar\Omega_\mathrm{p} = I_\mathrm{p}$, and Ω_c the frequency corresponding to the maximum electron energy.

The return time $t_\mathrm{r}^{\mathrm{s,l}}$ can also be interpreted as the group delay of the emitted radiation. The group delay is the frequency derivative of the dipole phase. Consequently, the dipole phase $\Phi^{\mathrm{s,l}}(\Omega)$ can be retrieved from the indefinite integral of the group delay over $\Omega - \Omega_p$. We derive an analytical expression for the dipole phase with the integration constant $\Phi^{\mathrm{s,l}}\left(\Omega_p\right)$:

$$\Phi^{\mathrm{s,l}}(\Omega) = \Phi^{\mathrm{s,l}}\left(\Omega_p\right) + t_p^{\mathrm{s,l}}\left(\Omega - \Omega_p\right) + \frac{t_c^{\mathrm{s,l}} - t_p^{\mathrm{s,l}}}{\Omega_c - \Omega_p}\frac{\left(\Omega - \Omega_p\right)^2}{2} \ . \tag{2.11}$$

We introduce the $\gamma^{s,l}$ constant, a parameter that describes the slope in Figure 2.3 for the cutoff case when $(\Omega_c - \Omega_p) = 3.17U_p/\hbar$. The third term of Equation 2.11 is then expressed using $\gamma^{s,l}$, which is approximated to be inversely proportional to the intensity of the driving laser I:

$$\frac{t_c^{s,l} - t_p^{s,l}}{\Omega_c - \Omega_p} = \frac{2\gamma^{s,l}}{I} , \qquad \text{where} \qquad \gamma^{s,l} = \frac{\left(t_c^{s,l} - t_p^{s,l}\right)\pi c^2 m_e}{3.17\alpha_{FS}\lambda^2} . \tag{2.12}$$

Here, α_{FS} is the fine structure constant and m_e the electron mass. We assume that the integration constant $\Phi^{s,l}(\Omega_p)$ varies linearly with the laser intensity and is expressed as $\Phi^{s,l} = \alpha^{s,l} I$. It is important to highlight that this $\alpha^{s,l}$ is not the same alpha as is commonly used within SFA theory, and it is zero for short trajectories. Using both coefficients, we express the dipole phase of the harmonic in its final form

$$\Phi^{s,l}(\Omega) = \alpha^{s,l} I + t_p^{s,l}(\Omega - \Omega_p) + \frac{\gamma^{s,l}}{I}(\Omega - \Omega_p)^2 . \tag{2.13}$$

By evaluating the coefficients for short and long trajectories, we obtain the following values for an $800\,\mathrm{nm}$ driving laser [52]:

$$\alpha^s = 0 \qquad \gamma^s = 0.22\; m_e c/(\alpha_{FS}\lambda) \tag{2.14}$$

$$\alpha^l = \alpha_{FS}\lambda^3/(2\pi m_e c^3) \qquad \gamma^l = -0.19\; m_e c/(\alpha_{FS}\lambda) . \tag{2.15}$$

In this form, the γ model offers a compact and analytically tractable expression for the dipole phase, highlighting its dependence on the laser intensity and fundamental parameters of the laser field. It is in agreement with the predictions of SFA, while avoiding extensive numerical computational effort.

2.4 Attosecond pulse trains and isolated attosecond pulses

The shortest pulse duration is determined by its spectral bandwidth, through the Time-Bandwidth Product (TBP). The TBP relates the pulse duration FWHM $\Delta\tau$ to the width of its spectral FWHM $\Delta\nu$, with shorter pulses requiring broader spectra. The TBP is expressed as:

$$\Delta\tau \times \Delta\nu \geq \text{TBP} , \tag{2.16}$$

with the TBP being a specific value that depends on the pulse shape. For a Gaussian transform-limited pulse, the value is TBP ≈ 0.44.

A single narrowband harmonic will not produce an ultrashort pulse, as illustrated in Figure 2.5 A. It will instead follow the duration of the driving laser, as long as the driver maintains an intensity that supports the non-linear effect.

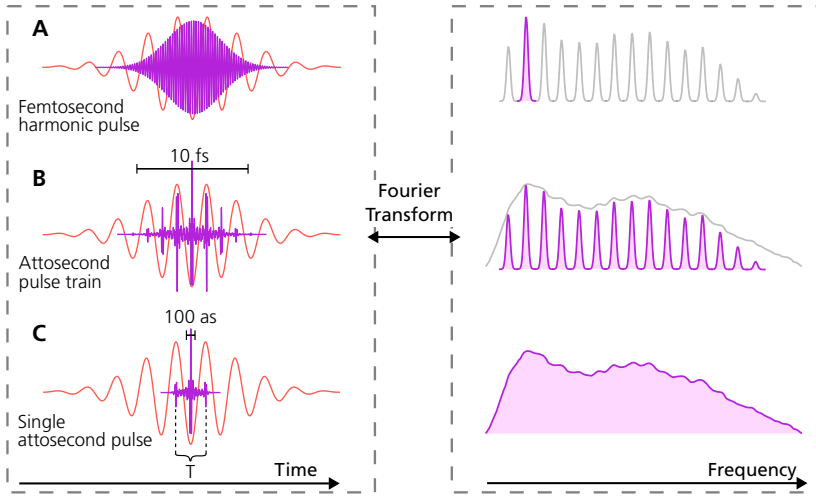

Figure 2.5: Attosecond pulse trains and isolated attosecond pulses. The time and frequency domains are related to each other via Fourier transformation. **(A)** An individual harmonic only follows the duration of the driving laser's envelope, and does not form an ultrashort pulse. **(B)** The contributions of the harmonics from the HHG frequency comb lead to the emission of an attosecond pulse train. The duration of the Attosecond Pulse Train (APT) follows the envelope of the driving laser's electric field. **(C)** Applying gating techniques broadens the individual harmonics and results in a narrow, isolated attosecond pulse. Courtesy of Robin Weissenbilder [41].

In contrast, the XUV radiation of HHG spans a broad frequency range that can result in short pulses of attoseconds. Since emission occurs once per half-cycle of the laser field (i.e., twice per full cycle), the consecutive XUV bursts interfere with one another, resulting in the comb structure with 2ω frequency spacing. In the time domain, this forms a coherent sequence of attosecond bursts separated by the half-cycle period of the laser, referred to as the APT. Figure 2.5 B illustrates how the harmonic comb structure in the frequency domain corresponds to an attosecond pulse train in the time domain.

The duration of the APT is determined by the duration of the driving laser pulse. However, the shortest possible duration of the driving laser pulse is fundamentally limited to a single optical cycle, which corresponds to 2.7 fs for a driving laser with an 800 nm wavelength. Despite this, even a single-cycle laser pulse will still produce a two-burst attosecond pulse train, as XUV emission occurs at both the rising and falling edges of the cycle.

To generate a single, isolated attosecond pulse, gating techniques must be applied to confine the harmonic emission to a single XUV burst and suppress any secondary emissions. There are various methods to achieve this, including polarization gating [17], double optical gating [53], ionization gating [54], and two-color gating [55]. These gating techniques remove the temporal periodicity in the emission, which is

why the frequency domain comb structure smooths out into a continuous spectrum. The result is an isolated attosecond pulse in the time domain, as illustrated in Figure 2.5 C.

Isolated attosecond pulses provide the highest temporal resolution due to their short duration, whereas attosecond pulse trains last longer but offer higher photon flux. However, neither pulse trains nor isolated pulses are typically transform-limited, as the intrinsic attochirp causes temporal broadening.

To achieve the shortest pulse duration, attochirp compensation is necessary. Common approaches implement thin metallic filters that introduce controlled amounts of anomalous dispersion [16, 21, 56]. Furthermore, dispersive media such as argon gas [57, 58] and chirped XUV mirrors [59, 60] have shown to effectively compensate for the attochirp. Beyond that, plasma has been discussed [61, 62].

2.5 Generation target

HHG can be achieved in various media, including gases [63], liquids [64], and solids [65, 66]. However, gases remain the most commonly used media because of their advantageous practical properties in a vacuum environment. The choice of gas is especially crucial, as it determines both the cutoff energy and the conversion efficiency.

The ionization potential of the gas directly dictates the maximum photon energy, as described by the cutoff law in Equation (2.5). Moreover, a higher ionization energy allows the gas to withstand stronger driving fields, before excessive ionization makes the process less efficient. Applying a stronger driving field increases the ponderomotive potential, which, in turn, raises the maximum photon energy at the harmonic cutoff. However, when ionization does occur, the resulting plasma introduces a negative phase matching term that degrades phase-matching conditions (see Section 2.6). Additionally, ionization depletes the neutral gas atoms, making them unavailable for high-order harmonic generation.

Noble gases are particularly favored in HHG experiments due to their closed-shell electronic configurations, which result in higher ionization potentials compared to other elements. Table 2.1 lists the ionization energies and static dipole polarizability of selected noble gases. The ionization energy decreases with increasing atomic number Z, leading to a lower cutoff energy for noble gases with larger Z.

Table 2.1: Noble gases and their ionization energies. The ionization potential decreases with the atomic number Z, while the static dipole polarizability increases.

Element	Atomic number Z	Ionization Energy I_p (eV) [67]	Static dipole polarizability α_∞ (a.u.) [68]
Helium (He)	2	24.59	1.407
Neon (Ne)	10	21.56	2.571
Argon (Ar)	18	15.76	11.23
Krypton (Kr)	36	13.99	16.86
Xenon (Xe)	54	12.13	27.03

However, noble gases with higher Z also exhibit greater polarizability, which enhances their interaction with the driving field and effectively increases the XUV yield. While the static polarizability in Table 2.1 provides a qualitative measure of how strongly an atom interacts with the laser field, it does not serve as a direct quantitative indicator, since the driving laser is a dynamic, oscillating field.

Therefore, selecting an optimal generation gas requires balancing the trade-off between maximizing harmonic yield and achieving the desired spectral range.

2.6 Phase matching

Up to this point, we have discussed only the single-atom response in high-order harmonic generation. However, HHG is a macroscopic phenomenon that arises from the collective contributions of many atoms. For efficient HHG, the emitted electromagnetic waves from individual atoms must interfere constructively as they propagate through the medium, enabling their contributions to add up coherently. Figure 2.6 A illustrates this principle by contrasting schematics of ideal and imperfect phase matching.

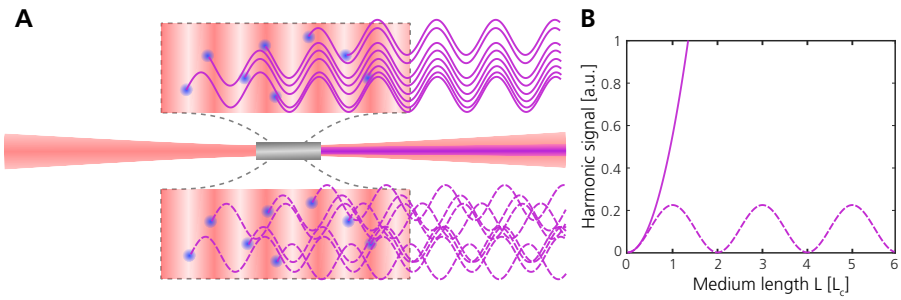

Figure 2.6: Concept of phase matching along propagation. (A) The HHG originating from different points along propagation add up constructively (upper panel) or destructively (lower panel). **(B)** Schematic diagram of the harmonic yield along propagation for ideal phase-matching condition (solid line) and the non-ideal case (dashed). Courtesy of Robin Weissenbilder [41].

Following [69], the harmonic intensity can be expressed as a function of the propagation length

$$I_q \propto \rho^2 \left|d_q\right|^2 L^2 \operatorname{sinc}^2\left(\frac{\Delta k L}{2\pi}\right) , \tag{2.17}$$

assuming a medium with constant gas density ρ and the dipole amplitude d_q from SFA (see Section 2.2) and the general wave vector mismatch Δk. Figure 2.6 B illustrates the harmonic signal as a function of propagation through the medium. The coherence length, $L_\mathrm{c} = \pi/\Delta k$ defines the propagation distance over which constructive interference occurs. If the propagation distance through the medium is longer than the coherence length, the intensity will oscillate, as the wave vector mismatch equals a phase offset, causing the contributions to align and misalign periodically along propagation [70].

The wave vector mismatch

$$\Delta k = q k_1 - k_q, \tag{2.18}$$

is the wave vector difference between the fundamental k_1 and the harmonic k_q, with the harmonic order q. There are four individual factors the wave vector mismatch is composed of [36, 71, 72]:

$$\Delta k = \underbrace{\Delta k_\mathrm{at}}_{\text{Neutral gas dispersion}} + \underbrace{\Delta k_\mathrm{fe}}_{\text{Plasma dispersion}} + \underbrace{\Delta k_\mathrm{foc}}_{\text{Gouy phase}} + \underbrace{\Delta k_\mathrm{i}}_{\text{Dipole phase}} \tag{2.19}$$

Each term represents a specific physical effect that can induce phase mismatch.

Δk_at **Neutral gas dispersion:** This mismatch arises from the different phase velocities of the fundamental and harmonic fields in the dispersive neutral gas medium:

$$\Delta k = \left(n_\mathrm{Fun} - n_q\right) \frac{q\omega_0}{c}, \tag{2.20}$$

where n_Fun is the refractive index at the fundamental frequency, and n_q the refractive index at the frequency of the harmonic.

Δk_fe **Plasma dispersion:** This component of the phase mismatch results from the dispersion due to free electrons. The ionization rate depends highly on the intensity of the driving laser. Controlling this dispersion is crucial to achieving good phase-matching conditions.

Δk_foc **Gouy phase:** This contribution to the phase mismatch arises from the geometric phase shift that occurs when a beam passes through a focus. For Gaussian beams, this phase shift is commonly referred to as the *Gouy phase* [73].

Δk_i **Dipole phase:** The dipole phase shift is associated with the single-atom dipole phase, as introduced in the previous sections (Section 2.2 and 2.3). The dipole phase varies with the electron trajectory in the continuum, is strongly intensity-dependent, and can significantly affect phase matching.

For perfect phase matching, the total wave vector mismatch should be zero. When this condition is met, constructive interference is maximized, leading to the highest possible conversion efficiency in HHG. However, it is usually not possible to achieve perfect phase matching for all harmonic orders at the same time.

2.7 Intense high-order harmonic generation

A high XUV flux is crucial for many experiments and can be achieved in two ways: by increasing the repetition rate of the driving laser or by maximizing the XUV yield within a single laser pulse. While higher repetition rates are beneficial for applications that rely on high experimental statistics, certain experiments demand high XUV intensities to trigger nonlinear effects [74–77], which can be effectively achieved by increasing the XUV yield per pulse.

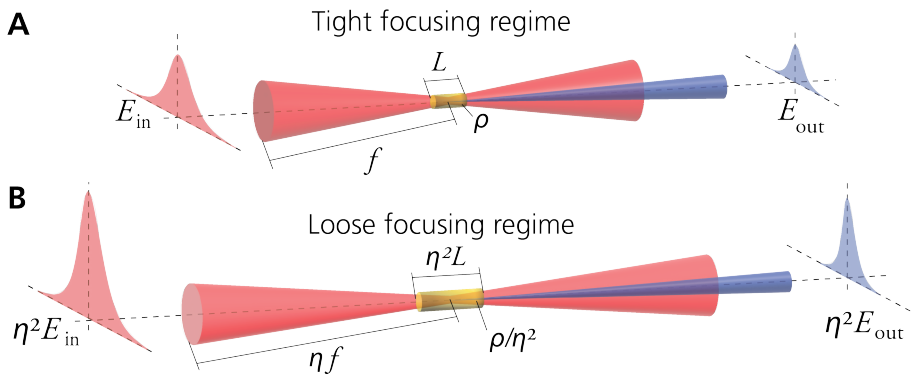

Figure 2.7: Scaling principle for high-order harmonic generation. (A) HHG in a tight focusing regime. **(B)** In a loose focusing regime, the focal length is extended, while maintaining the initial beam diameter. When adjusting the input energy, medium length, and pressure, the XUV output will scale accordingly.

To achieve an increase in XUV yield, efficient phase matching and conversion efficiency must be maintained while increasing the driving laser energy. However, even under optimized phase matching, the conversion from the incoming IR pulse to the generated XUV energy (E_{out}/E_{in}) is inherently low. For example, reported conversion efficiencies for a single harmonic order in neon are around $\sim 5 \times 10^{-7}$[78],

in argon low $\sim 10^{-5}$ [79], and for the 15th harmonic order generated in xenon it is around $\sim 5 \times 10^{-5}$ [70, 79, 80].

Scaling the experiment requires transitioning from tight to loose focusing. In a tight-focusing regime, the beam intensity follows a Gaussian distribution along the propagation axis (Figure 2.7 A). The beam is characterized by its input energy E_{in}, the focal length f, the waist in focus w_0 and its Rayleigh range $z_{\text{R}} = \frac{\pi w_0^2}{\lambda}$. The Rayleigh range represents the section along the propagation axis where the beam's cross-sectional area doubles, and its peak intensity decreases to half of its value at the waist.

The loose focusing regime (depicted in Figure 2.7 B) describes the case where the focal length is increased by a η factor $f \rightarrow \eta f$ while keeping the input beam diameter unchanged. This results in a quadratic increase in the Rayleigh range and a quadratic expansion of the volume within which the beam intensity remains roughly constant. The scaling law predicts that the conversion efficiency is maintained when appropriate adaptations to the system are made, following [81–83]:

- Increasing input energy $E_{\text{in}} \rightarrow \eta^2 E_{\text{in}}$,
- Extending the medium length $L \rightarrow \eta^2 L$, and
- Reducing the gas density $\rho \rightarrow \rho/\eta^2$.

Consequently, if the conversion efficiency is maintained, the XUV output energy will scale linearly with the input energy: $E_{\text{out}} \rightarrow \eta^2 E_{\text{out}}$.

For this reason, high XUV intensities require beamlines that are large-scale systems, characterized by long focal lengths and extended gas generation volumes. For instance, the Intensity XUV Beamline in Lund has a focal length of approximately 8.7 meters, providing an XUV energy of $E_{\text{out}} \approx 40\,\text{nJ}$ [84]. In comparison, the SYLOS LONG GHHG beamline (see Section 3.3) offers two focal geometries: a shorter configuration with a 19-meter focal length and a longer one extending to 55 meters. This design aims to achieve an XUV energy of $E_{\text{out}} > 300\,\text{nJ}$, with experimental validation pending [85].

Chapter 3

Experimental Methodology

This chapter describes the experiments and the methods they are based on, forming the foundation for the publications included in this thesis. A significant development during the course of this work was the decommissioning of the old laser and the installation of a new system at the Lund High-Power Laser Facility. The Lund CPA Terawatt Laser system, established in 1991, employed chirped pulse amplification. This system remained in operation until May 2023, covering roughly two-thirds of the time during which this thesis was conducted. Subsequently, most of the results were produced based on the CPA laser system. It has since been replaced by a new Optical Parametric Chirped-Pulse Amplification (OPCPA) laser system by *Light Conversion*, which became operational in November 2023. To provide context, this chapter includes a section on the fundamentals of laser amplification, serving as the foundation for the subsequent discussion of the differences between the old and the new laser systems.

Building on this foundation, a detailed description follows of the main experimental setup, the Intense XUV Beamline in Lund. This beamline was central to all experiments, and the data acquired from it contributed to all publications: **Paper I – V.** The setup is described sequentially, following the path of the beam through the experiment. The Intense XUV Beamline also served as a conceptual basis for the SYLOS GHHG LONG Beamline, an upscaled version located at the ELI-ALPS facilities in Szeged, Hungary. Two experimental campaigns were conducted there, of which one contributed to **Paper IV**. Consequently, this chapter concludes with a brief overview of the SYLOS GHHG LONG beamline.

3.1 Femtosecond laser amplification

High-intensity laser pulses are essential for HHG because they provide the strong field enabling the tunneling ionization regime, which requires intensities in the range of $10^{13} - 10^{15}\mathrm{W/cm^2}$ [36]. The duration of the laser pulse determines the temporal resolution of the experiment and should therefore be as short as possible.

Direct amplification of such pulses to multi-terawatt peak powers is generally not feasible, as the high electric field of an intense beam would cause breakdown or damage to the amplification material. To prevent excessive intensities in the amplification medium, Chirped Pulse Amplification (CPA) can be employed. This method, established in 1988, has been significant to the historical development of high-intense lasers, and was awarded the Nobel Prize in Physics in 2018 [11, 86].

In CPA, the pulse is stretched in time, reducing the peak intensity to stay below the critical damage threshold. The stretched pulse is then amplified in, for example, a Ti:sapphire gain medium. Figures 3.1 A and C depict the principles of laser amplification. A significant challenge arises from heat dissipation in the gain medium, caused by the inevitable energy mismatch between the energies of the pump and signal laser. This heat load requires efficient cooling mechanisms to prevent thermal lensing effects [87, 88]. Both the high heat load and the damage threshold of the gain medium limit the output power scalability of Ti:sapphire-based CPA systems. This limitation

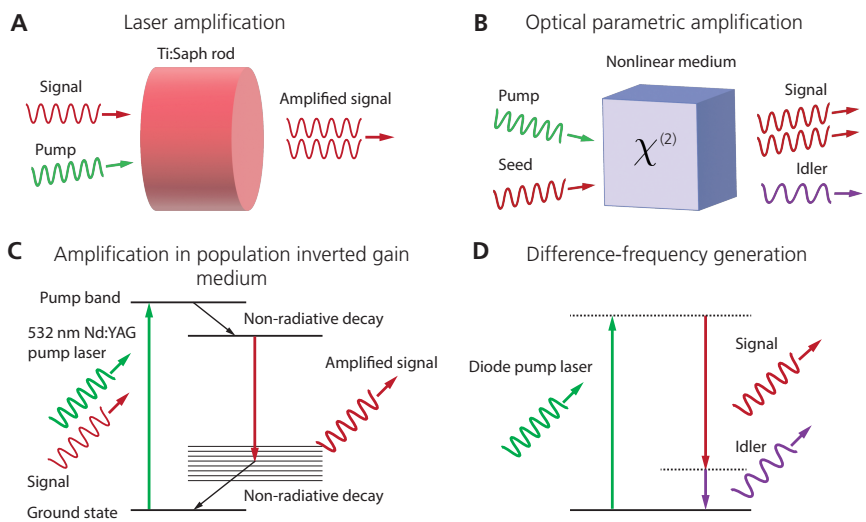

Figure 3.1: Principles of laser amplification and optical parametric amplification schemes. **(A)** Schematic of laser amplification using Ti:sapphire crystals as the gain medium, pumped by an Nd:YAG laser. **(B)** Schematic of optical parametric amplification using a nonlinear medium. **(C)** Energy level diagram showing the relative energies of the pump and the output laser for the Ti:sapphire laser. **(D)** Energy level diagram illustrating the nonlinear conversion of the pump laser into signal and idler beams.

is mitigated using the technique of Optical Parametric Amplification (OPA), where the pump laser and the seed pulse are combined in a nonlinear crystal. Through the nonlinear properties of the crystal three-wave mixing occurs, wherein the energy from the pump is transferred to amplify the seed (signal), while an idler beam is generated corresponding to the frequency difference between signal and pump. Figures 3.1 B and D show the principle of optical parametric amplification. Crucially, this process avoids high thermal loads within the nonlinear medium, as the excessive pump energy does not remain within the crystal.

A further distinction is made between collinear and Noncollinear Optical Parametric Amplification (NOPA). The (non-) collinear refers to the alignment of the pump laser with respect to the signal, resulting in different phase matching geometries. NOPA support a broader bandwidth, as the specifically chosen noncollinear angle reduces the temporal walk-off between the pump and signal that arises from the dispersion-based group velocity mismatch [89]. As the broader bandwidth supports shorter pulses, NOPA is the preferred method for femtosecond amplification. Both methods are highly efficient, reaching conversion efficiencies of up to 50% [90, 91].

OPCPA lasers combine the advantages of low peak intensity through CPA with the low thermal loading and high conversion efficiency from OPA, and were first introduced in 1991 [13].

3.1.1 The CPA terawatt laser system

The CPA terawatt laser system was the first system acquired for the *Lund High-Power Laser Facility* and later called the *Lund Terawatt laser*. The laser was put into operation in 1991 and has contributed to early publications on HHG [6, 92]. It has been continuously upgraded over the years, with significant improvements to its specifications. About 40 PhD and licentiate students graduated using this system, and it contributed to the creation of approximately 90 scientific publications. Until it was decommissioned in May 2023, an estimated 2.2 billion laser shots were amplified with the Ti:sapphire crystals [93].

Figure 3.2 provides an overview of the different stages of the terawatt laser system in its final shape. The front-end consisted of a Ti:sapphire oscillator generating low-energy pulses with a duration of 30 fs and a repetition rate of 80 MHz. A pulse picker reduced the repetition rate to 10 Hz before preamplifying and stretching the pulses to a duration of about $200-300$ ps. Temporal stretching was achieved using two parallel diffraction gratings that dispersed the frequency components. The different frequency components of the pulse travel different path lengths, effectively delaying them from one another, which stretches the pulse in time. The stretched pulses then underwent

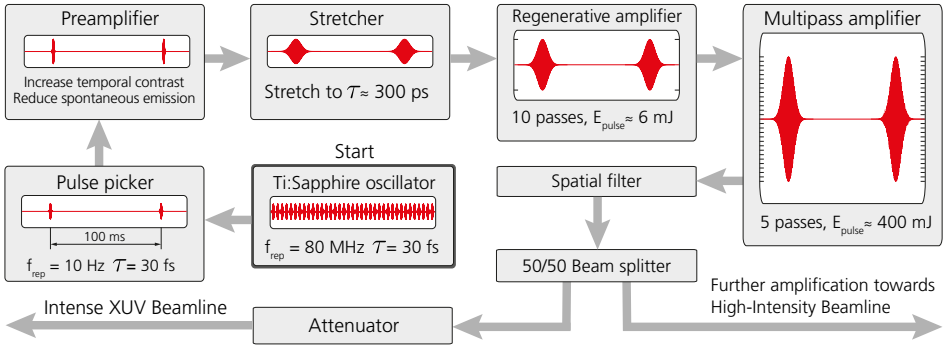

Figure 3.2: Schematic of the CPA laser system in Lund, decommissioned in May 2023. The system featured a Ti:sapphire oscillator and multiple amplification stages, including a regenerative amplifier and a multipass amplifier. The laser was driving experiments in two laboratories, the High-Intensity Beamline and the Intense XUV Beamline.

multiple amplification steps inside the regenerative and multipass amplifiers. Spatial filtering was applied by focusing the beam in vacuum, and cutting off the higher spatial frequency components at the focus using custom-sized glass capillaries.

Afterwards, the beam was split, with half of the power undergoing further amplification and being guided toward the High-Intensity Beamline, where experiments on laser wakefield acceleration are performed [94]. The other half went through a Brewster's angle attenuator, allowing for tuning the pulse energy. After compression in the Intense XUV Beamline, this system achieved a pulse duration of $\tau = 35\,\mathrm{fs}$ with a compressed pulse energy of $50\,\mathrm{mJ}$ at a repetition rate of $f_{\mathrm{rep}} = 10\,\mathrm{Hz}$.

3.1.2 The OPCPA laser system

The OPCPA laser system was installed at the facility after the CPA laser system was decommissioned. The OPCPA became fully operational in November 2023, after a six-month shutdown period. The laser front-end consists of a Light Conversion ORPHEUS-OPCPA, pumped by a PHAROS laser, an ytterbium-doped solid-state chirped pulse amplifier operating at 1030 nm. This seed is then guided into the 100 Hz amplifier. Figure 3.3 presents a flow chart of the laser system.

The seed coming from the laser front-end first goes through a GRISM pulse stretcher, a combination of a grating and a prism (thus GR-ISM). This dispersive element induces a frequency-dependent delay, stretching the pulse over time with a negative dispersion. The chirped pulse passes the Dazzler, an Acousto-Optic Programmable Dispersive Filter (AOPDF) [95]. The Dazzler allows for precise control over the spectral phase and amplitude of the pulse by adjusting a sound wave within a birefringent

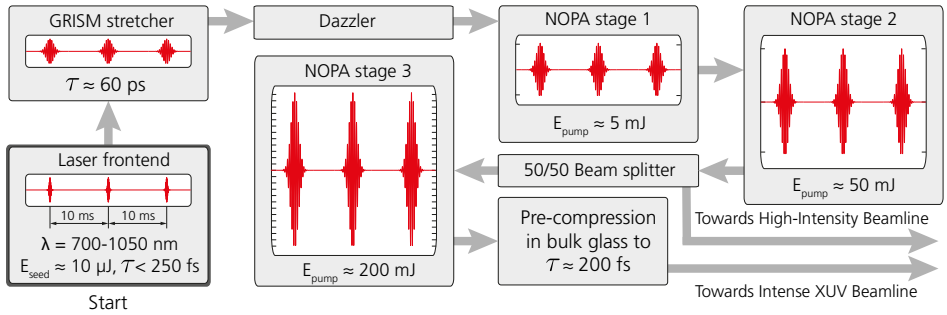

Figure 3.3: Flow chart of the 100 Hz OPCPA laser system. The beam coming from the front end is stretched by the GRISM stretcher and manipulated using the Dazzler. After two amplification stages, the beam is split, with one part directed toward the High-Intensity Beamline. The other part undergoes a third amplification stage before being guided toward the Intense XUV Beamline.

crystal, thereby tuning the dispersion. This fine-tuning is crucial to achieving minimal pulse duration and optimizing phase matching for HHG.

Amplification is achieved in three NOPA stages with increasing pumping power of 5 mJ, 50 mJ, and 200 mJ, respectively. Half of the beam power is taken out between the second and third amplification stage. This part undergoes further amplification in a separate unit, and is guided toward the High-Intensity beamline. In this way, the first two amplification stages are shared between the two experiments, while the third stage is used exclusively by Intense XUV Beamline. The pump energy at each stage is adjustable from 0 to 100 %. All optical pumps originate from the same frequency-doubled Nd:YAG laser, operating at 532 nm with a pulse duration of 90 ps.

After amplification, a set of bulk glass blocks pre-compresses the pulse from 60 ps to approximately $200 - 300$ fs, which is about three orders of magnitude shorter relative to the uncompressed pulses of the previous CPA system. A telescope slightly demagnifies the beam in order to reduce its diameter, before it exits toward the Intense XUV Beamline. To achieve a final pulse duration of sub-10 fs, the pulses undergo compression using a chirped-mirror compressor located in the beamline setup (refer to Subsection 3.2.1 for details).

The backreflection from the laser output window is compressed by a separate chirped-mirror compressor inside the laser enclosure. The compressed beam is used for pointing stabilization, and pulse duration monitoring (see Subsection 3.1.4 for laser pulse diagnostics).

3.1.3 Comparing both laser systems

The upgrade to a state-of-the-art laser system brings several improvements to the system specifications. Table 3.1 summarizes some key differences between the former laser system and its successor. While the pulse energy remained unchanged, the significantly reduced pulse duration leads to a corresponding increase in peak pulse intensity. These changes necessitate a larger beam diameter to ensure the beam remains below the damage threshold of mirror materials. Additionally, with the repetition rate being ten times higher, the output power scales proportionally. A shorter, sub-10 fs pulse duration inevitably results in a broader bandwidth, as dictated by the time-bandwidth product (see Equation (2.16)). Figure 3.4 compares the spectrum of the OPCPA laser system with that of the CPA laser.

Table 3.1: Comparison of CPA and OPCPA laser system parameters.

Parameter	CPA System	OPCPA System
Central wavelength	800 nm	839 nm
Pulse energy	50 mJ	50 mJ
Pulse duration	35 fs	9 fs
CEP stable	No	222 mrad over 8 hours
Intensity profile	Gaussian	Flat-top
Repetition rate	10 Hz	100 Hz
Beam diameter ($1/e^2$)	38 mm	47 mm

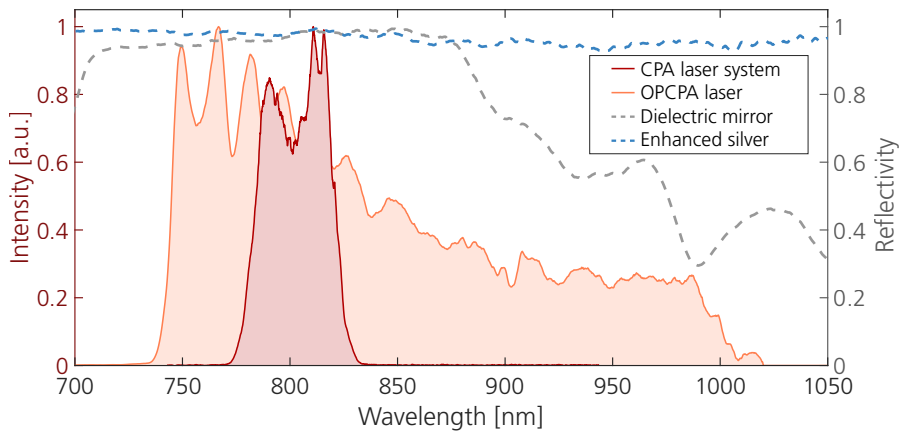

Figure 3.4: Comparison of spectra (solid) and mirror reflectivity (dashed): Spectrum of the decommissioned CPA laser (red) compared to the OPCPA laser system (orange). The dielectric mirror (grey) shows a narrower region of high reflectivity than the enhanced silver mirror (blue). The reflectivity measurement was performed using an incoherent black body radiation source and thus only gives a qualitative impression.

The increased spectral width imposes additional requirements on the optical components of the beamline. While the CPA system could rely on dielectric mirrors with relatively narrow bandwidths, the broader spectrum of the new laser necessitates the use of broadband dielectric mirrors or enhanced silver mirrors, which provide consistently high reflection over a broad range, while inducing minimal Group Delay Dispersion (GDD). The dashed lines in Figure 3.4 illustrate the spectral reflectivity of both types of mirrors. Notably, the dielectric mirror coating does not fully cover the new laser system's range, which explains the need to replace all IR optics during the upgrade.

3.1.4 Femtosecond laser pulse diagnostics

The broader spectrum in ultrafast laser systems introduces challenges in dispersion management, as dispersion becomes more pronounced with shorter pulse durations as a result of the broader bandwidth. Particularly in HHG, dispersion management is critical, as the temporal pulse profile affects the intensity, and subsequently the harmonic yield, cut-off and duration of the APT. Advanced diagnostic tools are therefore essential for characterizing and optimizing the performance of few-cycle femtosecond lasers.

Traditional autocorrelators, widely used for measuring the duration of ultrafast pulses [96] offer limited insight since the autocorrelator trace lacks information on the spectral phase. The spectral phase, however, can be decomposed into a Taylor series, obtaining values for the group delay dispersion as well as higher order terms. This in turn allows for a precise dispersion compensation with pulse shaping devices, such as the Dazzler. Hence, the ability to monitor the spectral phase allows for precise optimization toward the shortest pulse duration.

Different methods exist to obtain the spectral phase of ultrashort pulses, such as Frequency-Resolved Optical Gating (FROG) [97, 98], Spectral Phase Interferometry for Direct Electric Field Reconstruction (SPIDER) [99], and the dispersion scan (d-scan) [100, 101]. All three methods retrieve the spectral phase enabling determination of the pulse characteristics. However, since most ultrafast laser systems already have adjustable pulse compressors, setting up the d-scan is trivial.

Given the simplicity of the setup and the on-site expertise in developing the d-scan [102, 103], it has become our diagnostic tool of choice.

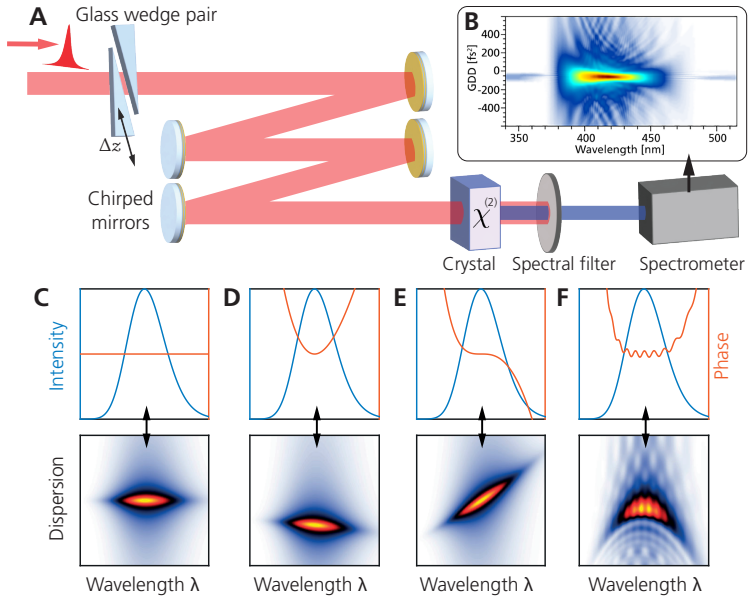

Figure 3.5: Working principle and results of a scanning d-scan: (A) Schematic of the setup. The second-harmonic generation signal from the crystal (marked by χ_2) is measured as a function of the insertion depth of a glass wedge pair, which introduces a controlled amount of group delay dispersion. **(B)** d-scan trace of the OPCPA laser system. **(C-F)** Spectral intensity and phase (upper row) and simulated d-scan trace (lower row). Subfigure (C) features an optimized pulse, while (D-E) have second, and third order dispersion respectively added to the spectral phase. Figure (F) showcases fourth-order dispersion with additional phase-ringing, as it is typical for a beam compressed by chirped mirrors. Figures (C-F) adapted from Ivan Sytcevich [104].

In this approach, a pair of BK7 glass wedges is introduced and by varying the insertion depth of the wedges, a controlled amount of dispersion is added. A set of chirped mirrors compensate for the dispersion introduced by the wedges. After frequency doubling in a Second Harmonic Generation (SHG) crystal, the SHG spectral intensity is recorded as a function of the added dispersion. Figure 3.5 A illustrates the working principle of a scanning d-scan, with the retrieved SHG intensity map depicted in panel B.

Since frequency doubling is a nonlinear process, it is inherently sensitive to the peak intensity of the pulse which encodes the spectral phase (and thus to the pulse duration), yielding the strongest (and broadest) SHG signal at the point of optimal compression. The resulting 2D map of second harmonic spectrum as a function of dispersion is the d-scan trace, from which the temporal pulse profile can be extracted via retrieval algorithms [100, 105–107].

Figure 3.5 C-F contains the d-scan traces (lower panel), as well as the corresponding spectral intensity and phase for a Gaussian-shaped pulse (upper panel). Panel C corresponds to an optimized pulse with a flat phase. Panel D and E have a GDD

and Third-Order Dispersion (TOD) added respectively. Subfigure F shows a d-scan with some fourth-order dispersion, and additional ringing as it is typical for chirped mirror pulse compressors. For a more thorough discussion of pulse characterization using dispersion scans, the reader is referred to [103].

3.2 The Intense XUV Beamline

The Intense XUV Beamline is one of four attosecond light sources at the Atomic Physics Division in Lund. The experiment was established in 2012, with the first results published in 2013 [108, 109]. Figure 3.6 is a beamline schematic, which illustrates the key parts of the beamline in a simplified manner.

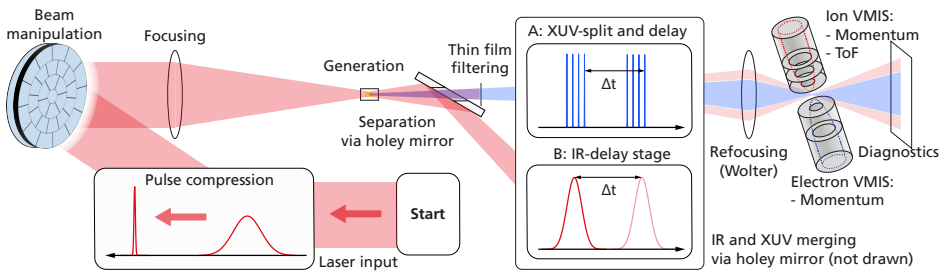

Figure 3.6: Flow illustration of the Intense XUV Beamline: The beam is compressed, manipulated, and focused into a generation gas to create harmonics. In the next step, the IR and XUV components are separated via a holey mirror. Thin film filtering removes remaining IR from the XUV beam path. The XUV split-and-delay unit and the IR delay stage enable two separate types of experiments. Refocusing the beam into a target gas produces both photoelectrons and ions, which are analyzed by the DVMIS. Diagnostic elements for the beam are installed at the end of the beamline.

The laser pulses are propagated through a 10 m long transport tube system connecting the laser room with the beamline. High-intensity pulses are prone to nonlinear effects (e.g., self-focusing) in air and are particularly sensitive to instabilities caused by air fluctuations. Furthermore, XUV radiation cannot propagate through material, including air, because it is absorbed. Consequently, the transport tube system and all subsequent beamline parts are maintained under vacuum.

Given its complexity and scale, the experiment is divided into two sub-sections: the generation part and the application part. The generation part covers all parts until the generation target, including compression, beam manipulation, and focusing. The application part encompasses the separation of XUV from the IR, the interferometric delay units, refocusing toward the target interaction, acquisition instruments, and beam diagnostics.

3.2.1 Intense XUV Beamline: Generation part

The elements of the generation part are pulse compression, beam manipulation, and focusing into the generation gas, which can vary in length, density, and shape. Additionally, the system is equipped with a rotational stage that introduces a pick-up mirror to redirect the beam toward an auxiliary output for offline diagnostics, enabling a full-power beam characterization when required. Figure 3.7 illustrates the generation part for the old and new laser systems in comparison.

Pulse compression

The upgrade of the laser system required a change of the pulse compression technique. While the CPA laser system employed diffraction gratings for pulse compression, as illustrated in Figure 3.7 A, the OPCPA system relies on a chirped-mirror compressor, shown in Figure 3.7 B.

The principle behind pulse compression with a grating compressor is that two grating surfaces are arranged in parallel, diffracting the beam in a way that causes different spectral components to traverse varying path lengths. When different spectral components enter the compressor temporally separated, they exit simultaneously, resulting in a shorter pulse duration [110, 111]. The amount of dispersion is determined by the grating constant, the distance between the gratings and the incidence angle. The gratings' incidence angles are arranged so that the -1 order beam is compressed, while the $+1$ and higher orders are evanescent, as their diffraction angles are equal to or beyond the grating plane. Without light diffracted in those orders, the compression efficiency increases [111]. However, the 0th-order reflection- unless suppressed, for instance, by a blazed grating- remains and can serve as a reference point for the beam alignment.

In the case of the CPA laser, the uncompressed pulse had a duration of $200 - 300\,\mathrm{ps}$ as it entered the beamline. After passing through two folding mirrors, the beam was directed into the grating compressor. The grating compressor consisted of two parallel diffraction gratings and a retro reflector. All components were mounted on rotational stages and the second grating was also placed on a linear stage to adjust the distance between the gratings, allowing the dispersion to be tuned. The retroreflector redirects the beam to a lower height. The reflected beam then followed the same path as the incoming beam, exiting the system at a lower height. This common arrangement, in which the same gratings are passed through twice, takes up less space, and simplifies the alignment. Under operating conditions, the compressed beam had $55\,\%$ of the input energy and a duration of $35\,\mathrm{fs}$.

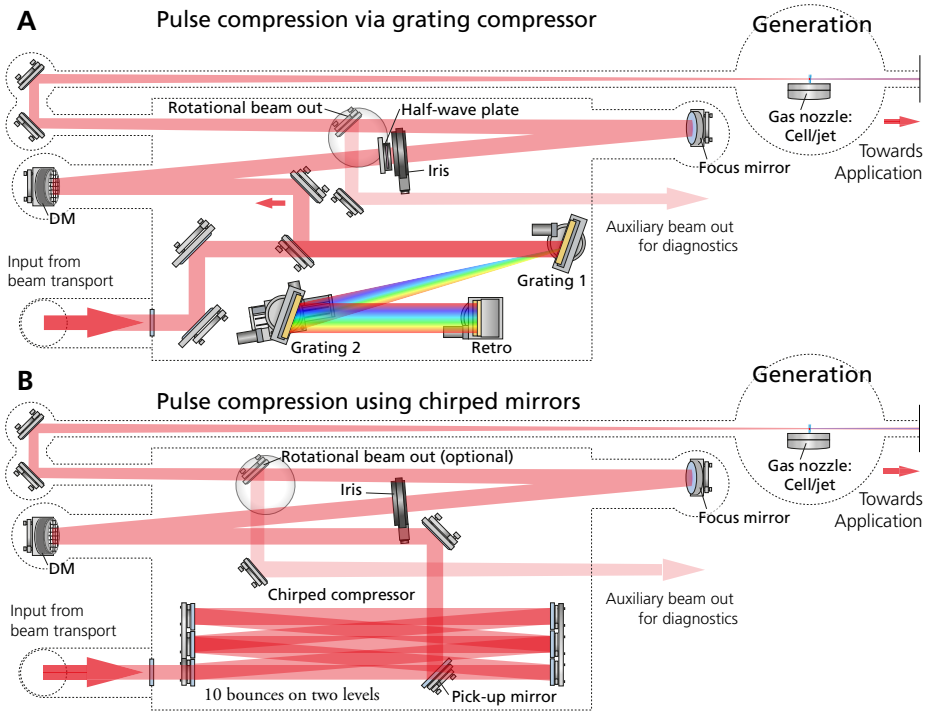

Figure 3.7: Generation part of the Intense XUV Beamline. (A) Setup with grating compressor: The beam entering from the beam transport tube system is guided into the grating compressor. **(B)** Generation part with chirped-mirror compressor. The chirped mirrors compress the laser pulse over 10 bounces across two vertically separated layers of mirrors before the beam is directed toward the deformable mirror. Identical in both parts: after passing through an iris, a curved mirror with a focal length of 9 m focuses the beam into the generation gas.

Figure 3.7 B illustrates the beamline's generation part after the laser upgrade. Notably, the grating compressor was replaced by a chirped-mirror compressor, while the remaining components, such as the deformable mirror, iris, and focusing mirror, remained in their original positions.

The operational principle of chirped mirrors relies on alternating layers of materials with differing refractive indices, where the layer thickness gradually changes. This variation in thickness causes different spectral components to penetrate the material to different depths, resulting in Group Delay Dispersion (GDD). Consequently, a limited amount of dispersion can be added per reflection. Multiple reflections are needed to compress the beam to its final pulse duration. The transmission of a chirped-mirror compressor with a reflectivity $R > 99\%$ per reflection is generally higher than that of a grating compressor.

Figure 3.8 shows the chirped-mirror compressor in an isolated view. The compressor unit consists of 10 chirped mirrors arranged in two horizontal layers of five mir-

rors each, with the edges spaced just one centimeter apart. This minimal spacing, combined with the large distance of approximately 130 cm between the two mirror holders, minimizes the angle of incidence, which is crucial for operating within the coating specifications. To mitigate spectral ringing in the reflected beam caused by the coating structure, chirped mirrors are paired with complementary coatings that cancel each other's phase distortion.

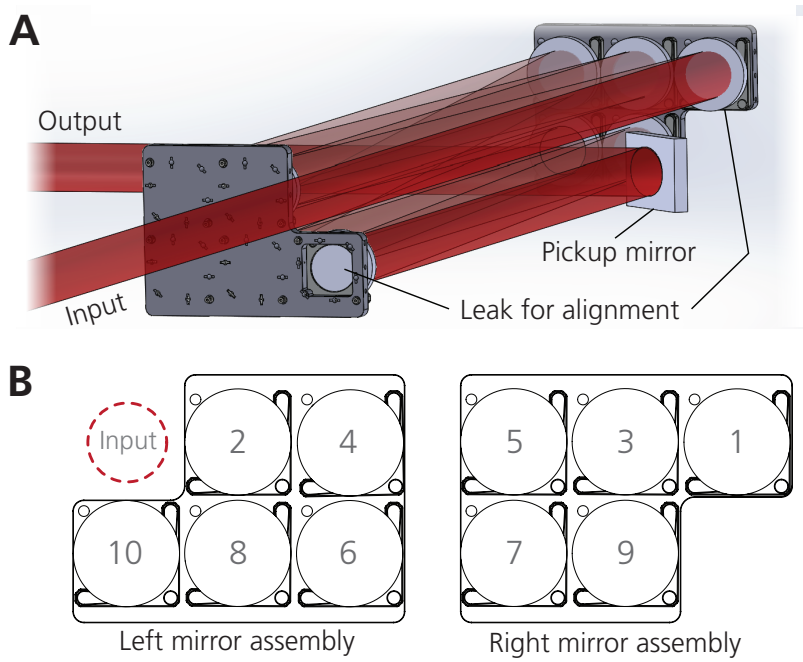

Figure 3.8: Principle of the chirped mirrors compressor: (A) Render of the mirror assembly with rays. The holder has a hole behind the first and last mirrors to utilize the beam leak as an alignment point. **(B)** Face view of the two assembly sides, with the order in which the beam bounces marked.

The chirped-mirror compressor at the Intense XUV Beamline reduces the pulse duration from 200 fs to sub-10 fs through 10 bounces on two layers of mirrors, with each mirror pair contributing a GDD of +100 fs^2. The beam enters the compressor at the top, undergoes five bounces, is deflected to the lower layer, and then completes five more bounces. The beam is picked up on the lower level using a rectangular mirror, which redirects toward the deformable mirror. The alignment of the incoming and outgoing beams is monitored using cameras that detect leakage through the first and last mirrors in the compressor. Piezoelectric actuators on the final mirror in the transport tube and the pick-up mirror enable precise alignment corrections under vacuum.

Beam manipulation

The Deformable Mirror (DM) at the Intense XUV Beamline facilitates wavefront correction of aberrated beams and allows for adjusting the focus position along the propagation direction. Figure 3.9 illustrates the operating principle of the DM. The mirror consists of a 2.5 mm thin substrate membrane with piezoelectric actuators on its back. Thirty-one actuators, arranged in concentric rings, shape the mirror's surface to correct the wavefront. One additional actuator adjusts the overall curvature of the reflected beam, effectively moving the focus position. The mirror has an open surface diameter of 80 mm, with an optically active area spanning 70 mm in diameter, the region that is covered by the piezoelectric actuators.

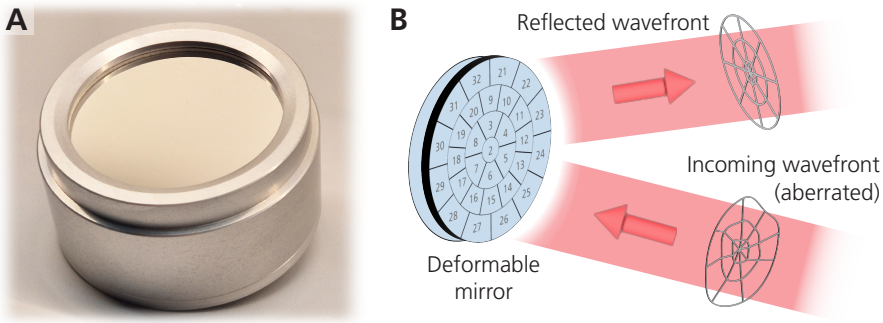

Figure 3.9: Photo and schematic of the deformable mirror. (A) Photo of the deformable mirror surface with an enhanced silver coating. **(B)** Functional principle: The incident wavefront shows visible distortions. The mirror's 31 actuators (indicated by their numbers in the figure) adjust the surface shape. After reflection, the beam is corrected, resulting in an aberration-corrected wavefront.

Wavefront distortions at the edges of the laser beam negatively impact the beam profile in focus, and subsequently the HHG phase matching. By trimming the outer regions of the beam with an iris, it becomes easier to achieve a well-defined, aberration-free focus. With the OPCPA system, the most efficient XUV generation is achieved when the beam is restricted to a diameter of 30 – 33 mm. Figure 3.10 illustrates the measured IR pulse energy as a function of the iris diameter.

The laser beam has a total diameter of 47 mm, and its intensity distribution follows a flat-top profile, indicating a relatively uniform cross-section. This is evident in the measured energy curve, which closely follows the surface area of a circle of the same diameter. From the graph, it can be observed that when the iris reduces the beam to diameters of 30 mm and 33 mm, the resulting pulse energy is approximately 41 % and 50 %, respectively, of the total energy of the full beam.

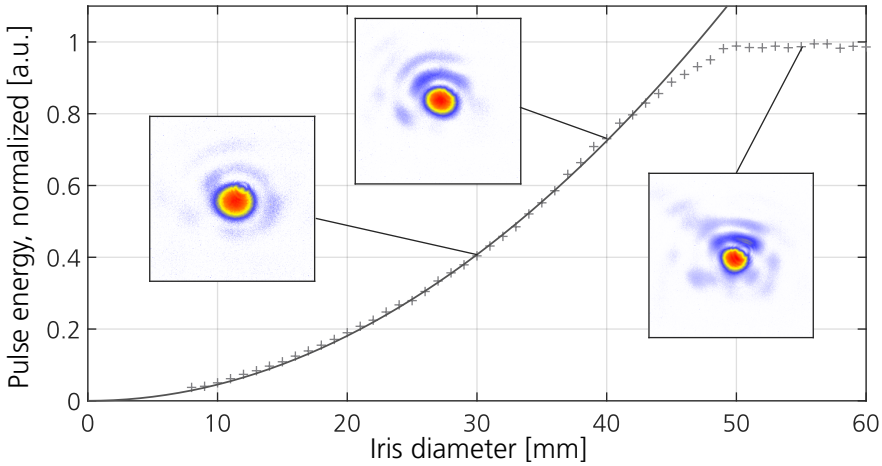

Figure 3.10: Pulse energy vs. iris diameter. The grey crosses represent the measured pulse energies, normalized to the maximum value. The black curve represents the surface area of a circle, normalized to a diameter of 47 mm. Focus images at selected positions are shown in the panels.

3.2.2 Beam focusing properties

After passing through the iris, the beam is reflected by a spherical focusing mirror with a focal length of 9 m, while the distance to the generation target is only 8.7 m. This means that the beam would naturally be focused slightly behind the target. As discussed in subsection 3.2.1, the DM can alter the wavefront curvature to compensate for this mismatch. In addition, the DM allows tuning the focus position away from the target, enabling what is referred to as *out-of-focus generation*.

In an ideal case, a perfectly rotationally symmetric Gaussian beam exhibits a single focal point with a well-defined beam waist and Rayleigh range. Given the central wavelength of 839 nm, a truncated beam diameter of 30 mm and a 8.7 m meter focal length, the beam waist at focus is in the transform-limited case of a Gaussian beam [73]

$$2w_0 \approx \frac{4\lambda f}{\pi D} = 309\,\mu\mathrm{m}, \tag{3.1}$$

with a corresponding Rayleigh length of $z_\mathrm{R} = 8.9\,\mathrm{cm}$. However, the beam width along propagation deviates from a pure Gaussian beam since the beam's intensity distribution is more aligned with a flat-top profile. Furthermore, an elliptical distortion in the beam focus is observed, which is caused by astigmatism. Astigmatism implies that the beam curvature differs in two orthogonal directions resulting in two points that are separated along the propagation axis—one in the sagittal plane and the other in the tangential plane.

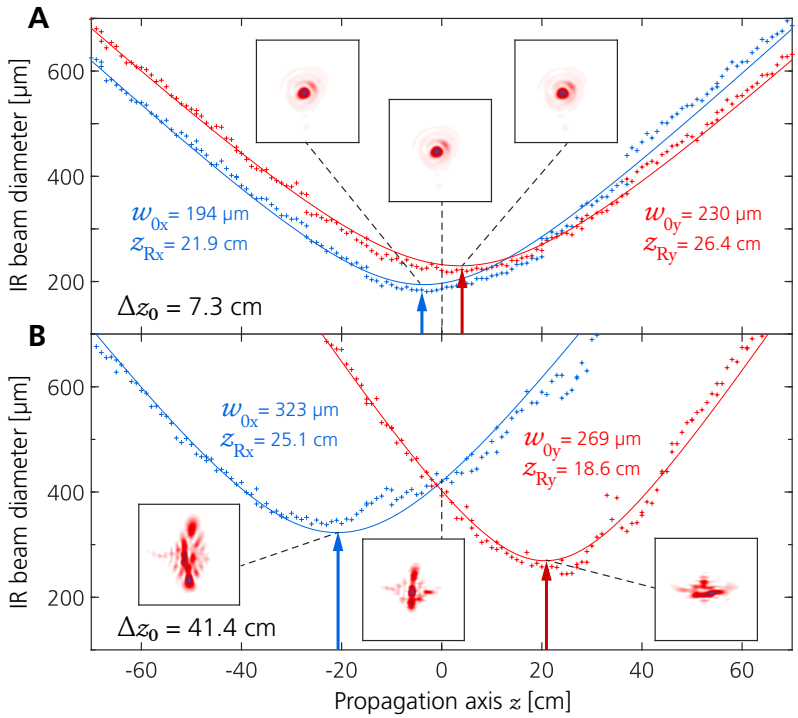

Figure 3.11: Beam waist along propagation and selected focus images with/without DM. (A) The DM-corrected beam shows slight astigmatism, indicated by the difference in focus position along the x- (blue) and y-axes (red), and the different waist w_0 in both directions. The images show the beam profile at selected positions. **(B)** Repeated measurement with a flat mirror replacing the DM. Both measurements are recorded using the OPCPA laser system. The beam is truncated by an 30 mm diameter iris.

Figure 3.11 A shows the measured beam diameters along the shortest and longest axes as a function of propagation distance. The deformable mirror was included and the beam was truncated by a 30 mm iris, resembling conditions for high-order harmonic generation. To determine the beam waist, the second-order moment was calculated, as the flat-top nature of the beam profile prevents the application of a Gaussian fit. The zero point on the propagation axis is defined as the average between both focus positions.

From these measurements, it is evident that the beam exhibits slight astigmatism, with the focal planes displaced by $\Delta z_0 = 7.3\,\mathrm{cm}$. The Rayleigh range for the earlier focal point is $z_{\mathrm{Rx}} = 21.9\,\mathrm{cm}$, while the later focus exhibits a longer Rayleigh range of $z_{\mathrm{Ry}} = 26.4\,\mathrm{cm}$. Furthermore, the beam waists at the two foci differ, with $\omega_{\mathrm{ox}} = 194\,\mu\mathrm{m}$ and $\omega_{\mathrm{oy}} = 230\,\mu\mathrm{m}$, respectively. The observed deviation from the calculated values can be attributed to the flat-top intensity profile in the near-field (i.e. before focusing). Upon focusing, a flat-top beam deviates from a Gaussian by maintaining a

uniform core while diffraction softens edges and introduces side lobes. This can also explain the larger Rayleigh range compared to the transform-limited case.

In comparison, Figure 3.11 B shows the same measurement, but with the DM replaced by a flat mirror. The profile exhibits clear distortions, with a pronounced focus position displacement.

Generation gas geometry

The generation gas density and density profile play an important role in the macroscopic properties of HHG (see phase matching, Section 2.6). While the impact of the generation gas type is discussed in Section 2.5, this subsection focuses on the physical geometry of the generation gas target.

At the Intense XUV beamline, gas is dispensed via a pulsed Attotech GR001 valve with adjustable opening time, width, and backing pressure [112]. The valve dispenses gas toward an adapter plate that supports the attachment of various geometries. The two primary configurations are a vertical slit and a gas cell.

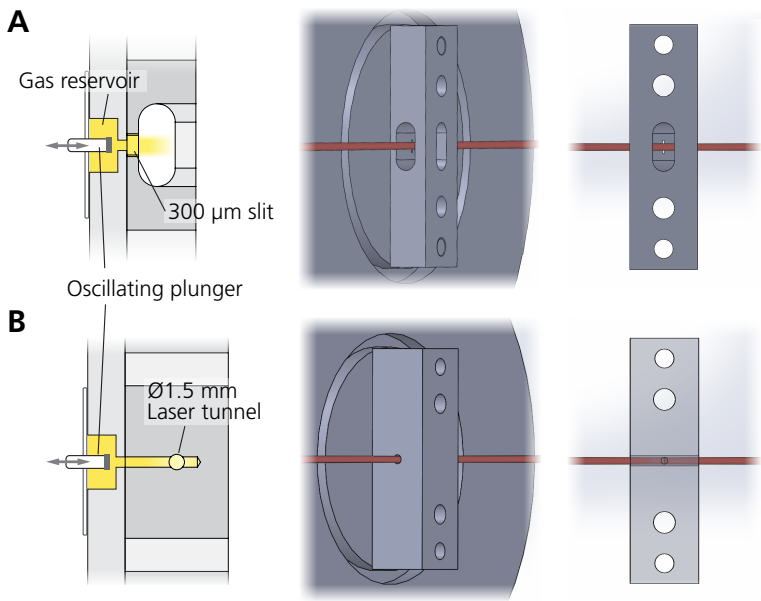

Figure 3.12: Comparison between different generation gas geometries. (A) Gas slit, resembling a very thin layer of generation gas with high density. **(B)** Gas cell with 1 cm length. The gas is injected into the tunnel, from where it expands in both directions along the laser propagation axis. In a similar geometry, pulsed gas cells with up to 11 cm tunnel length are used at the beamline.

In the slit geometry, gas is dispensed through a 300 μm wide and 4 mm high vertical slit, depicted in Figure 3.12 A. This offers a large cross-sectional area of a thin gas medium with relatively high density. The large cross-sectional area makes this target less sensitive to pointing instabilities, and the medium length is very thin, in contrast to the Rayleigh length of the driving laser. This geometry principally allows for generation with a larger beam away from the focal point.

In contrast, gas cells feature a 1.5 mm diameter channel of various discrete lengths between 5 and 110 mm. Figure 3.12 B shows a 10 mm long cell, where the gas is filled from the center of the channel and spreads out in both directions. The cell length can be significant in relation to the Rayleigh length of the laser. Although this configuration has proven to generate harmonics with higher conversion efficiency, it is sensitive to beam-pointing drifts.

3.2.3 Application part of the Intense XUV Beamline

The application part of the Intense XUV Beamline covers the section of the beamline from the point after generating XUV until the end of the beamline. Figure 3.13 is a schematic of this beamline section, with the left side connecting to the generation part.

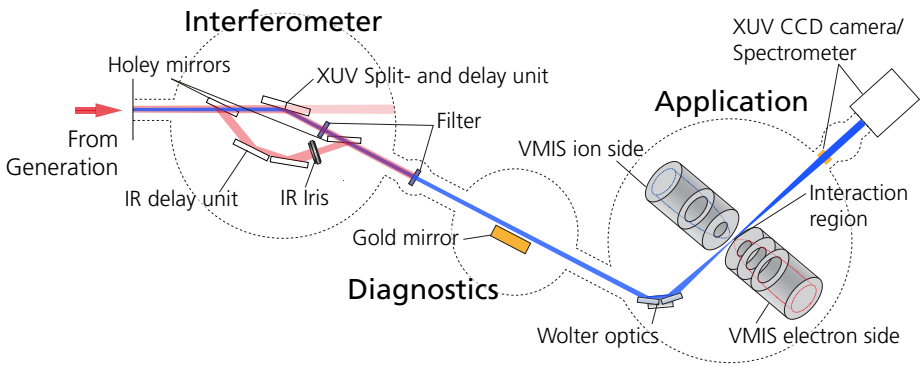

Figure 3.13: Application part of the Intense XUV Beamline: The XUV and IR beams propagate through the XUV–IR interferometer with the option to filter the IR with different kinds of filters. After passing through the Wolter optics, the beam is refocused inside the VMIS chamber, where the target gas is injected via an Even–Lavie valve (not shown in the illustration). The expanding beam is then diagnosed using the XUV spectrometer and XUV CCD camera.

In the interferometer chamber, the XUV and IR beams are separated and delayed with respect to each other, and the diagnostics chamber is equipped with photodiodes and a shutter controlling the beam propagation. The final stage of the beamline is the application chamber. At its entry, a toroidal mirror assembly in a Wolter configura-

tion [113] refocuses the beam into the center of the chamber, where the target gas is injected to define the interaction region. The resulting photoelectrons and ions can be resolved by the Double-Sided Velocity Map Imaging Spectrometer (DVMIS) in both the momentum and time of flight. At the end of the beamline, a diagnostics assembly allows for capturing the spatial profile using an XUV CCD camera (referred to as 'Andor' camera, after the manufacturer) or the measurement of the XUV spectrum. The specific components of the beamline are elaborated in detail in the following subsections.

XUV–IR interferometer

The XUV–IR interferometer is a compact system that separates and delays the XUV and IR beams with respect to each other in a Mach-Zehnder configuration, based on the work of [114]. To introduce a delay between the XUV and IR beams, the two collinearly propagating rays must first be separated. When the collinearly propagating beams enter the interferometer, the XUV component has a significantly smaller beam size compared to the IR beam. This difference arises from the fact that the beam divergence is determined by diffraction and proportional to the wavelength [115]. Because the XUV wavelength is several times shorter than that of the IR, the XUV beam exhibits a divergence that is several times smaller.

Since the XUV beam is smaller, it can be efficiently separated from the IR beam using a mirror with a drilled hole aligned with the XUV propagation axis, referred to as the *holey mirror*. In the setup shown in Figure 3.14, the XUV passes through the holey mirror, with the majority of the IR being reflected toward the IR translation stage. The XUV beam undergoes only a single reflection on a 10 ° grazing-incidence fused silica plate. A thin film filter (e.g. 200 nm aluminium) removes the remaining driving laser. The silica plate is part of the Split-and-Delay Unit (SDU), discussed in the next subsection.

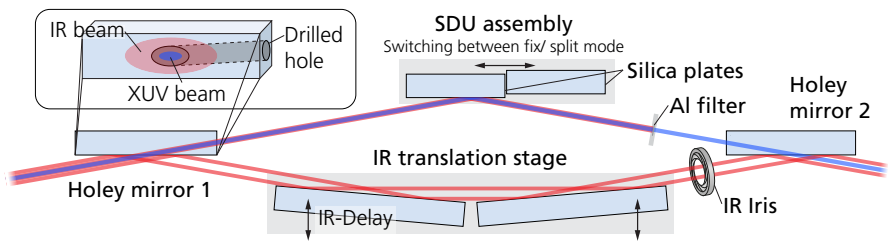

Figure 3.14: Schematic of the XUV–IR interferometer. The differing spatial footprint of the XUV and IR beams allows for their separation and recombination using grazing-incidence mirrors with drilled apertures. The IR beam is delayed via a translation stage. The XUV-beam is filtered and both beams are merged using a second holey mirror.

The IR beam undergoes two reflections within the translation stage, ensuring overlap at the interaction point even as the translation stage moves. The IR translation stage (Piezosystem Jena nanoX 400) operates in a closed-loop configuration, with a 400 μm scanning range and a resolution of 8 nm. Considering the trapezoid geometry of the assembly, this converts to a delay range of 560 fs and a step size of 11 as [114]. An iris in the IR path is used to control the amount of IR that reaches the interaction region.

Split- and delay unit

The Split-and-Delay Unit (SDU) is used to divide the XUV beam into two parts of equal energy and introduce a delay between them, allowing for XUV–XUV pump probe experiments [116].

The unit consists of two fused silica plates, one of which is fixed, while the other is equipped with actuators on three of the four corners. The actuators consist of a piezoelectric slipstick, which provide a wide range with a resolution of 14 nm per step, in combination with a piezo tip for fine, continuous adjustments. The assembly is located within the XUV–IR interferometer, as part of the XUV arm, as indicated in Figure 3.14. When the interferometer is in an XUV–IR configuration, the split- and delay unit is positioned at the fixed plate, ensuring that the XUV remains stable and unsplit. For an XUV–XUV configuration, the two mirrors are moved so that half of the XUV beam is reflected by each plate, and the IR-beam path is blocked or closed by the IR-path iris.

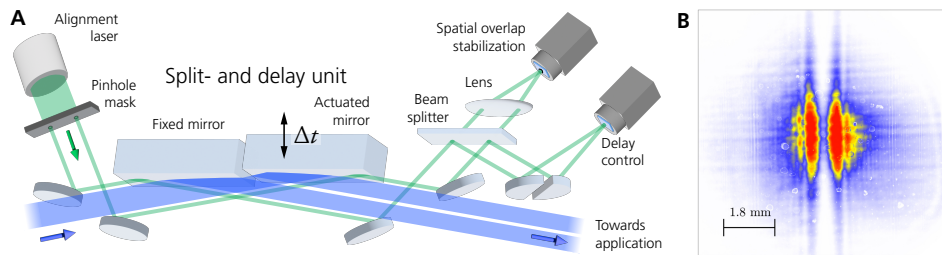

Figure 3.15: Schematic of the split-and delay unit and resulting XUV beam. (A) Drawing of the split and delay unit. The XUV beam is split into two parts of equal intensity, while a green laser runs parallel to the beam, passing through the unit for measuring beam pointing and relative delay between the fixed mirror and the actuated one. To simplify the drawing, the IR is not included. **(B)** XUV spatial profile captured with the XUV CCD camera. The cut in the center results from the gap between the two plates of the SDU.

Figure 3.15 shows the SDU including the feedback control beams. A green diode laser with the same divergence as the HHG radiation passes through a pinhole mask, generating two small laser beams. The beams are guided onto the SDU, where each beam is

reflected by one of the mirrors. After passing through the SDU, the beams go through a beamsplitter. A portion of each beam is then focused onto a camera through a lens system with a demagnification factor of $M = 35$, imaging the harmonic source point and simulating the properties of the Wolter optics employed later in the experiment. This portion of the beams provides feedback for stabilizing the spatial overlap using the actuated mirror.

The remaining portion of the beams is projected onto a camera chip at an additional angle between them, without focusing. The shift in the interference pattern of these beams is used to measure the relative delay between both mirrors in the SDU assembly. A control loop with the piezo tips allows for a temporal scan resolution of 10 as to 28 as with a range of 52 fs [116, 117]. The picomotors installed in 2021 extend the range to go far beyond that.

Wolter optics

The refocusing optics within the application chamber, commonly referred to as Wolter optics, consist of two toroidal mirrors arranged in a Wolter configuration [113, 118]. Each mirror deflects the beam under a 15 ° grazing incidence angle, leading to a total deflection between the incoming and exiting beam of 60 °. This grazing incidence angle is chosen to enable a high reflectivity in the XUV region, that is approximately 60% per reflection in the region from 30 to 50 eV [119].

The toroidal design of the mirrors features two different radii of curvature in the tangential and sagittal directions. When light strikes a mirror at an angle, the cylindrical symmetry is broken as the footprint on the mirror's surface becomes elliptical. This leads to asymmetric focusing when using a spherical mirror, resulting in strong astigmatism. The different curvatures in the two directions of the toroidal compensate for this asymmetry, allowing rays in both planes to focus at the same point with minimal aberrations.

Figure 3.16 is a schematic of the Wolter optics, highlighting its three pivoting and two translation axes. The optical system has an object arm length of 6 m (distance to the source position) and an image arm length of 170 millimeters, producing a demagnification factor of 35[113, 120]. The imaging point is strategically placed in the center of the application chamber, aligning with the point of interaction with the target, the detection assembly, and the XUV spectrometer.

The assembly is equipped with five axes of actuation, allowing for aberration compensation and optimization of the spot size in the interaction region. Paper [113] contains a characterization of the optics that links the axes noted in Figure 3.16 B with Zernike

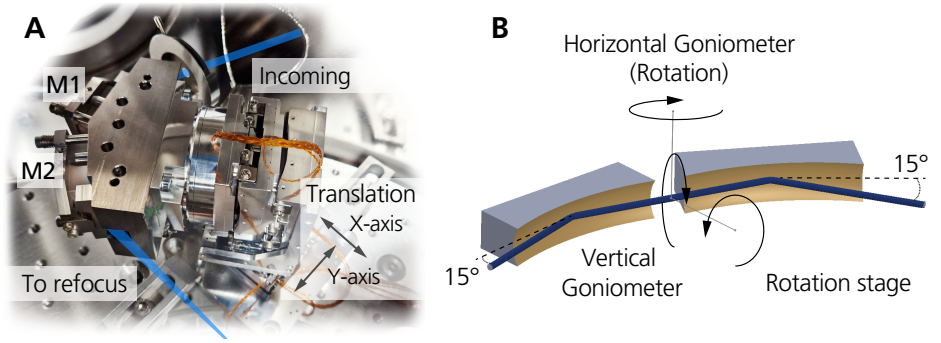

Figure 3.16: Schematic of the Wolter optics. (A) Photo of the Wolter optics assembly. The beam enters from the top right, and is deflected toward the center of the application chamber. The assembly is mounted on a two-axis translation stage, of which the Y-axis is aligned with the incoming beam. **(B)** Schematic of the mirror assembly, highlighting its three pivot axes that are used for optimizing the alignment.

polynomials. It is shown that the rotation mainly affects the $45\,^\circ$ astigmatism, while the horizontal goniometer affects the $0\,^\circ$ astigmatism. The vertical goniometer impacts the $45\,^\circ$ as well, but to a smaller degree than the rotation. The two translation stages align the assembly position, with the y-axis running parallel to the incoming beam. The design even allows for compensating for initial aberrations of the XUV, resulting in a spot size of $3.6 \times 4.0\,\mu\mathrm{m}^2$ (FWHM) [113].

Double-sided velocity map imaging spectrometer

The Double-Sided Velocity Map Imaging Spectrometer (DVMIS) is the primary detection instrument of the beamline, capable of recording the time of flight (ToF) and momentum of both photoelectrons and ions simultaneously, as an extension of a single-sided VMIS, as presented by [121]. A detailed description of the assembly and its design can be found in [122]. Figure 3.17 illustrates the central section of the device. In the interaction region in the middle, the laser pulses interact with a high-density target gas jet, released by an Even–Lavie valve [123, 124], resulting in the ejection of photoelectrons and ions.

Each side of the DVMIS consists of an extractor and a flight tube, configured with a floating ground- an electrically isolated reference point that allows for independent control of the electrical potential relative to the vacuum chamber grounding. At the end of the flight tube is a microchannel plate (MCP)-phosphor screen assembly, which detects the particles. When charged particles impact the MCP, they are multiplied through secondary emission, similar to an electron multiplier. The amplified electron signal is made visible by a phosphor screen and captured by cameras.

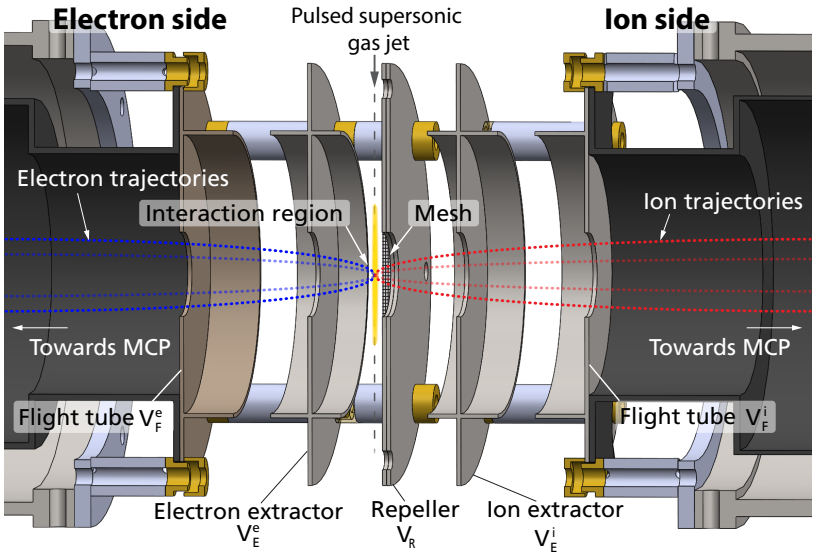

Figure 3.17: Center section of the DVMIS. The focused XUV/IR pulse meets the supersonic gas within the interaction region. The subsequently released photoelectrons and ions are pushed/dragged by the repeller toward the corresponding side. After propagation through the flight tubes, the charged particles are registered on an MCP/phosphor screen assembly (not in the picture). The corresponding trajectories are illustrated by dashed lines. Modified from [122].

In principle, both sides of the DVMIS can detect negatively or positively charged particles. However, one side contains a repeller plate with a conductive mesh, which is the side designated for ion detection. When a negative potential is applied to the repeller, electrons are accelerated toward the opposite (electron-detection) side, while ions are attracted to the ion side. Both sides feature an extractor plate that acts as an electrostatic lens, and a flight tube. The ratio between repeller and extractor voltages determines the operating mode of the system.

In spatial mode, the impact position of the charge carriers on the detector screen approximates the initial ionization position. This mode is particularly useful for alignment purposes, such as aligning the imaging position of the Wolter optics with the target or confirming the overlap between both beams originating from different arms of the interferometer.

In the Velocity Map Imaging (VMI) mode, the voltage ratios are tuned so that the detector position of the charge carriers corresponds to their initial ionization momentum. In this mode, spatial information about the ionization site is largely irrelevant, provided that the interaction occurs within the central region of the assembly where the electrostatic field is homogeneous.

The initial voltages for the different imaging modes are derived from simulations, as

shown in [122], and are optimized in the experiment. The detection range depends on the imaging mode, and can reach a kinetic energy of up to $\approx 90\,\mathrm{eV}$ for electrons, and $\approx 10\,\mathrm{eV}$ for ions.

The flight tube allows particles with different mass and charge to separate temporally while propagating toward the detector, which allows to identify them based on the time they impact the screen. A time-of-flight signal can be recorded by measuring the detector current as a function of time. Although this method is technically possible for both electrons and ions, it is practically only feasible for ions due to their significant mass differences. For electrons, time-of-flight separation is challenging because they all share the same charge-to-mass ratio, resulting in minimal temporal spread, making distinguishing them impractical.

XUV spectrometer

The spectrometer is positioned at the very end of the beamline and consists of a concave Hitachi grating with 600 lines/mm [125], which can be introduced via a closed-loop translation stage and aligned using a rotation stage. The grating disperses the harmonic orders onto a MCP-phosphor screen assembly, where the resulting diffraction pattern is imaged by a camera. Alternatively, the grating can be moved out of the beam path, allowing the beam to propagate toward the XUV camera.

Figure 3.18 A presents the recorded spectral image for harmonics generated with the CPA laser in argon, as captured by the camera. Panel B shows the integrated spectrum as a function of the diffraction axis for both the decommissioned CPA system, and the OPCPA laser system. Due to the broad energy range covered by the harmonics, some second-order diffraction spots of higher harmonic orders appear near the lower-order diffraction spots. While it is possible to clearly distinguish the second orders in the case of the CPA laser, they become difficult to resolve for the much broader harmonics generated by the OPCPA laser system. The increased spectral width of the harmonics is a direct result of the shorter pulse duration.

A tin filter, combined with an aluminum filter, reduces the presence of most harmonics, leaving primarily order 15, with order 13 remaining but significantly weaker. This filtering allows for identification of the harmonic orders and can be useful in specific experiments.

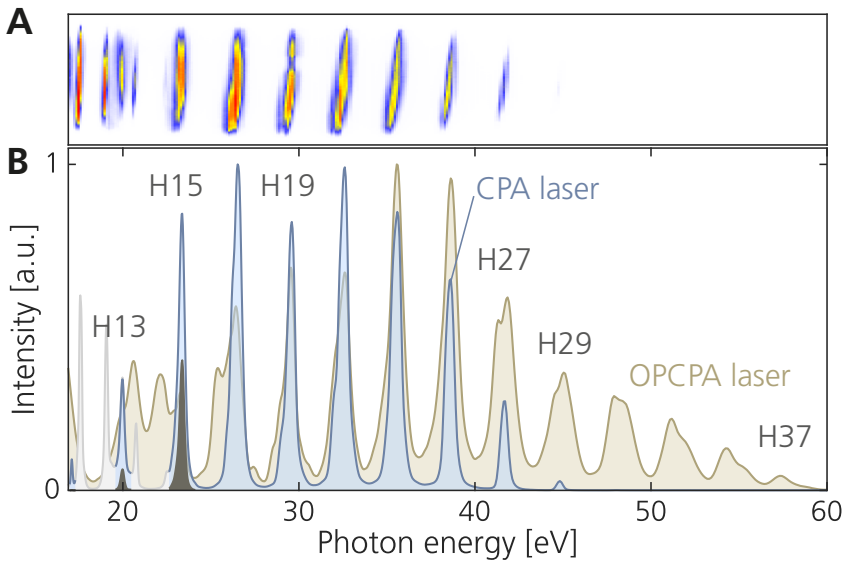

Figure 3.18: Spectrum of the XUV. (A) XUV spectrum as imaged on the MCP-phosphor assembly. **(B)** Integrated XUV spectrum generated in argon, filtered by a 200 nm aluminum film for the CPA laser (blue), and the OPCPA laser system (olive). With an additional 200 nm tin filter, the spectrum for is reduced to two harmonics (dark gray). The curved grating produces second-order diffraction spots around 20 eV, which can be identified for the CPA laser (light-gray regions). For the OPCPA laser they are blending in with the lower-order harmonics and cannot be distinguished.

3.2.4 Estimation of the XUV energy

Reliable measurement of XUV energy is crucial, as it enables the determination of conversion efficiency, guides the optimization of generation conditions during the experiment, and allows experimental observations to be compared with those in other publications and theoretical predictions.

Due to its high photon energy, XUV typically causes direct ionization upon interaction with matter, leading to absorption that renders transmitting optics unsuitable. Periodic multilayer mirrors can offer peak reflectivities of greater than 70 % [126], but only within a narrow optimized bandwidth that does not cover the broad spectral range of HHG. Specifically designed periodic multilayer mirrors can support the broad bandwidth and offer the ability to compensate for the intrinsic attochirp, reducing the pulse duration toward the Fourier-transform limit [127–129]. However, their reflectivity remains low - under 20 % for the range applicable to the intense XUV beamline - which is challenging when aiming for high-intensity pulses. Grazing-incidence mirrors provide broadband reflectivity that, depending on the grazing angle and surface material, can easily exceed 50 % [119].

Multiple reflections along the beam path, as illustrated in Figure 3.19, significantly re-

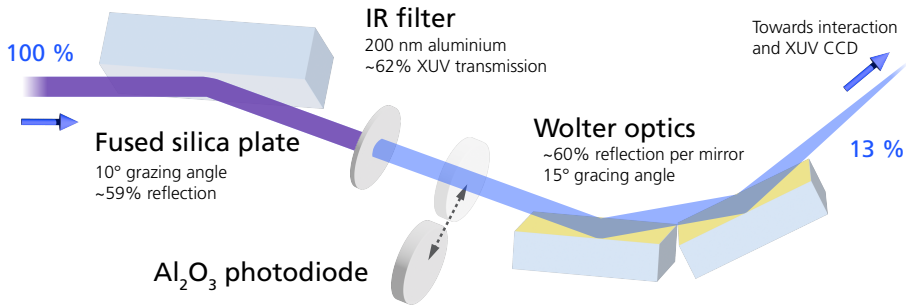

Figure 3.19: Schematic of elements affecting XUV flux from generation to application. After the reflections on a silica plate, filtering through a 200 nm aluminum filter and refocusing through the Wolter optics, only 13% of the generated XUV intensity remains.

duce the XUV energy reaching the target compared to the initially generated amount. Three key elements are used to steer, delay, and filter the XUV from the IR, each contributing to XUV intensity losses: fused silica plates in the SDU, an aluminum film for IR filtering, and the Wolter refocusing optics. The XUV-CCD camera is located further downstream, beyond the refocusing spot. Reflectivity values are calculated using the XUV spectrum and values from reflectivity data tables [119]. The amount of XUV that finally reaches the target is approximately 13 % of what has been generated.

There are two methods for measuring pulse energy at the Intense XUV beamline: a calibrated IR-blind photodiode (position indicated in Figure 3.19) and an XUV-CCD camera, which is used primarily to image the spatial profile of the XUV, but it also provides a response that is linear to the signal and can be used for an XUV energy estimation.

IR-blind photodiode

The IR-blind photodiode consists of a silica substrate disk with a thin Al/Al_2O_3 photocathode, designed for extreme ultraviolet (EUV) detection, and has a known calibration curve [130, 131]. To convert the diode signal to a pulse energy, the spectrally-weighted diode responsivity must be determined. Figure 3.20 shows a typical XUV spectrum, calibration points from the data sheet, and the interpolation used to calculate the spectrally weighted responsivity. As the calibration data only covers the range above 25 eV, it is assumed that the responsivity plateaus for energies below this value.

The spectrally weighted responsivity is derived by multiplying the interpolated spectral

response from the diode calibration sheet by the normalized spectrum:

$$R_{\text{eff}} = \int S(\lambda) R(\lambda) d\lambda \, . \tag{3.2}$$

Using this approach, the spectrally weighted responsivity is calculated to be $4.73\,\mathrm{mA/W}$.

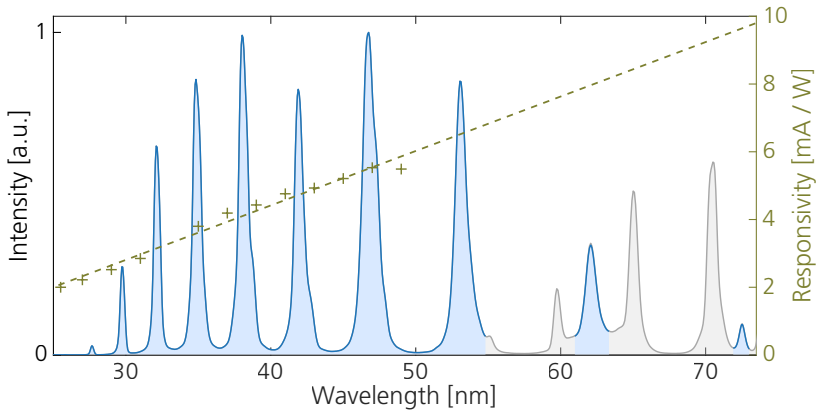

Figure 3.20: Responsivity of the IR blind photodiode: The plot shows a typical HHG spectrum (blue peaks) with the second order diffraction (grey) and the calibration points from the diode' s data sheet (green crosses) [131]. The interpolation (dashed line) assumes plateau in responsivity for lower photon energies, and a linear regression over the range of the calibration data. The spectrally weighted responsivity is $4.73\,\mathrm{mA/W}$.

Since the photodiode current I is in the μA range, a transimpedance amplifier is used to convert the current into a voltage V_{TIA} that is proportional to the current and amplified by a gain factor G. This voltage is measured using an oscilloscope, as plotted in Figure 3.21, and by integrating this signal over time, the measured charge (Q) is determined. The XUV pulse energy is calculated by dividing the photodiode charge by its responsivity:

$$E = \frac{Q}{R_{\text{eff}}} = \frac{\int V_{\text{TIA}}(t) dt}{G R_{\text{eff}}} \, . \tag{3.3}$$

From this measurement, the XUV photon energy that is not filtered by 200 nm aluminium is determined to be 2.54 nJ, which reduces to 1.60 nJ after aluminium filtering, corresponding to an XUV transmission of 63%. This result aligns well with the database prediction for the transmission of 200 nm aluminium that is 62%, according to [119].

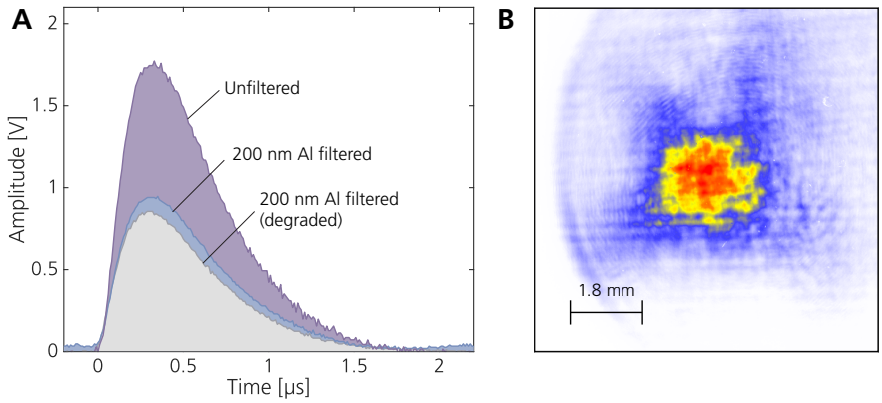

Figure 3.21: Measurements of the pulse energy. (A) Transimpedance amplifier signal from the calibrated IR-blind Al_2O_3 photodiode. The different curves represent a measurement with two different IR-filters and without filtering. **(B)** Spatial image from the XUV on the CCD camera. The curved edge on the left side in the image is an artifact from one of the holey mirrors in the interferometer chamber.

Filters degrade over time as a result of surface contamination and oxidation, reducing their transmission. For a filter that has been in the setup for about a year, the measured transparency shows only a pulse energy of $1.26\,\mathrm{nJ}$— more than $20\,\%$ less compared to a new filter.

XUV CCD camera

Another option for monitoring the XUV energy is the XUV CCD camera located at the end of the beamline. The XUV beam is directly imaged using an Andor iKon-L SO camera, which features a $27.6\,\mathrm{mm} \times 27.6\,\mathrm{mm}$ sensor with a resolution of $4.2\,\mathrm{MP}$ [132]. This camera is mounted on a flange approximately $850\,\mathrm{mm}$ (5 focal lengths) downstream from the XUV focus, attached to the application chamber.

The number of XUV photons N_{ph} can be estimated using the signal count rate N_{counts} and spectrum-specific device parameters

$$N_{\mathrm{ph}} = \frac{N_{\mathrm{counts}}\, SN}{N_{\mathrm{e-h}}\mathrm{QE}}\,, \tag{3.4}$$

using the sensitivity value SN that depends on the camera readout rate and gain settings, and a wavelength-dependent quantum efficiency that is estimated to be $QE = 0.7$, both derived from the data sheet of the sensor. Further, each incident photon generates a specific number of electron-hole pairs, $N_{\mathrm{e-h}}$. This number is obtained by dividing the average photon energy by the energy that is required to generate an electron-hole pair in silicone ($3.65\,\mathrm{eV}$):$N_{\mathrm{e-h}} = E_{\mathrm{ph}}/3.65\,\mathrm{eV}$. Given the number

of photons and their average energy, the pulse energy can be determined by simple multiplication.

For a measurement taken simultaneously with the above photodiode measurements, the XUV CCD camera recorded a calculated pulse energy of $5.25\,\mathrm{nJ}$. However, the photodiode positioned before the Wolter optics measured a pulse energy of $1.60\,\mathrm{nJ}$ for the IR-filtered beam. Given that the Wolter optics are expected to transmit approximately $36\,\%$, the estimated pulse energy at the height of the XUV camera would be $0.576\,\mathrm{nJ}$ based on the diode measurement. This is about a factor of 10 lower than the pulse energy derived from the camera measurements.

A possible explanation for this difference is the relatively high age (about 8 years) of the diode, and the high likelihood that the active surface has undergone some aging leading to a significant reduction in responsivity. A possible explanation for this difference is that the diode's active surface has likely undergone aging over time, leading to a significant reduction in responsivity. Given the Al/Al_2O_3 structure, exposure to air or contamination can alter the oxide layer, affecting the photoemission efficiency. Such a strong discrepancy underscores the inherent challenges in accurately determining XUV energy and highlights the need for caution when making related claims.

3.3 The SYLOS GHHG LONG beamline at ELI-ALPS

The Gas High Harmonic Generation (GHHG) Beamline is a part of the ELI-ALPS user facility in Szeged, Hungary. Developed in collaboration between Lund University and ELI-ALPS, the setup is an expanded version of the Intense XUV beamline in Lund [133]. Two experimental campaigns were conducted at the beamline, one of which resulted in Paper IV.

Following the scaling principles described in Section 2.7, the HHG conversion efficiency can be maintained when the focal length is increased by a factor of η, the medium length and input energy are scaled by η^2, and the gas density is reduced by a factor of $1/\eta^2$. This requires high-intensity XUV beamlines to be large in scale and is the reason for the long focal length of the SYLOS GHHG LONG beamline. Figure 3.22 presents a simplified schematic of the setup, excluding certain beam manipulation elements near the end of the beamline, such as the interferometer and refocusing optics.

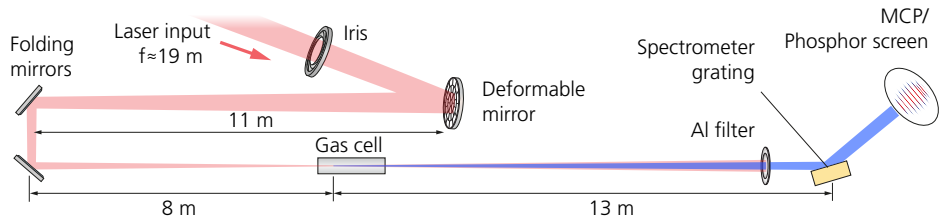

Figure 3.22: Simplified schematic of the SYLOS GHHG LONG beamline at ELI-ALPS. The laser is focused by a mirror with a focal length of 19 m in the short-focus configuration. After passing through the generation medium, the resulting beam is IR-filtered and its spectrum is monitored by a spectrometer.

The GHHG LONG Beamline operates with either the SYLOS laser system (pulse energy = 32 mJ, repetition rate = 1 kHz) or the SEA (SYLOS Experiment Alignment) laser (pulse energy = 40 mJ, repetition rate = 10 Hz). The beamline features two distinct focusing geometries: a "short" and a "long" focus. The short focusing geometry provides a focal length of 19 m, leading to a scaling factor of $\eta \approx 2.2$ compared to the 8.7 m focal length in the Lund setup. This short focal length configuration uses a generation gas target cell that can vary in length from 32 cm to 78 cm, allowing for optimal control over the gas medium properties and the phase matching conditions [85, 133].

In contrast, the long focusing geometry provides an extended 55 m focal length and includes a gas cell system spanning 6 m. This gas system consists of 15 separate cells, each independently adjustable in terms of gas type and pressure, allowing precise control of phase matching and generation conditions along the entire target length.

As in the Intense XUV Beamline, the SYLOS GHHG LONG beamline incorporates a compact XUV–IR interferometer. This interferometer includes an XUV mirror that can function as a split-and-delay unit, enabling XUV–XUV pump-probe experiments to explore nonlinear dynamics. Following the interferometer section, the beam is refocused into the interaction region via a Wolter-type toroidal mirror setup. Sample injection into the XUV refocusing spot is achieved with an Even–Lavie valve. The generated charged particles are subsequently detected by an Electron time-of-flight detector.

Chapter 4

Properties of High-Order Harmonics

Attosecond pulses result from the coherent sum of high-order harmonics. Consequently, understanding the phase characteristics of these harmonics is crucial for shaping the attosecond pulse. Their generation, propagation, and focusing onto a target must be well understood to optimize HHG-based applications such as attosecond pulse generation, coherent diffractive imaging, and pump-probe experiments.

This chapter provides a structured overview of the spatial and phase-matching properties of high-order harmonics, beginning from the fundamental description of the driving laser beam. We first review Gaussian beam optics, establishing the mathematical framework needed to describe wavefront evolution. Using this foundation, we apply the γ-model as an analytical approach to quantify harmonic wavefront curvature and its dependence on laser intensity and generation conditions. Theoretical predictions from this model are then compared with experimental measurements, with emphasis on harmonic focusing behavior in harmonic propagation, as discussed in **Paper III**.

Next, we examine how wavefront aberrations in the driving laser, particularly astigmatism, influence harmonic beam profiles. By characterizing these effects, we show how they give rise to complex spatial structures in the harmonic beam, linking to findings presented in **Paper I**. Furthermore, we explore beam shaping using a flat-top intensity distribution, which can mitigate phase distortions and reduce chromatic aberrations, as presented in **Paper II**. The impact of out-of-focus harmonic generation is also discussed as a strategy to incorporate the higher IR intensity of the OPCPA laser system.

Finally, we conclude with a discussion on phase matching, emphasizing the interplay between pressure, medium length, and driving laser intensity in optimizing harmonic yield. By identifying distinct phase-matching regimes, we establish a framework for achieving efficient HHG under different experimental conditions. These theoretical findings are validated experimentally in **Paper IV**.

Together, these theoretical and experimental insights provide a comprehensive understanding of harmonic beam formation and propagation, which is required for advanced applications in ultrafast and nonlinear XUV science.

4.1 Description of a Gaussian driver

A precise description of high-order harmonics requires a thorough characterization of the driving laser beam. Gaussian beams are especially suitable for this purpose due to their well-defined analytical properties. The expressions introduced in this section are based on fundamental optics principles, as presented in [73]. However, they are included here to establish a foundation for the discussions in the following sections.

The beam width of a Gaussian beam along the propagation axis z follows

$$w(z) = w_0 \sqrt{1 + \left(\frac{z}{z_\mathrm{R}}\right)^2} \,, \tag{4.1}$$

where w_0 is the minimum beam width (waist), and z_R the Rayleigh range. The Rayleigh range is the distance from the waist at which the beam width increases by a factor of $\sqrt{2}$, and it is linked to the wavelength λ as:

$$z_\mathrm{R} = \frac{\pi w_0^2}{\lambda} \,. \tag{4.2}$$

The full expression of the electric field of a Gaussian beam is:

$$E(x,y,z) = A_0 \frac{w_0}{w(z)} \exp\left(-\frac{r^2}{w^2(z)}\right) \exp\left[-ikz - ik\frac{r^2}{2R(z)} + i\xi(z)\right], \tag{4.3}$$

with the radial coordinate $r = \sqrt{x^2+y^2}$, and the wavenumber $k = 2\pi/\lambda$. The first factor represents the constant field amplitude A_0 that changes with z as $w_0/w(z)$. The second factor is the transverse spatial profile, describing the intensity variation in the radial direction. The third factor describes the phase, and consists of three components: the longitudinal phase kz, the radial phase curvature $k\frac{r^2}{2R(z)}$, and the Gouy phase shift $\xi(z)$. The radius of curvature follows

$$R(z) = z\left[1 + \left(\frac{z_\mathrm{R}}{z}\right)^2\right] \,. \tag{4.4}$$

The wavefront curvature is the reciprocal of the radius of curvature. The Gouy phase introduces a π-phase shift as the beam goes through the focus and is described by

$$\xi(z) = \tan^{-1} \frac{z}{z_\mathrm{R}} \,. \tag{4.5}$$

The most rapid phase shift happens in the proximity of the focus. Within the range from $-z_\mathrm{R}$ to z_R, the Gouy phase changes approximately from $-\pi/4$ to $\pi/4$.

Figure 4.1 illustrates the beam width evolution and wavefront curvature of a Gaussian beam as it propagates through the focal region. The curvature of the wavefront is nearly flat both very close to and far from the beam waist. However, at $\pm$ one Rayleigh range, the absolute value of the radius of curvature $|R(z)|$ reaches its minimum, corresponding to the point where the wavefront exhibits the strongest curvature.

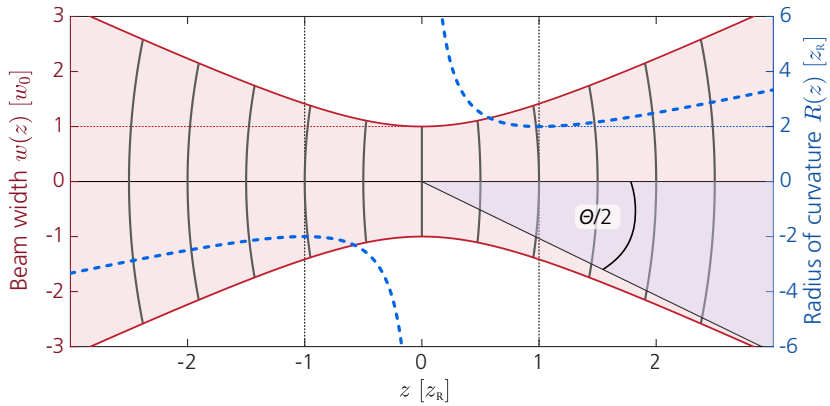

Figure 4.1: Evolution of a Gaussian beam along propagation. The beam width (red solid) is at its minimum at the waist (horizontal dotted line). The radius of curvature (blue dashed line) is smallest at the Rayleigh range (vertical dotted lines) and increases toward the focus and at large distances. The curvature of the beam (dark-gray solid lines) is nearly flat close to and very far away from the focus, but reaches a maximum at the Rayleigh range. The angle θ marks the divergence of the beam.

The intensity $I(z)$ of a Gaussian beam is the absolute square of its complex amplitude:

$$I(x, y, z) \propto \left| A_0 \frac{w_0}{w(z)} \exp\left(-\frac{r^2}{w^2(z)} \right) \right|^2 \,. \tag{4.6}$$

If the radius of curvature $R(z')$ and beam width $w(z')$ at a given propagation distance z' are known (from either simulations or measurements), the focus position and beam waist can be determined from the following relations:

$$z\,(w_0) = \frac{R(z')}{1 + \left(\frac{\lambda R(z')}{\pi w^2(z')} \right)^2}, \qquad \text{and} \qquad w_0 = \frac{w(z')}{\sqrt{1 + \left(\frac{\pi w^2(z')}{\lambda R(z')} \right)^2}} \,. \tag{4.7}$$

These equations provide a fundamental framework for characterizing the spatial and phase properties of the driving laser beam.

4.2 Description of high-order harmonics

In this section, we derive a description of high-order harmonics under the assumption that they inherit the characteristics of the Gaussian driver. We derive expressions for the harmonic phase and width at the point of generation, which in turn allow us to determine the focus position and waist of the different harmonic order beams. Using the terminology defined in the previous section, we can now reconstruct the spatial and spectral properties of the harmonics at any point along the propagation axis.

4.2.1 Phase structure of high-order harmonics

At the generation position z_{gen}, the phase of the q-th harmonic is given by the sum of the phase of the driving laser, scaled by the harmonic order q, and the harmonic dipole phase contribution, which depends on the electron excursion in the continuum [52]:

$$\Phi_q(r, z_{\text{gen}}) = q\phi(r, z_{\text{gen}}) + \Phi^{\text{s,l}}(r, z_{\text{gen}}) \ , \tag{4.8}$$

where $\phi(r, z)$ is the spatial phase of the fundamental beam, as given in Equation 4.3:

$$\phi(r, z) = kz + k\frac{r^2}{2R(z)} - \xi(z) \ , \tag{4.9}$$

and $\Phi^{\text{s,l}}(r, z)$ the dipole phase for short (s) or long (l) trajectories. According to the γ-model (Equation (2.13) in Section 2.3), the harmonic dipole phase is

$$\Phi^{\text{s,l}}(\Omega) = \alpha^{\text{s,l}} I + t_p^{\text{s,l}} \left(\Omega - \Omega_p\right) + \frac{\gamma^{\text{s,l}}}{I}(\Omega - \Omega_p)^2 \ . \tag{4.10}$$

Here, the intensity gradient in the radial direction plays a crucial role as it produces a spatial variation in the dipole phase across the beam profile. Using the definition for the Gaussian driving laser intensity from the previous section, we substitute Equation (4.6) into Equation (4.10) and introduce $I_0 = A_0^2$. This yields an expression for the dipole phase of a single harmonic with photon energy Ω

$$\Phi^{\text{s,l}}(r, z_{\text{gen}}) = \alpha^{\text{s,l}} \frac{I_0 w_0^2}{w^2(z_{\text{gen}})} e^{-\frac{2r^2}{w^2(z_{\text{gen}})}} + \frac{\gamma^{\text{s,l}} w^2(z_{\text{gen}})}{I_0 w_0^2} e^{\frac{2r^2}{w^2(z_{\text{gen}})}} \left(\Omega - \Omega_p\right)^2 . \tag{4.11}$$

To allow an analytical description of the radius of curvature, we perform a Taylor expansion around the center, $r = 0$:

$$e^{\pm 2r^2/w^2(z_{\text{gen}})} \approx \sum_{n=0}^{N} \frac{1}{n!} \left(\pm \frac{2r^2}{w^2(z_{\text{gen}})} \right)^n . \tag{4.12}$$

Higher-order expansion terms contribute to the description of the far-field spatial profile of harmonics, as discussed in Section 4.4.3 and Paper I. However, since their effect is not essential at this stage of the discussion, we restrict our expansion to the second order, yielding $\exp(\pm 2r^2/w(z_{\text{gen}})^2) \approx 1 \pm 2r^2/w(z_{\text{gen}})^2$. The terms that do not depend on r^2 represent a global phase shift that is uniform across the beam and does not impact the spatial variation of the phase. Hence, they can be neglected when deriving a description of the harmonics' propagation and divergence. Neglecting terms that do not depend on r^2, we find the dipole phase:

$$\Phi^{\text{s,l}}(\Omega) = -\alpha^{\text{s,l}} \frac{I_0 w_0^2}{w^2(z_{\text{gen}})} \frac{2r^2}{w^2(z_{\text{gen}})} + \frac{w^2(z_{\text{gen}})}{I_0 w_0^2} \frac{2r^2}{w^2(z_{\text{gen}})} \gamma^{\text{s,l}} \left(\Omega - \Omega_p\right)^2 . \tag{4.13}$$

Simplifying by canceling common factors and substituting into Equation (4.8) along with the fundamental phase, yields:

$$\Phi_q(r, z_{\text{gen}}) = q \frac{kr^2}{2R(z_{\text{gen}})} - \alpha^{\text{s,l}} \frac{2r^2 I_0 \omega_0^2}{w^4(z_{\text{gen}})} + \frac{2r^2}{I_0 w_0^2} \gamma^{\text{s,l}} \left(\Omega - \Omega_p\right)^2 . \tag{4.14}$$

This expression describes the harmonic phase, incorporating the intensity dependence from the γ-model. To fully describe how harmonics propagate, we assume they exhibit Gaussian behavior. This means that, as for Gaussian beams, their propagation can be determined by just two parameters: the beam width and the radius of curvature at a given location z.

4.2.2 Harmonic wavefront and propagation

Having established the harmonic phase structure, we now examine how it influences the wavefront properties. A key factor in this evolution is the radius of curvature, which determines whether the beam remains collimated, converges, or diverges.

If we assume that each harmonic has a Gaussian intensity profile, we can treat its curvature as that of a Gaussian beam. This allows us to equate the r^2-dependent part of the phase in Equation (4.3) with the harmonic phase of a Gaussian:

$$\Phi_q(r, z_{\text{gen}}) = \frac{qkr^2}{2R_q(z_{\text{gen}})} , \tag{4.15}$$

and solve for the harmonic radius of curvature, using $qk = \Omega/c$:

$$\frac{1}{R_q(z_{\text{gen}})} = \frac{1}{R(z_{\text{gen}})} - \frac{4\alpha^{s,l} I_0 w_0^2 c}{w^4(z_{\text{gen}})\Omega} + \frac{4\gamma^{s,l}\left(\Omega - \Omega_p\right)^2 c}{I_0 w_0^2 \Omega} \,. \tag{4.16}$$

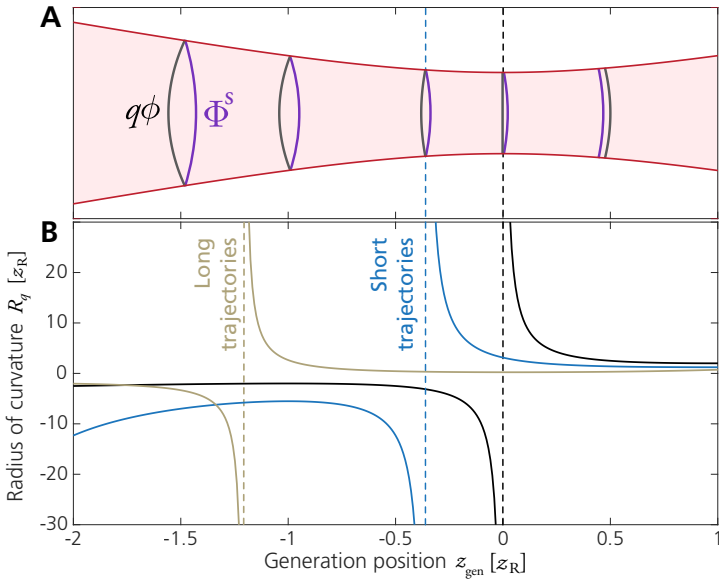

Figure 4.2: Wavefront and radius of curvature across generation position. **(A)** Curvature of the harmonic wavefront originating from the fundamental wavefront phase $q\Phi$ (black) and from the dipole phase Φ^S of the short trajectory (violet). **(B)** Radius of curvature for the fundamental (black), and the radius of curvature including dipole phase contributions from the short (blue) and long (olive) trajectories. The vertical dashed lines indicate positions where the wavefront is flat (i.e., where the radius of curvature is infinite) for the fundamental, short, and long trajectories.

Figure 4.2 A illustrates the beam width of the fundamental along the propagation axis, along with the wavefront curvature contributions from the driving laser (black) and the harmonic dipole phase (violet) for the short trajectory. Panel B depicts the radius of curvature for the fundamental (black) and the radius of curvature resulting from the dipole phase for the short (blue) and long (olive) trajectories.

The black dashed line marks the focus of the fundamental beam, where its wavefront curvature is flat. The blue dashed line indicates the generation position where the phase contribution of the fundamental beam exactly cancels out the harmonic dipole phase for the short trajectory. As shown in Panel A, the harmonic wavefront at this position becomes flat, corresponding to an infinite radius of curvature. This defines the harmonic focus, where the beam width reaches its minimum (waist). At this point, the generation position coincides with the harmonic source position—unlike other

generation positions, where the harmonic focus is located elsewhere. A similar point exists for the long trajectory (olive dashed line) but occurs at a different generation position.

The simulations for Figure 4.2 use a peak intensity of $2 \times 10^{14}\mathrm{Wcm}^2$ with a $\lambda = 800\,\mathrm{nm}$ driver to calculate the radius of curvature of the $q = 21$st harmonic.

To express the dipole in a more compact form, we can only consider short trajectories, for which we find $\alpha^s = 0$ [52], and introduce the dipole phase coefficient Γ, defined as:

$$\Gamma = \frac{\gamma^s \left(\Omega - \Omega_p\right)^2 w^2 \left(z_{\mathrm{gen}}\right)}{I_0 w_0^2} \,. \tag{4.17}$$

Substituting, we find a very compact description for the harmonic radius of curvature

$$\frac{1}{R_q\left(z_{\mathrm{gen}}\right)} = \frac{1}{R\left(z_{\mathrm{gen}}\right)} + \frac{4\Gamma c}{\Omega w^2(z_{\mathrm{gen}})}. \tag{4.18}$$

To determine the width of the harmonic at the generation position, we must account for the intensity scaling relative to the fundamental laser. This scaling is often described by a power law:

$$I_q = I^p \,, \tag{4.19}$$

where p is an empirically determined exponent that depends on both the generation gas and the harmonic order. In the plateau region, TDSE simulations show typical values of $p = 2.6$ for argon and $p = 5.5$ for neon [36].

If we assume a single exponent p for all plateau harmonics, the harmonic beam width at the generation position scales with the driver beam width via

$$w_q(z_{\mathrm{gen}}) = w(z_{\mathrm{gen}})/\sqrt{p} \,. \tag{4.20}$$

Under this approximation, all harmonic orders share the same initial beam width at the generation position. Any differences in their subsequent propagation—such as variations in focus position or waist—arise from the r^2-dependent phase terms (i.e., the harmonic wavefront curvature) and diffraction effects due to their different wavelength, rather than differences in their initial beam sizes.

4.2.3 Harmonic focus and beam waist

The wavefront curvature governs the evolution of the harmonic beam from its point of generation. If the curvature is converging, the harmonic focus lies beyond the

generation position and is a real focus. Conversely, if the curvature is diverging, the harmonic focus is located before the generation position and is therefore virtual.

In the previous steps, we derived expressions for the harmonic radius of curvature (Equation (4.16)) and harmonic width (Equation (4.20)) at the generation position z_{gen}. Assuming the harmonics behave as Gaussian beams, these two parameters fully determine their propagation, specifically the focal position and waist. Applying the Gaussian beam expressions from Equation (4.7), we obtain the harmonic focal position:

$$z_{0q} = z_{\text{gen}} - \frac{R_q(z_{\text{gen}})}{1 + \left(\frac{\lambda_q R_q(z_{\text{gen}})}{\pi w_q^2(z_{\text{gen}})}\right)^2}, \tag{4.21}$$

and the harmonic beam waist:

$$w_{0q}(z_{\text{gen}}) = \frac{w_q(z_{\text{gen}})}{\sqrt{1 + \left(\frac{\pi w_q^2(z_{\text{gen}})}{\lambda_q R_q(z_{\text{gen}})}\right)^2}}\,. \tag{4.22}$$

With this foundation, we simulate the positions of the harmonic focal points and waists for any generation position, as shown in Figure 4.3.

Panels A and C show the harmonic focus position and beam waist as a function of generation position without contributions from the harmonic dipole phase, i.e., with $\Gamma = 0$. In this scenario, the harmonics inherit only the curvature of the driver at the generation position. When generation occurs at the focus ($z_{\text{gen}} = 0$), the fundamental has a flat wavefront, and all harmonic orders share the same focus position.

Away from this point, the harmonics no longer focus at the same position as the fundamental, and pronounced differences between harmonic orders emerge when generation occurs within the Rayleigh range. The reason lies in the difference in wavelength among harmonic orders: for shorter wavelengths, the Rayleigh range increases, meaning that despite having the same initial wavefront and beam width, the beam focuses farther away compared to a longer wavelength. Strongly curved wavefronts lead to more rapid wavefront evolution, making the order-dependent focus shift effect due to different harmonic wavelengths more pronounced. Since the fundamental's wavefront curvature undergoes its strongest variation within the Rayleigh range, the differences in harmonic focus positions are largest in this region.

When generation occurs outside the Rayleigh range, the driver's curvature flattens, and the harmonic wavefronts evolve gradually over long distances. As a result, differences in phase accumulation remain small, and all harmonic orders focus at nearly the same position. For the same reason, far outside the focus ($z_{\text{gen}} \gg 0$), the harmonic foci approach the focus position of the fundamental.

The differences in waist size arise from the interplay between curvature and diffraction. As the variation in the fundamental beam's properties is symmetric with respect to the focus, the harmonic focus positions and waist sizes also vary symmetrically.

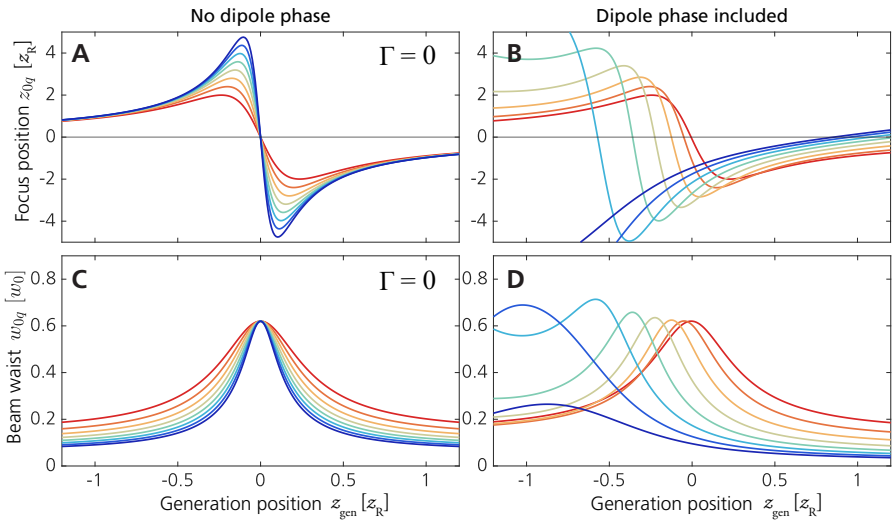

Figure 4.3: Harmonic focus position and waist as a function of generation position. Harmonic focus positions relative to the laser focus, shown in **(A)** without and in **(B)** with accounting for the harmonic dipole phase. **(C) and (D)** Harmonic beam waist without/with the dipole phase. The harmonic orders are color coded, covering harmonics 11 (red) to 25 (blue). The figures show the short trajectories using a peak intensity of $I = 1.5 \times 10^{14}$ W/cm^2.

Panels B and D of Figure 4.3 illustrate how the focus position and beam waist vary along the generation position, when the dipole phase contribution for short trajectories is taken into account.

The dipole phase introduces a divergent contribution to the wavefront curvature, varying with harmonic order and causing a spread in harmonic focus positions. This effect is particularly pronounced for $z_{\text{gen}} < 0$, where the fundamental beam's wavefront is converging. However, as the fundamental beam transitions through the focus, its curvature reverses and becomes diverging, aligning with the dipole phase contribution. As a result, the difference in focus positions between harmonic orders becomes less distinct. Unlike the case without a dipole phase contribution, there is no generation position—not even at the focus of the fundamental—where all harmonics share the same focus position.

The dipole phase also introduces additional variations in the beam waist size for different harmonic orders along the generation position axis, enhancing diffraction-induced variations. The order-dependent spread in both beam waist and focus position limits the ability to refocus the XUV into a tight focal region where all harmonics converge to a single, minimal spot size. As a result, these chromatic aberrations af-

fect both the achievable intensity upon refocusing and the temporal structure of the resulting attosecond pulse.

4.3 Experimental validation

In the preceding sections, we derived a description for high-order harmonics by assuming they exhibit Gaussian beam characteristics and inherit both the wavefront curvature and the beam properties of the fundamental, along with the intensity-dependent dipole phase contribution described by the γ-model. A key prediction of this model is that different harmonic orders exhibit distinct focal positions along the propagation axis—often referred to as chromatic aberrations. To verify these predictions experimentally, we performed knife-edge measurements at the Intense XUV Beamline in Lund, with results presented in **Paper III**.

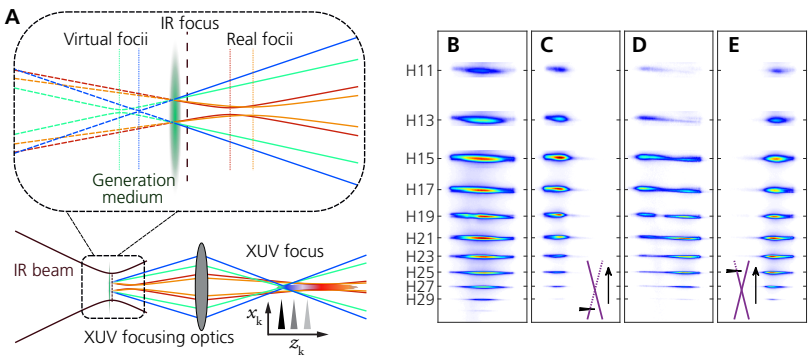

Figure 4.4: Principle of the knife-edge measurement. (A) Schematics of the experimental method. The generation position influences the way the HHG propagates, with the refocusing positions being spread out as the different harmonic orders diverge differently. The measurement is performed by moving a knife edge through the beam at different locations along propagation near the refocusing region. Modified from [52]. **(B-E)** Representative harmonic spectra at different knife-edge positions. When the knife edge is inserted far before or after the focus (panels (C) and (E)), all harmonic orders are clipped from the same side. Near the focus (panel (D)), higher orders are clipped from one side, while the lower orders are clipped from the opposite side, indicating that harmonic foci are distributed along z_k. Adapted from [134]

In this experiment, a thin metal blade (the knife edge) was translated through the refocused XUV beam at various positions along the propagation axis z_k. At each position, we recorded the harmonic spectrum as a function of knife edge insertion x_k. By noting which side of the harmonic beam was clipped as the knife edge moved in, we could determine whether the insertion plane was before or after each harmonic focus: when the knife edge is inserted before the focus, the beam appears cut from the opposite side on the spectrometer; when inserted after the focus, the cut appears on the same side. This principle is schematically illustrated in the lower portion of Figure 4.4 A. Panels B–E of Figure 4.4 show representative spectra without a knife

edge insertion (B) and at three selected positions along z_k. Notably, near the average focus (Panel D), lower harmonic orders are clipped from a different side than the higher orders, directly confirming the spread of focal points.

The integral of a Gaussian transverse profile clipped by a knife-edge is described by an error function. Consequently, the harmonic width was determined by fitting an error function to the individual harmonic yield as a function of knife-edge insertion x_k. Repeating this procedure at multiple z_k planes effectively mapps out the focal region of each harmonic order, enabling an accurate determination of their focal positions and waists. Additionally, the experiment's deformable mirror served as a control parameter by allowing the generation position to be tuned via adjustments to the fundamental beam's wavefront curvature. As seen in Figure 4.5, these parameter scans produce near-quantitative agreement between the experiment and theory for harmonic orders 11 through 25, supporting the validity of our approach. The data reveals a clear spread

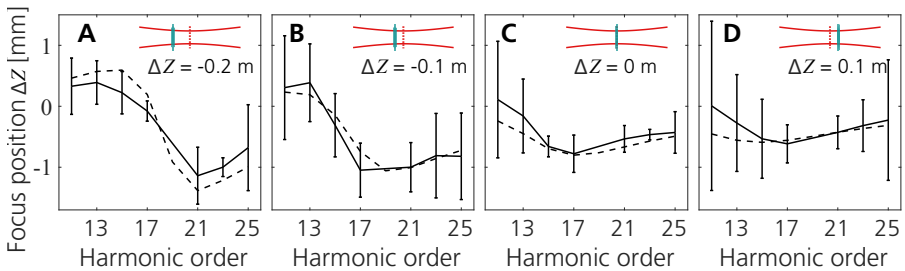

Figure 4.5: Focus positions for harmonic orders 11–25 at different generation positions. Measured focus positions are shown as solid lines; simulated positions are shown as dashed lines. (The 19th order is suppressed because it coincided with a dark spot on the detector.) When the generation occurs before the fundamental focus (panels **(A)** and **(B)**), the harmonic focal positions exhibit a larger spread. In contrast, generation at or after the focus (panels **(C)** and **(D)**) yields a narrower distribution of harmonic focal positions. Adapted from [134]

in the harmonic foci positions when the generation plane lies before the driving-laser focus—exactly as the model predicts for negative generation positions z_{gen}. By contrast, when z_{gen} coincides with or lies beyond the fundamental focus, the distribution of harmonic focal positions becomes much narrower. Minimizing the spread of harmonic foci is crucial for achieving strong spatial overlap, ensuring that all harmonic orders can be refocused onto a small spot. Since attosecond pulses result from the coherent sum of harmonic orders, this spatial confinement is essential for generating short and intense pulses.

The close agreement between measurement and simulation confirms that the model captures the essential physics of harmonic wavefront curvature, including the role of the dipole phase and the power-law scaling of harmonic beam widths. Hence, the knife-edge measurement provides a direct validation of our theoretical description of harmonic focusing and chromatic aberrations in HHG.

4.4 Impact of an astigmatic driving laser

Up to this point, we have assumed the driving laser's transverse amplitude and phase to be cylindrically symmetric, with $r = \sqrt{x^2 + y^2}$. In reality, however, laser beams often suffer from wavefront distortions, leading to aberrations. This is especially relevant in high-power laser systems, where nonlinear effects, such as self-focusing and self-phase modulation, as well as non-uniformities in the amplification process, can introduce significant aberrations. Given that the harmonic wavefront is fundamentally shaped by the wavefront of the driving laser, we now examine how driver aberrations affect the generated harmonics. This discussion follows the findings of **Paper I**, with a particular focus on astigmatism as the dominant form of aberration in the experiment.

4.4.1 Describing the fundamental with astigmatism

Aberrations are commonly quantified by Zernike polynomials, which provide a mathematical framework describing wavefront distortions in a given plane. These polynomials form an orthogonal basis on a unit circle, making them well-suited for approximating wavefronts in circular apertures. In this approach, the wavefront is expressed as a sum of polynomials indexed by radial order n and azimuthal order m, with each term corresponding to a specific type of aberration [135, 136]. Lower-order Zernike terms have specific names: the zeroth and first orders represent a phase shift (piston) and tilts in the x- and y-directions, respectively. Second-order terms describe defocus and astigmatism, while third-order terms include coma and trefoil, with higher orders accounting for increasingly complex aberrations.

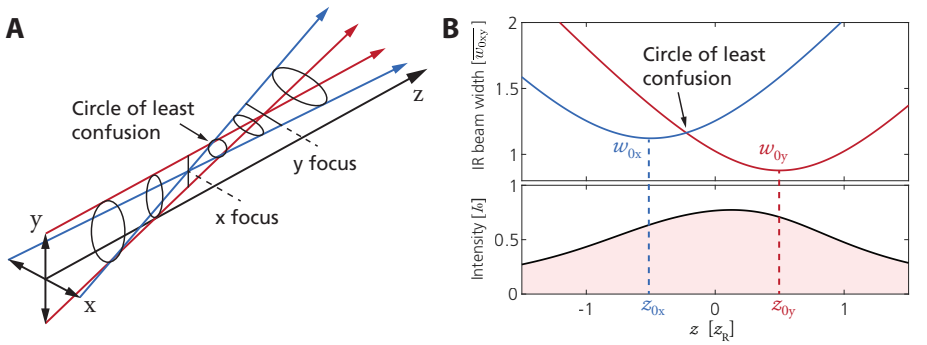

Figure 4.6: Properties of an astigmatic beam. (A) Visualization of an astigmatic beam with two distinct foci: one in the x-direction and the other orthogonally in the y-direction. Between these foci is one spot, denoted as the circle of least confusion, which is when both beam widths are equal. **(B)** Beam width along the propagation axis for the x- (blue) and y-direction (red). The intersection of the two curves represents the circle of least confusion. The bottom curve in panel (B) shows the intensity profile along the propagation axis.

In the case of astigmatism, the beam exhibits different curvatures along two orthogonal directions, leading to two separate foci displaced along the propagation axis. Additionally, each focus may have a slightly different waist size $w_{x,y}$, resulting in varying Rayleigh ranges $R_{x,y}$. Figure 4.6 illustrates the behavior of an astigmatic beam upon propagation, showing the evolution of the x- and y-axis components along the beam's path. These components are orthogonal, and we choose to assign the earlier focus with the x-direction. All values are expressed uniformly in terms of the average Rayleigh range or average beam waist.

To analyze the impact of an aberrated driver on high-order harmonics, we must adjust the Gaussian beam intensity description from Section 4.1 to incorporate separate waists and Rayleigh ranges in the x- and y-directions:

$$I(x,y,z) = I_0 \frac{w_{0x} w_{0y}}{w_x(z) w_y(z)} \exp\left(-\frac{2x^2}{w_x^2(z)} - \frac{2y^2}{w_y^2(z)}\right) , \tag{4.23}$$

with the corresponding phase:

$$\phi(x,y,z) = \frac{kx^2}{2R_x(z)} + \frac{ky^2}{2R_y(z)} . \tag{4.24}$$

With this refined description of the astigmatic driver, we can now analyze its direct impact on the phase properties of the harmonics.

4.4.2 Harmonic description with an astigmatic driver

Building on the derivation in Section 4.2, we now examine how the harmonic phase is influenced by both the driving laser's field phase—scaled by the harmonic order q—and the harmonic dipole phase contribution. To account for an astigmatic driver, we apply the non-uniform intensity distribution from Equation (4.23) instead of a cylindrically symmetric one.

As a result, the harmonic phase will have different contributions in the x- and y-axis with two distinct harmonic radii of curvature

$$\phi_q^{(2)}\left(x,y,z_{\text{gen}}\right) = \frac{qkx^2}{2R_{qx}\left(z_{\text{gen}}\right)} + \frac{qky^2}{2R_{qy}\left(z_{\text{gen}}\right)}. \tag{4.25}$$

To determine the radius of curvature for each axis, we perform the Taylor expansion (Equation (4.12)) on the intensity for an aberrated driver and only consider short trajectories with $\alpha^s = 0$. For the x-direction, the radius of curvature takes the form

(the y-direction follows analogously):

$$\frac{1}{R_{qx}(z_{\text{gen}})} = \frac{1}{R_x(z_{\text{gen}})} + \frac{4\Gamma c}{q\omega w_x^2(z_{\text{gen}})}\,, \tag{4.26}$$

with Γ adjusted to incorporate the different width at generation position, waist and Rayleigh range between the two axes

$$\Gamma = \frac{\gamma^s\,(\Omega - \Omega_p)^2\, w_x\left(z_{\text{gen}}\right) w_y\left(z_{\text{gen}}\right)}{I_0 w_{0x} w_{0y}}\,. \tag{4.27}$$

Using this mathematical description for the harmonic radius of curvature and the beam width at the generation position (derived from the power law in Section 4.2.2) we can simulate the evolution of harmonic beams along the x- and y-direction. Figure 4.7 shows this evolution of two harmonic orders in x- and y-direction, together with their spatial profile in the far-field. The parameters of the fundamental field are the same as in Figure 4.6.

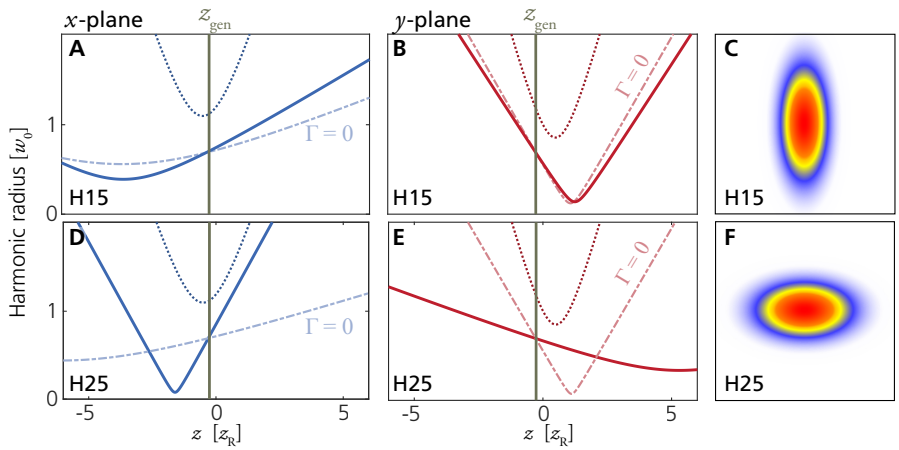

Figure 4.7: Harmonic beam evolution and spatial profile. Beam radius along propagation direction in x- and y-direction for the 15th harmonic **(A-B)** and 25th harmonic order **(D-E)**, together with their simulated far-field profile **(C)** and **(F)**. The solid lines represent the harmonic evolution taking into account the phase transfer of the fundamental, together with the dipole phase derived from the γ-model. The dashed line represents harmonic propagation without the dipole phase contribution ($\Gamma = 0$). The thin, dotted line represents the beam width of the driving laser. The generation position is indicated by the vertical dark green line.

Due to the astigmatism of the driver, the harmonics exhibit distinct divergence characteristics along the x- and y-directions. These characteristics depend on both the generation position and the harmonic order. For the generation position shown in the Figure, the beam of the 15th harmonic diverges more strongly along the y-direction than the x-direction, whereas for the 25th harmonic, this trend is reversed. To reconstruct the far-field image, a numerical calculation of the diffraction integral for each

individual harmonic can be performed

$$I_{XUV}\left(\theta_x, \theta_y, q\right) = \left| \iint \sqrt{I_q\left(x, y, z_{\text{gen}}\right)} e^{-i\phi_q(x,y,z_{\text{gen}})} e^{iqkx\theta_x} e^{iqky\theta_y} dxdy \right|^2, \tag{4.28}$$

that results in the profiles plotted in Figure 4.7 (C and F).

When considering the case where the harmonic phase is purely composed of the phase transfer of the fundamental beam ($\Gamma = 0$, dashed lines), there are only marginal differences between the harmonic orders. This suggests that the harmonic dipole phase plays a significant role in the strong order-dependent variations observed in both the spatial evolution and spatial profile of the harmonics.

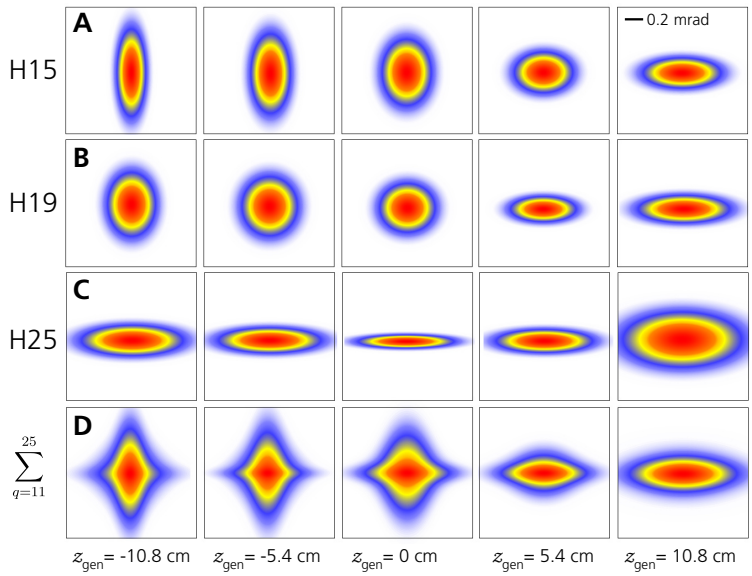

Figure 4.8: Simulation of the harmonic spatial profile. (A-C) Simulated spatial profiles for the 15th, 19th and 25th harmonic orders at five different generation positions. **(D)** Spectrally weighted sum of the harmonics, showing distinct cross-like patterns due to the opposing orientations of the harmonic order contributions.

To visualize these effects, Figure 4.8 presents simulated spatial profiles at various generation positions, illustrating how the harmonic beam shape evolves. The upper three rows show the spatial profiles for the 15th (A), 19th (B) and 25th (C) harmonic orders at five different generation positions. Subfigure D shows the effective harmonic spatial profiles, summed according to the experimentally determined spectral weights for the harmonic orders 11 through 25. This summed image reflects experimental observations, where, as in most HHG experiments, different harmonics typically cannot be resolved individually.

Lower-order harmonics transition from vertical to horizontal elongation as the generation position increases, while the 25th harmonic remains horizontally aligned across all generation positions. At negative generation positions and at the zero point, individual harmonics exhibit elongation along either the vertical or horizontal axis, depending on their order. The weighted superposition of differently oriented harmonics results in a structured spatial profile. For positive generation positions, the harmonic contributions become increasingly aligned along the same vertical axis. Consequently, the summed profile reflects this alignment with a more uniform spatial structure.

4.4.3 Validation of Aberration Effects on Harmonic Beams

The Intense XUV Beamline allows for a controlled study of the impact of beam astigmatism. This is made possible by two key components: the deformable mirror (introduced in Subsection 3.2.1), which enables wavefront control, and the XUV-CCD camera (presented in Section 3.2.4), which captures the harmonic spatial profile. To investigate the effects of an astigmatic driver, measurements were performed in the second half of 2022, using the now decommissioned CPA laser system. The results obtained contributed the experimental results in **Paper I**.

The deformable mirror was used to adjust the focal position of the driving laser relative to the generation medium, effectively shifting the generation position. The IR beam profile at the height of the gas target was simultaneously recorded using the leak from a dielectric mirror. This setup enabled a systematic scan across different generation positions, with concurrent measurements of both the IR near-field and the XUV far-field spatial profile.

By adding a metallic filter (200 nm tin) in addition to the 200 nm aluminium filter that is principally in the beam path to separate the IR from the XUV, the harmonic spectral profile was reduced to the single harmonic order 15.

Figure 4.9 presents the evolution of the driving laser and the experimentally determined XUV spatial profiles alongside simulations. Panel A shows the evolution of the IR driver with a strong separation of the harmonic foci in the x and y-direction, indicating a pronounced amount of astigmatism in the driving laser.

Panel B shows the experimentally determined harmonic spatial profile as the effective sum over all harmonic orders in the spectrum. At negative generation positions, the beam exhibits complex patterns forming a cross-like structure, whereas at positive generation positions, the profile transitions to a horizontally elongated shape. These experimental observations align well with the simulated profiles in Panel D, which were obtained using the experimentally determined parameters of the driving laser.

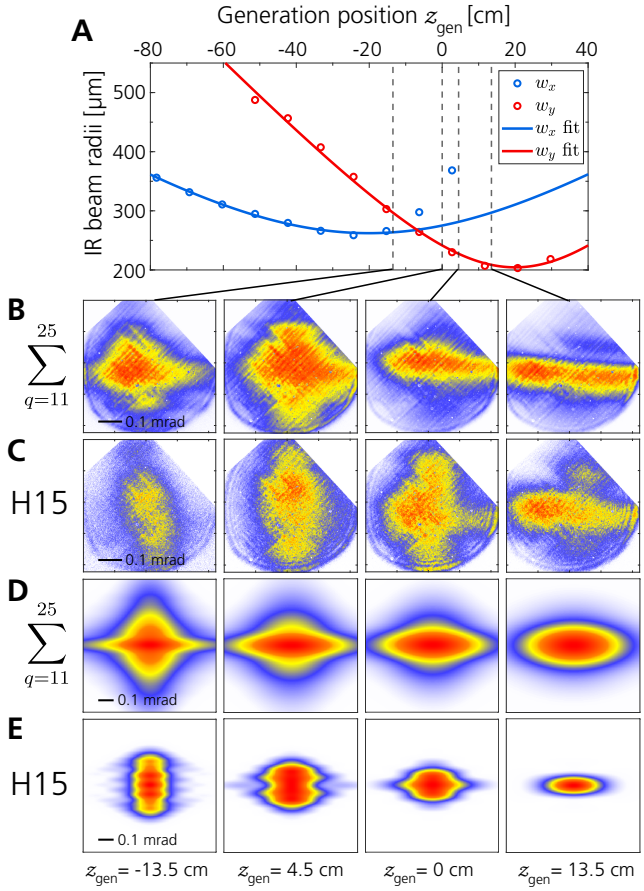

Figure 4.9: Characterization of IR driver and XUV with an aberrated profile. **(A)** Beam radii of the driving laser along the generation position in the x-direction (blue) and y-direction (red). **(B)** and **(D)** Experimentally measured XUV far-field spatial profiles for the sum of harmonics, and the isolated 15th order respectively at four selected generation positions. **(C)** and **(E)** Simulated XUV far-field for the sum of harmonics and the single 15th order, based on the parameters of the experiment. The simulations consider higher-order contributions in the Taylor expansion of the intensity of the driving laser.

The tin-filtered XUV far-field for harmonic order 15 is shown in Panel C. Unlike the previous simulations (Figure 4.8), the single harmonic exhibits complex spatial structures at $z_{\text{gen}} = 4.5\,\text{cm}$. This discrepancy arises because the previous simulations only included second-order terms in the Taylor expansion (Equation 4.12) of the driving laser intensity. While this approximation is valid for describing the overall harmonic spatial profile—where overlapping harmonic orders with different orientations dominate the pattern—it appears insufficient for capturing the spatial structure of an individual harmonic. This approach produces a more complex simulated spatial profile (Fig. 4.9, Panel E), which reproduces the complex experimental features of the experimental measurement in Panel B. The resulting simulated spatial profile (Figure 4.9,

Panel E) captures the intricate experimental features observed in **Panel C**, demonstrating that higher-order terms play a role in shaping individual harmonic profiles.

As the deformable mirror allows not only for adjusting the focus to optimize generation conditions, it also enables correction of wavefront aberrations in the driving laser by applying a custom voltage map to the 31 surface actuators. By fine-tuning the wavefront, we demonstrate in **Paper I, Figure 8**, that the IR astigmatism can be corrected, producing a cylindrically symmetric beam. As a result, the spatial profile of the harmonics is free of aberrations. This demonstrates that correcting the beam yields a well-defined, round spot in the XUV far-field.

4.5 Flat-top driving laser

Correcting wavefront aberrations in the driving laser can lead to more uniform spatial profiles in the harmonic far-field with better focusability, but the fundamental beam shape itself also plays a crucial role in determining the spatial coherence and focal properties of the generated harmonics. In particular, the strong intensity gradients inherent to the transverse profile of Gaussian beams introduce variations in the harmonic dipole phase, leading to order-dependent harmonic curvatures. To mitigate these effects and achieve more uniform harmonic beam characteristics, an alternative approach is to employ a flat-top driving laser.

A flat-top beam is characterized by a more uniform intensity distribution with significantly reduced intensity gradients. This section explores the advantages of using a flat-top driver for HHG, particularly its impact on reducing harmonic longitudinal focus spread, improving intensity uniformity, and enhancing beam characteristics compared to a Gaussian driver. The following experiments were conducted in late 2019 and are detailed in **Paper II**. They were performed using the now-decommissioned CPA laser system, which originally had a Gaussian transverse intensity profile.

To create a flat-top profile, a phase mask is introduced into the beam path, imposing a π-phase shift on the inner disk covering about half of the beam diameter. The beam's intensity is shaped by the superposition of the inner disk and the phase-shifted outer region. These two contributions interfere destructively, effectively modifying the transverse profile. An iris aperture is used to adjust the intensity ratio between the phase-shifted center and the beam edges, allowing gradual control over the profile shape. Figure 4.10 A schematically illustrates the transverse beam profile for different iris openings, with the phase step indicated by a dashed ring.

Figure 4.10 B shows measured intensity profiles along the radial coordinate for six different iris diameters. The top curve corresponds to the case where the iris is as wide

as the phase mask, resulting in the transverse profile of a Gaussian beam. As the iris opens further (moving toward the bottom curves), more phase-shifted contributions from the edges overlap with the central part, progressively shaping the beam from a Gaussian to a super-Gaussian or flat-top profile.

The phase mask is mounted on a linear actuator, enabling it to be moved in and out of the beam path, allowing for switching between flat-top and Gaussian profiles under identical experimental conditions. High-order harmonics are generated using either a gas jet or a 1 cm-long pulsed gas cell, with the resulting harmonics imaged via a grating spectrometer for full-width at half-maximum (FWHM) reconstruction along the non-diffracted axis.

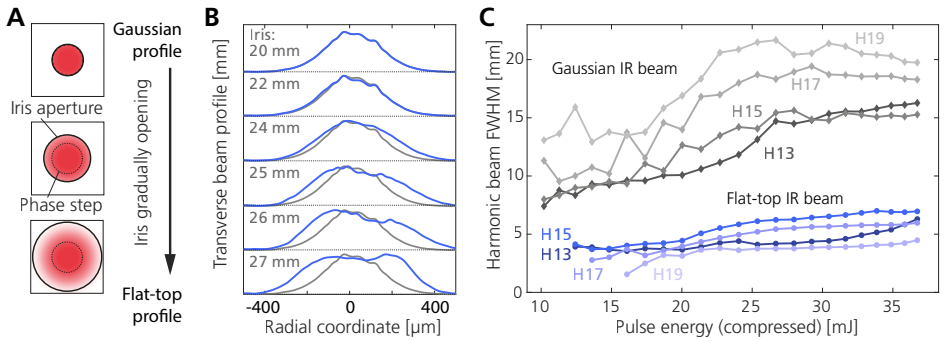

Figure 4.10: Gaussian and flat-top driver profile. (A) As the iris opens, more phase-shifted contributions from the edges interfere with the central part of the beam, effectively shaping the transverse profile. **(B)** Transverse intensity profiles for the initial Gaussian beam, gradually modified by increasing the iris diameter, allowing greater phase-shifted contributions to interfere with the inner part of the beam. **(C)** Harmonics FWHM as a function of pulse energy. Harmonics generated with a Gaussian driver (grayscale) exhibit strong variations across harmonic orders as pulse energy increases, whereas those generated with the flat-top beam (blue) exhibit a weaker dependence on pulse energy. Panel B and C modified from Paper II.

Figure 4.10 C presents the FWHM of harmonics generated with Gaussian and flat-top driving lasers as a function of the driving laser pulse energy. Harmonics generated with the Gaussian beam exhibit significant variations in beam width as pulse energy changes, with each harmonic order responding differently. In contrast, harmonics generated with the flat-top beam display a much weaker dependence on pulse energy, featuring a smaller beam width and more consistent trends across all harmonic orders.

To analyze the focusing properties of individual harmonics, a slit was placed at a fixed distance from the spectrometer screen. By transversely scanning the slit through the beam, the resulting diffraction pattern was recorded. This technique, known as the Spectral Wavefront Optical Reconstruction by Diffraction (SWORD) method, enables the reconstruction of the harmonic radius of curvature, and subsequently waist size, and focal position.

Figure 4.11 A and B compare the beam waist and focus position for harmonic orders 11

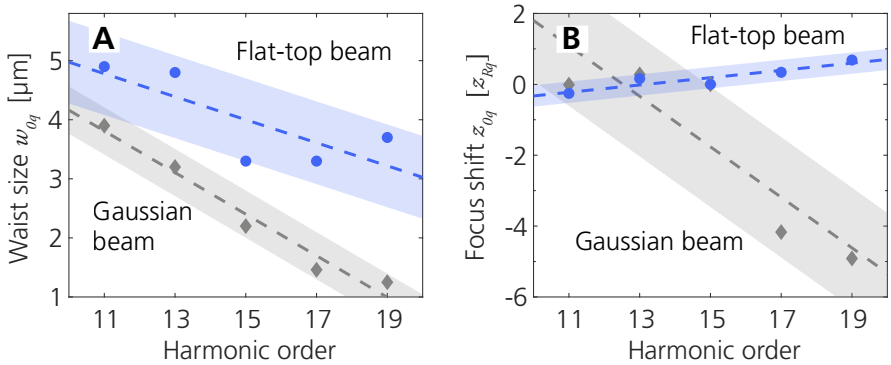

Figure 4.11: Harmonic beam waist size and focus shift for a Gaussian and a flat-top driving laser. (A) and **(B)** Waist size and focus shift determined via the SWORD measurements for Gaussian (gray) and flat-top (blue) drivers. The flat-top beam shows reduced variation across harmonic orders. Figure reproduced from Paper II.

to 19 generated with a Gaussian and a flat-top driver. The flat-top beam generally produces slightly larger harmonic beam waists but with a more consistent focus position across harmonic orders. In contrast, the Gaussian beam exhibits strong chromatic aberrations, shifting the longitudinal focal positions by up to five Rayleigh ranges.

This behavior can be explained by the harmonic dipole phase, which is defined via both the driver's intensity distribution and the harmonic order q. In a uniform-intensity flat-top beam, intensity gradients are reduced, leading to weaker phase variations and a more consistent radius of curvature across harmonic orders. As a result, harmonics generated with the flat-top driver exhibit less variation in waist size and a narrower focus shift compared to those generated with a Gaussian beam. This improved spatial coherence leads to a more confined harmonic focal distribution along the propagation axis, in turn allowing for more effective harmonic refocusing and potentially higher intensities.

Simulations based on the waist size and focus shift shown in Figure 4.11, presented in **Paper II** further underscore that the flat-top driver can mitigate chromatic aberrations by enabling harmonics to focus with a smaller separation between different orders.

4.6 Out-of-focus generation

The introduction of the new OPCPA laser system inherently presents the challenge of managing the significantly increased peak intensity compared to the previous system. If the focusing geometry remains unchanged, the much shorter pulse duration—almost four times shorter than before—and the larger beam width lead to a substantial

rise in the peak intensity.

HHG has a minimum intensity I_{mic} defined by the single atom response (hence referred to as microscopic) and can be derived by setting the cutoff Equation (2.5) equal to the energy of the harmonic order q:

$$I_{\mathrm{mic}} = \frac{m_e \omega^2}{3.17 \times 2\pi\alpha} \left(q\omega - \frac{I_{\mathrm{p}}}{\hbar} \right). \tag{4.29}$$

This defines the lowest intensity at which the returning electron can reach the required cutoff energy. However, this does not imply efficient harmonic generation since higher intensities are required to ensure a sufficient tunneling rate for HHG.

There is also an upper intensity limit I_{mac}, imposed by the macroscopic response: once the ionization degree reaches a critical level, the wavevector mismatch induced by plasma Δk_{fe} can no longer be compensated by gas dispersion and phase matching degrades.

For the 23rd harmonic in argon this opens an intensity window between $I_{\mathrm{mic}} = 1.0 \times 10^{14}\mathrm{W/cm^2}$ and $I_{\mathrm{mac}} \approx 2.1 \times 10^{14}\mathrm{W/cm^2}$ [137].

Using the OPCPA laser parameters and assuming a Gaussian intensity profile with a pulse energy of $E = 25\,\mathrm{mJ}$ (accounting for a 50 % reduction from iris truncation), a pulse duration of $\tau = 9\,\mathrm{fs}$ and the beam waist of $w_0 \approx 200\,\mu\mathrm{m}$ (consistent with Subsection 3.2.2), the peak intensity is

$$I_0 = \frac{2E}{\pi w_0^2 \tau} = 4.4 \times 10^{15}\mathrm{W/cm^2}, \tag{4.30}$$

which exceeds the I_{mac} by far, effectively limiting the conversion efficiency.

The peak intensity can, in principle, be reduced by adapting the focusing geometry, such as extending the focal length or reducing the beam diameter before focusing. However, these changes also result in a larger beam waist and, consequently, a broader width of the harmonics, degrading the ability to focus them tightly. To address this issue, we discuss out-of-focus generation, where the generation medium is positioned away from the high-intensity focus of the driving laser. Figure 4.12 A schematically illustrates this principle. Subfigure B shows the peak intensity of the beam along the propagation axis for a Gaussian beam, with the red shading indicating regions of excessively high intensity.

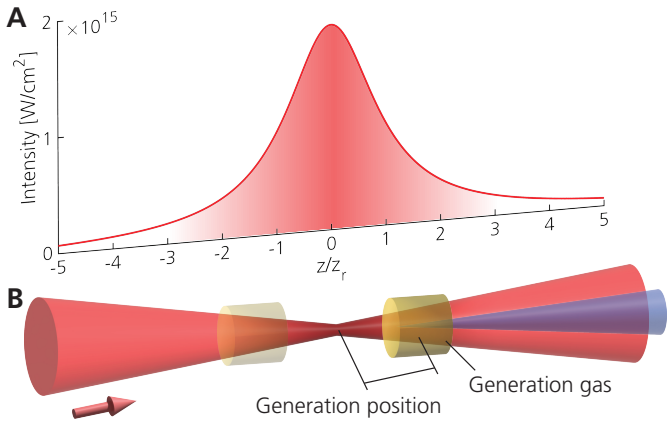

Figure 4.12: Principle of out-of-focus generation. **(A)** Intensity along the propagation direction, following a Lorentzian trend characteristic of a Gaussian beam. The region where the intensity is too high for efficient HHG is shaded with a red color gradient. **(B)** Schematics of out-of-focus generation, where the generation medium is located away from the focal point of the driving laser.

To examine how generating away from the driving laser focus affects the harmonic beam waist and focus position, the on-axis intensity is adjusted to remain constant across different generation positions. To maintain a constant intensity at the generation medium I_{gen}, the peak intensity in focus I_0, is adjusted following the expressions of a Gaussian beam

$$I_0 = I_{\text{gen}}(1 + (z_{\text{gen}}/z_{\text{R}})^2). \tag{4.31}$$

With this adjusted intensity, we perform simulations of the harmonics focus position and waist, using the γ-model to determine the harmonic dipole phase. The results are presented in Figure 4.13.

Panels A and B show the harmonic focus position and beam waist as a function of the generation position, assuming a Gaussian driver beam with peak intensity at the focus that decreases away from it. These simulations extend the results from Figure 4.3, covering a wider range of generation positions. The transition to dashed lines indicates where the intensity at the generation position drops below the cutoff intensity I_{mic} for individual harmonics.

As discussed in Section 4.2.3, the focus position and beam waist vary significantly between harmonic orders when generated before the driving laser focus. Beyond the focus ($z_{\text{gen}} > 0$), this variation is greatly reduced, the harmonic focus positions span a much narrower range and the harmonic beam waists are smaller. Nevertheless, practical gains from generating harmonics in this region are limited because the intensity quickly falls below I_{mic} for some harmonic orders.

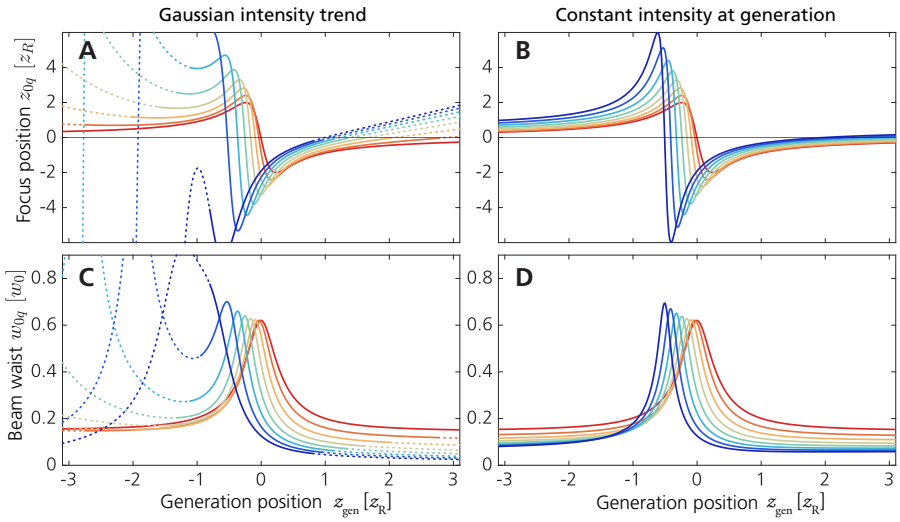

Figure 4.13: Harmonic focus position and beam waist simulations with different intensity profiles. (A) and **(C)** show the focus position and beam waist for harmonics generated by a driver with a Gaussian intensity profile with the peak intensity I_0 = 2×10^{14} W/cm^2 at the focus. The curves become dashed when the intensity $I(z_{gen})$ drops below the harmonic order dependent minimum intensity I_{mic}. **(B)** and **(D)** show the focus position and beam waist for a constant intensity of $I(z_{gen})$ = 2×10^{14} W/cm^2 for all generation positions. Harmonic orders are color-coded from harmonic 11 (red) to 25 (blue).

Panel A also shows that all harmonics generated after the focus have a virtual focus. Although the plot appears to show positive focus positions, these occur only after the intensity has dropped below I_{mic}, where the gamma model no longer applies. Since the short-trajectory dipole phase always contributes a diverging component, it cannot convert a virtual source into a real one. This means that the apparent shift to a positive focus position is merely an artifact of insufficient laser intensity.

Panels B and D show focus position and beam waist when the intensity in the focus is adjusted to be constant at the generation position, following Equation 4.31. Within the Rayleigh range, the results closely resemble those obtained using a Gaussian intensity profile. However, for generation positions outside the Rayleigh range, the harmonics exhibit only a small spread in focus position, and show a small beam waist throughout all orders.

These effects arise because dipole phase scales inversely with the intensity $\Phi^s \propto 1/I_o$ for short trajectories. However, in this scenario, the intensity is increasing with the distance from the center. Consequently, the dipole phase contribution becomes small, and the harmonics evolution is dominated by the phase transfer from the driving laser, and diffraction.

There are two notable observations from these simulations:

1. The results show no strong preference for whether generating before or after the focus yields a smaller spread in focus position and beam waist. However, additional factors, particularly the macroscopic propagation behavior of the harmonics that dictates the phase-matching efficiency must be considered.

2. The harmonic beam waist is significantly smaller—by a factor of approximately three—when generating outside the Rayleigh range compared to generating at the focus. This has crucial implications for refocusing harmonics to high intensity. Since intensity scales as the inverse square of the waist, this reduction in beam waist size translates to a potential ninefold increase in peak intensity, without requiring higher laser power.

As the intensity in the generation medium is adjusted, there is no risk of it falling below the cutoff intensity I_{mic}. However, a practical constraint arises when the laser can no longer supply sufficient power to maintain the required intensity at the generation position. For the OPCPA laser system, this limiting position lies beyond the range of the figure, approximately 4.6 Rayleigh ranges away from the focus.

The feasibility of out-of-focus generation has been successfully demonstrated at other beamlines [138, 139]. This approach presents a viable alternative to major redesigns of beamline configurations, offering a practical route to optimizing HHG without extensive modifications on the setup. However, beam quality is essential, as a larger beam can undergo reshaping at the focus, leading to significant distortions beyond the Rayleigh range.

4.7 Phase-matching properties

Although the single-atom response is fundamental for high-order harmonic generation (HHG), efficient emission requires constructive interference of contributions from many atoms along the propagation direction. As discussed in Section 2.6, the wavevector mismatch is composed of four contributions, neutral gas dispersion Δk_{at}, plasma dispersion Δk_{fe}, the geometrical phase mismatch Δk_{foc} and the contribution from the dipole phase shift Δk_{dip}.

At a chosen focusing geometry and intensity (which defines both the Rayleigh range and a suitable intensity window for HHG), the two main parameters that remain for fine-tuning phase matching are the gas density and the medium length.

Adjusting the gas density, which is proportional to the pressure in the experiment, affects both the neutral gas dispersion and the plasma dispersion. The plasma dispersion can be approximated to scale with the gas density $\Delta k_{\mathrm{fe}} \rightarrow \Delta k_{\mathrm{fe}}/(\rho\eta_{\mathrm{fe}})$, with

η_{fe} being the ionization degree of the gas. The neutral gas dispersion scales similarly, with $\Delta k_{\mathrm{at}} \rightarrow \Delta k_{\mathrm{at}}/(\rho)$.

The medium length affects how far harmonics can build up coherently. A longer medium can increase the total generated signal if phase matching holds, but it also risks higher ionization (leading to phase mismatch) and reabsorption of the produced XUV radiation. The Gouy-phase accumulation likewise becomes more significant over longer distances near the focus, leading to an increased mismatch term.

The key is to optimize the phase-matching condition to achieve $\Delta k \approx 0$ by balancing the two parameters, pressure and medium length. Numerical calculations based on solving the propagation equation for the driving laser and the harmonic field, presented in [140] and [36] are performed to map out the variable space of pressure, medium length and the resulting conversion efficiency. Figure 4.14 A-C showcases the simulated conversion efficiency for the 23rd harmonic generated in argon at different intensities.

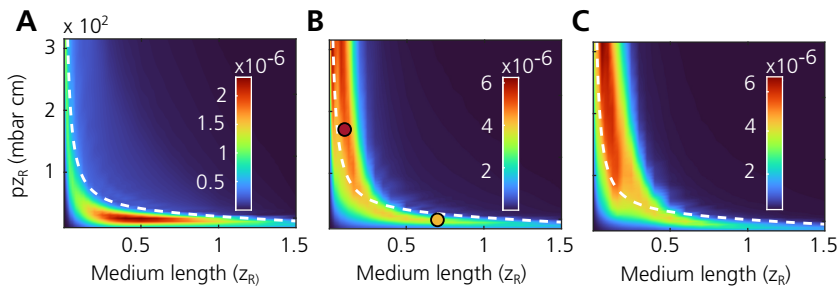

Figure 4.14: The two phase-matching regimes in argon. Simulated conversion efficiency of the 23rd harmonic in argon as a function of medium pressure and length for three laser intensities: 1.5×10^{14}W/cm^2 **(A)**, 2.5×10^{14}W/cm^2 **(B)**, and 4.5×10^{14}W/cm^2 **(C)**. In panel **B**, the two phase-matching regimes are highlighted: high-pressure (red) and low-pressure (yellow). Modified from [41].

From the simulations it can be seen that the conversion efficiency follows a hyperbolic trend, which allows to identify two regions that show high conversion efficiency: A horizontal and a vertical branch.

- The horizontal branch operates in a low-pressure regime with a long gas medium, favoring lower laser intensities and a low ionization degree. Here, free electron contribution is negligible ($\Delta k_{\mathrm{fe}} \approx 0$), and phase matching is achieved when neutral atom dispersion cancels the Gouy phase and dipole phase contribution. Due to the weak absorption at low pressure, a long interaction length is required to optimize conversion efficiency. Since only the neutral dispersion scales with pressure, phase matching becomes highly pressure-dependent and is effectively achieved by balancing the three contributions $\Delta k_{\mathrm{at}} + \Delta k_{\mathrm{foc}} + \Delta k_{\mathrm{i}} = 0$.

- The vertical branch occurs in a high-pressure regime with a short gas medium and requires sufficiently high laser intensity, such that plasma-induced phase mismatch compensates for neutral atom dispersion. Here, the dipole-induced phase mismatch is relatively small, and due to the short medium length, the geometrical phase mismatch is negligible. Because both neutral atom and plasma dispersion scale with pressure, phase matching is less pressure-sensitive than in the horizontal branch. Hence, phase matching is effectively achieved by balancing the strong gas dispersion with the plasma induced phase mismatch $\Delta k_{\mathrm{at}} + \Delta k_{\mathrm{fe}} \approx 0$.

The hyperbolic trend describing the transition between both branches is described following [36]:

$$(p - p_0)\, L = \frac{\varsigma k_B T f_i(z)}{\sigma_{\mathrm{abs}}}, \tag{4.32}$$

where p is the medium pressure, p_0 the minimum phase-matching pressure when there is no ionization of the medium, L the medium length, ς a constant that is defined via the coherence and absorption length of the medium, k_{B} and T the Boltzmann constant and temperature. The factor $f_i(z)$ depends on the medium position, and corrects the phase-matching pressure relative to the pressure at laser focus, and σ_{abs} is the absorption cross-section.

The hyperbolic behavior of the conversion efficiency has been experimentaly confirmed in **Paper IV**. By performing measurements at both the Intense XUV Beamline and the SYLOS GHHG LONG beamline at ELI-ALPS, the universal applicability of the model, independent of the geometry of the beamline has been confirmed.

Chapter 5

Attosecond Pulses: Techniques and Applications

Attosecond pulses enable ultrafast studies of electronic dynamics in atoms, molecules, and solids. This chapter discusses the characterization methods and applications of these pulses in advanced experimental schemes. First, the procedure for achieving temporal and spatial overlap of laser beams using Above Threshold Ionization (ATI) scans as a type of high-order autocorrelation is described. Next, the velocity map imaging (VMI) principle and the algorithmic steps required for inverting raw images to retrieve angle- and energy-resolved electron distributions are detailed. The chapter then introduces the RABBIT technique, which is, in a first step, used to characterize the temporal structure of attosecond pulses. Subsequently, the focus shifts to angle-resolved measurements of photoelectron distributions in RABBIT scans, highlighting neon as a case study, central to the findings in **Paper V**, and presenting so far unpublished results that have not yet been fully analyzed. Finally, nonlinear XUV–XUV pump-probe methods are explored, concentrating on double-ionization in neon. Comparisons of direct and sequential ionization channels, their cross sections, and the experimental considerations for reaching sufficiently high XUV intensities are presented.

5.1 Finding temporal and spatial overlap

Above Threshold Ionization (ATI), first described in 1979 [141, 142], specifies the absorption of more photons than is required to ionize an atomic electron. ATI is a nonlinear process that, given sufficient laser intensity, results in the ejection of electrons with excess kinetic energy, arranged in levels with a $\Delta E = \hbar\omega$ spacing, correspond-

ing to the energy of a single photon. Direct ATI emission has an upper limit at $2U_p$. However, at higher intensities, an additional emission plateau extends up to $10U_p$. This plateau can be explained within the three-step model, in which electrons driven back by the oscillating laser field do not immediately recombine but instead undergo rescattering with the atomic core [143–145].

In a velocity map image, the photoelectrons appear as a series of concentric rings, each ring corresponding to an additional $\hbar\omega$ of energy. The angular distribution along these rings depends strongly on the laser polarization and exhibits symmetry around the polarization axis. Moreover, the angular distribution often features off-axis contributions and complex structures that depend on ionization dynamics, such as rescattering of electrons by the ion [146, 147], quantum path interferences [148] or Coulomb interaction [149, 150]. Figure 5.1 A shows an angle-resolved electron velocity map image using neon as a target gas. The laser polarization is vertical, lying within the plane parallel to the detector.

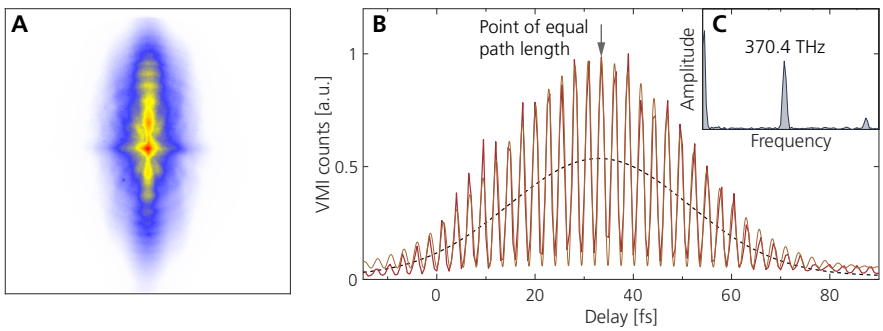

Figure 5.1: Above-threshold ionization of neon. (A) Angle-resolved raw VMI of neon, averaged over ∼4000 laser shots. **(B)** ATI photoelectron yield (red) of neon as a function of IR delay in increments of 0.5 fs. By performing a qualitative fit (orange) using a Gaussian function with cosine modulation, the envelope FWHM is τ_{FWHM} = 43 fs, assuming a Gaussian temporal profile. The envelope's maximum (black dashed) corresponds to the point of equal pathlength. **(C)** The Fourier analysis reveals a f = 370.4 THz oscillation, corresponding to a fundamental wavelength of λ = 810 nm.

The laser usually used to generate HHG also provides sufficient intensity to induce ATI. By performing IR-pump IR-probe scans, the ATI signal serves as a high-order autocorrelation method, making it a valuable tool for characterizing laser parameters and benchmarking both the IR delay stage and the split-and-delay unit [114, 117]. The ATI signal is measured by monitoring the electron or ion yield while adjusting the delay between both IR pulses. As the two IR pulses interfere, the ω oscillations become apparent in the signal. The closer the interferometer path lengths, the stronger the ATI yield, with the signal's envelope providing information about the pulse's temporal profile. The ATI signal peaks when the optical path lengths of the two arms are equal. Accordingly, the ATI scan is used to align the interferometer for XUV–IR

pump-probe experiments and to assess the temporal stability and resolution of the setup.

To enable IR-IR pump-probe measurements, filters are removed from the XUV arm of the interferometer to transmit IR. The IR intensity is tuned by attenuating the laser, or using apertures to ensure a single beam's intensity remains below the ATI threshold while their combined intensities produce a strong signal. The ATI yield is measured by recording either the electron velocity map image or the ion Time of Flight (ToF) signal while scanning the delay between the two IR pulses.

Figure 5.1 B shows the ATI autocorrelation trace at the Intense XUV Beamline using the CPA laser system and the IR delay stage in the interferometer chamber for scanning. The envelope has an FWHM of $\tau_{\mathrm{FWHM}} = 43\,\mathrm{fs}$. Treating ATI as a second order autocorrelation[1], the pulse duration can be determined via $\tau = \tau_{\mathrm{FWHM}}/\sqrt{2}$ to $\tau \approx 30\,\mathrm{fs}$. This is in accordance with autocorrelator measurements of the laser indicating durations between $35\,\mathrm{fs}$ and $40\,\mathrm{fs}$. A Fourier analysis, presented in panel C of Figure 5.1, reveals a frequency of $f = 370.4\,\mathrm{THz}$, corresponding to a wavelength of $\lambda = 810\,\mathrm{nm}$, aligning well with the laser's specified central wavelength.

5.2 Velocity map image inversion

Upon interaction with a laser or XUV field and a target gas, charge carriers are ejected with varying kinetic energy and direction in three-dimensional space. Through electrostatic lensing, the Velocity Map Imaging Spectrometer (VMIS) accelerates the charge carriers onto the detector, imaging the perpendicular components of their momentum on the detector screen [121, 122, 151]. This compresses the 3D momentum space into a 2D projection, as illustrated in Figure 5.2 A. In these raw images, each region associated with a particular momentum includes overlapping contributions from other momentum components along the unmeasured third dimension.

The inverse Abel transformation reconstructs the true momentum distribution, resulting in a cross-sectional slice through the spherical distribution, under the assumption of cylindrical symmetry around the laser polarization axis. Several inversion algorithms exist that provide a similar output but differ in computational efficiency [152–155]. Figure 5.2 B compares the raw image (left half) and the inverted image (right half) of XUV interacting with an argon target, reconstructed using the inversion algorithm described in [152]. The concentric rings represent photoelectrons with different kinetic energies corresponding to the HHG spectrum.

[1]ATI is highly nonlinear, involving more than 10 photons to ionize argon. Hence, a second-order autocorrelation is only a rough approximation.

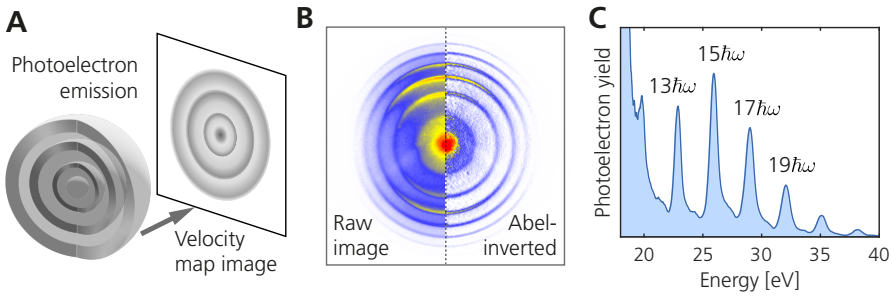

Figure 5.2: Principle of measurement and data retrieval. (A) Photoelectrons, ejected spherically with varying kinetic energy and direction, are accelerated toward the VMIS screen, where they are recorded as a two-dimensional projection. **(B)** Comparison of a raw image (left half) and its Abel-inverted counterpart (right half) for an interaction involving only XUV radiation with an argon target. **(C)** Calibrated angle-integrated photoelectron spectrum with the corresponding harmonic orders indicated.

To retrieve an energy resolved photoelectron spectrum, the Abel-inverted data is transformed from Cartesian to polar coordinates, and integrated along the emission angle. The calibration process involves correlating known harmonic energy values with their corresponding radial distances from the image center. The lowest energy peak corresponds to the first harmonic above the ionization potential of the target gas, determined by dividing the ionization potential of the target gas by the IR photon energy $I_p/\hbar\omega$. The energy-calibrated photoelectron spectrum for argon as a target gas is shown in Figure 5.2 C.

Several factors must be taken into account to perform Abel inversions. First, the repeller and extractor voltages of the VMIS must be tuned to ensure that all photoelectrons reach the detector. Electrons that fall outside the detector range result in incomplete data and erroneous reconstructions. Second, a sufficiently high number of recorded events and a high Signal-to-Noise Ratio (SNR) are required, as statistical noise can introduce artifacts into the reconstructed image.

Besides the two-fold symmetry of the velocity map images due to the laser polarization axis, targets with a symmetric structure can also exhibit spherical symmetry, resulting in a second symmetry axis. This holds as long as there are no external fields or misalignments that can break the symmetry.

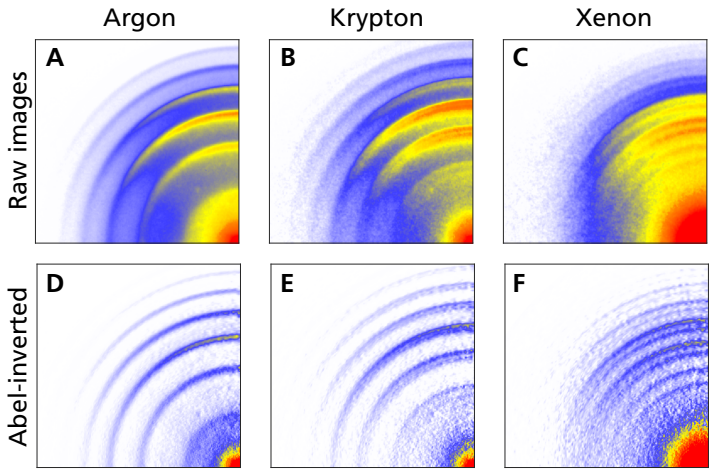

Figure 5.3: VMI for selected noble gases interacting with XUV. (A-C) Raw VMI with argon, krypton and xenon as target gas, together with their Abel-inverted images **(D-F)**. The full VMI has been folded into one quadrant due to the four-fold symmetry of the process. The increase in spin-orbit splitting with larger atomic number Z is clearly visible.

Neutral atoms can exhibit spherical symmetry, as their electron distribution forms an electron cloud with an up-down symmetry. In such cases, the velocity map images display a four-fold symmetry, allowing them to be folded into one quadrant, effectively improving the statistical signal-to-noise ratio by a factor of two. Figure 5.3 shows the raw VMI of three noble gases: argon, krypton, and xenon alongside their inversions, reduced to one quadrant.

Table 5.1: Spin-orbit splitting of selected noble gases The splitting describes the energy difference between the spin-orbit-coupled sub-levels of the ion p^5 state, and increases with atomic number Z.

Element	$\Delta E_{\text{spin-orbit}}$ [156]
Neon (Ne)	0.10 eV
Argon (Ar)	0.18 eV
Krypton (Kr)	0.67 eV
Xenon (Xe)	1.31 eV

Notably, the krypton images show a double-ring structure originating from spin-orbit splitting. Spin-orbit splitting increases with atomic number Z, as shown in Table 5.1. For argon, the splitting is too small to be resolved with the measurement resolution, while for xenon, the splitting energy is relatively close to the photon energy of the driving laser, that is $1.53\,\text{eV}$ for $810\,\text{nm}$. Since the images all feature direct ionization by the XUV only, the photoelectron distribution follows the laser polarization, with the off-axis contributions corresponding to the angular distribution of the ionization channels.

5.3 RABBIT

The Reconstruction of Attosecond Beating by Interference of Two-Photon Transitions (RABBIT) technique is a method to determine the temporal structure of attosecond pulses. First demonstrated by Paul et al. in 2001 [15], it represents the first experimental observation of attosecond pulse trains and constitutes a milestone in the field of ultrafast science. The interaction of both XUV and infrared radiation with a target gas leads to the appearance of intermediate peaks between the harmonics in the photoelectron spectrum, which are referred to as sidebands. These sidebands originate from two distinct quantum pathways:

$$E^+ = q\hbar\omega + \hbar\omega \qquad \text{and} \qquad E^- = (q+2)\hbar\omega - \hbar\omega, \tag{5.1}$$

where E^+ corresponds to the absorption of an additional IR photon by the photoelectron ionized by the q^{th} harmonic, and E^- corresponds to the emission of an IR photon by the photoelectron ionized by the $(q+2)^{\text{th}}$ harmonic. Figure 5.4 A schematically illustrates this principle while Panel B represents the photoelectron spectrum for krypton with XUV-only in contrast to XUV+IR, where the sidebands are clearly visible.

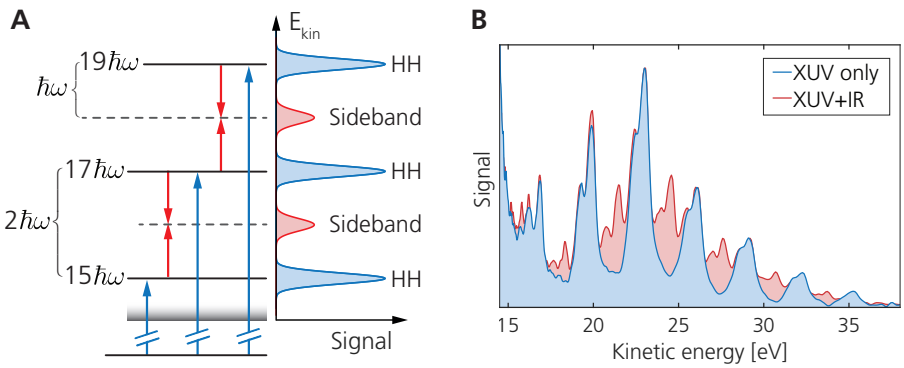

Figure 5.4: Schematics of a XUV–IR sideband generation. (A) An electron is excited into the continuum by an XUV photon. An additional IR photon can either be absorbed, increasing the electron's energy, or emitted, decreasing the electron's energy by an amount equivalent to the IR photon's energy. **(B)** Photoelectron kinetic energy spectrum for XUV-only excitation (blue) and XUV+IR interaction (red) of krypton. The presence of the IR field results in sidebands appearing between the harmonic peaks. The double peak structure in both harmonics and sidebands is due to the spin-orbit split.

When the delay between the XUV pulse and the IR field is varied, interference between the two quantum pathways modulates the sideband amplitude. Following [15, 157], this modulation can be expressed as:

$$S(\tau) = \alpha + \beta \cos\left[2\omega\tau - 2\omega\tau_1 - \Delta\Phi_{2q}\right] \ , \tag{5.2}$$

where α and β are constants, τ_I is the atomic emission delay which accounts for the time an electron requires to escape the atomic potential, and $\Delta\Phi_{2q}$ is the phase difference between the two consecutive high-order harmonics of orders q and $q+2$ that contribute to the sideband. The atomic emission delay τ_I is relatively small and can sometimes be derived from theory [15, 158], though effors have been made to determine the times experimentally [157].

By scanning the delay τ between the XUV and IR pulses, the oscillations in sideband amplitudes can be recorded. The aim of a RABBIT measurement is to derive the temporal pulse profile by extracting the phase differences between the harmonic orders from the sideband oscillations.

5.3.1 Scan analysis

The XUV–IR scan is performed by recording angle-resolved VMIS images while scanning the delay of the IR pulse relative to the XUV pulse. Each delay step corresponds to a single image, capturing several (e.g., 100–200) laser shots per step. Scans with higher numbers of shots per step or extended ranges (>20 fs) introduce specific challenges to measurement stability. Over longer timescales, fluctuations in laser intensity, harmonic yield, and beam pointing, along with drift in the spatial overlap between the XUV and IR beam in the interaction region, degrade measurement stability. These instabilities often lead to scans where the contrast of the sideband structures diminishes over parts of the range, making comprehensive analysis more difficult. To improve the signal-to-noise ratio (SNR) for the inversion procedure (discussed in Section 5.2), a data-binning approach is introduced.

This binning method initially considers only the angle-integrated VMIS data. Figure 5.5 A (lower panel) shows the non-inverted scan, where the signal is plotted as a function of distance from the center of the image and delay. To enhance image contrast, the data is normalized line-by-line along the distance axis, followed by subtraction of the average signal.

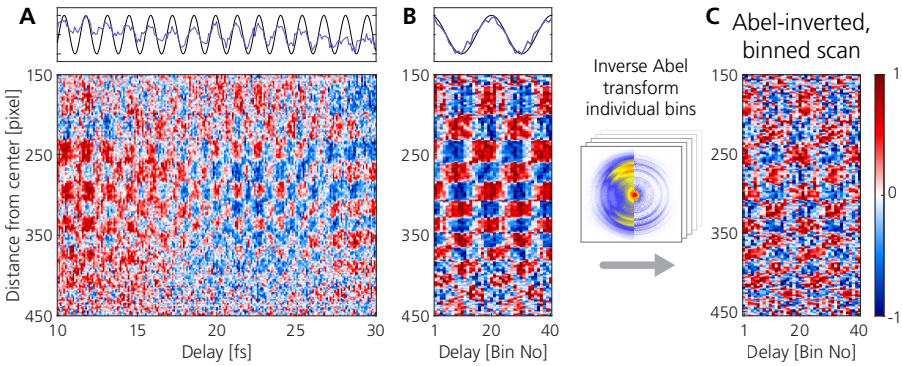

Figure 5.5: Illustration of the binning procedure for a RABBIT scan. (A) Angularly integrated RABBIT scan in krypton with a line-by-line average subtraction. The scan duration is $20\,\mathrm{fs}$ with a resolution of $0.1\,\mathrm{fs}$, covering about 15 oscillations. The upper panel indicates an excerpt of a sideband (purple) together with its oscillation retrieved from Fourier analysis (black). **(B)** The data is binned to 20 bins and repeated once for better visibility. One period with a duration of T = 1.357 fs is equivalent to 20 bins. The upper panel indicates the oscillation of the sideband for the binned data. **(C)** The inverse Abel-transformed data, based on the binned images.

Typically for RABBIT, the sidebands follow a 2ω oscillation. The one-photon signal (XUV peaks) oscillates as well, but with a π phase shift relative to the sidebands, resulting from depletion due to photons transferred into the sideband.

The sideband oscillations are extracted by integrating across a pixel range that is manually assigned. This assignment is done by comparing the angle- and delay-integrated photoelectron spectrum from the RABBIT scan with its XUV-only photoelectron spectrum, as shown in Figure 5.4 B. The top panel of Figure 5.5 A illustrates the extraction of a sideband (purple line) and its corresponding oscillation signal (black line), obtained via Fourier analysis.

Based on the observed oscillations, each delay step in the scan is mapped to a phase within a single oscillation cycle. The cycle is then divided into a predefined number of bins, and images corresponding to each bin are summed. The number of bins reflects a trade-off between temporal resolution and statistical robustness. In the example shown in Figure 5.5 B, a long scan consisting of 200 images is condensed into a single cycle with 20 bins. For clarity, the data in the figure is repeated once.

On average, each bin contains 10 images, improving the statistics for the inversion procedure by the same factor. Additionally, since this method is sensitive to the phase information of the scan, multiple individual scans can be effectively combined within the bins, further enhancing the statistical quality. Figure 5.5 C shows the binned scan after inversion, with the data again repeated after bin 20 for visual clarity.

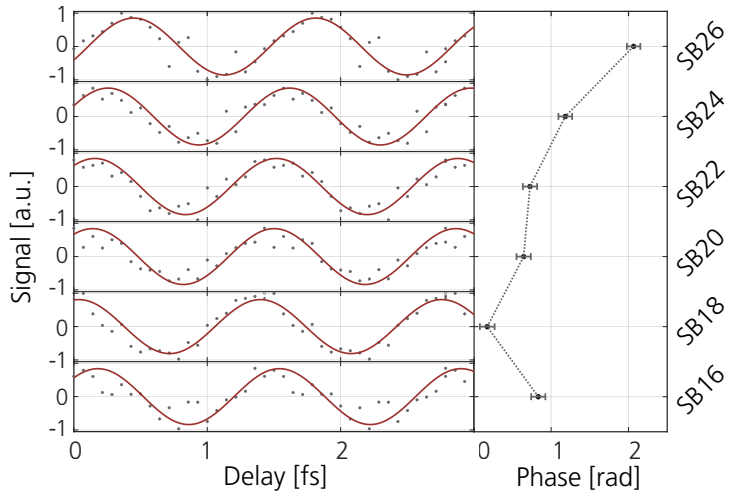

Figure 5.6: Sideband extraction from the extracted sidebands. The left panel shows the sideband signal (gray dots) obtained from the binned, inverted scan with a krypton target. By fitting a cosine function (red solid), the phase of the oscillation is determined, and plotted in the right panel. The error bars correspond to the confidence interval of the fit.

Figure 5.6 left panel shows the signal for sidebands 16 to 26, extracted from the binned and inverse Abel transformed scan (black dots) together with the cosine fit, following Equation (5.2). The right panel displays the extracted phases, with error bars representing the confidence intervals of the fit.

5.3.2 Pulse reconstruction

The attosecond pulse results from the interference of contributions from different harmonic orders. Its time-dependent intensity profile can be described as:

$$I(t) \approx \left| \sum_q \sqrt{I_q} \mathrm{e}^{-\mathrm{i}(q\omega t - \Phi_q)} \right|^2 , \tag{5.3}$$

where I_q represents the individual harmonic amplitudes measured with the spectrometer or retrieved from XUV-only velocity map images, and Φ_q being the harmonic phase.

A RABBIT scan cannot retrieve an absolute phase value, as the sideband phases only provide the phase differences between consecutive harmonics. However, adding a phase constant across all harmonics has no effect on the temporal shape of the pulse profile. Therefore, this constant phase term can be chosen arbitrarily or set to zero. Thus, the phase difference between consecutive harmonics is sufficient to fully describe the temporal profile.

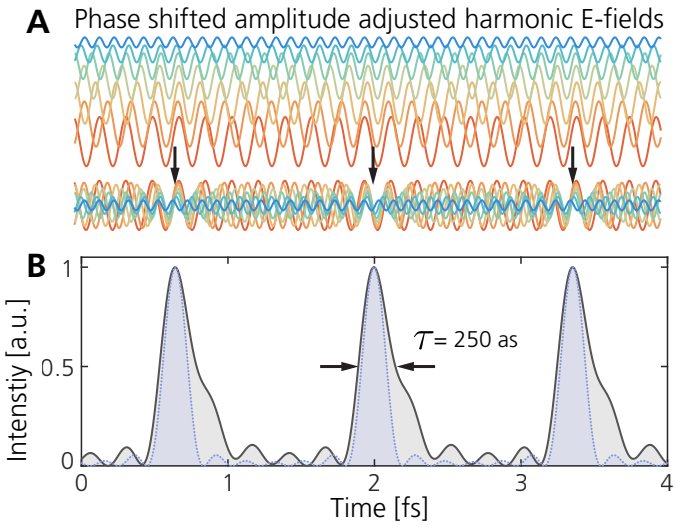

Figure 5.7: Temporal reconstruction of the attosecond pulses. (A) Contributing harmonic orders, with amplitudes and phases determined from the experiment. The harmonics are color-coded, ranging from orange (H15) to blue (H27). **(B)** Temporal reconstruction of the attosecond pulse, showing intensity profile over time (solid line, grey shaded). The pulse duration (FWHM) is determined to be 250 as. The dotted line (blue shaded) represents the Fourier transform limited pulse with a duration of 173 as.

Figure 5.7 A shows the individual harmonic oscillations, featuring the electric field amplitude $E(t) \propto \sqrt{I_q}$ and phase differences $\Delta\Phi$ as retrieved from the scan. The corresponding intensity profile, reconstructed using Equation (5.3) is plotted in Figure 5.7 B, revealing the temporal profile of the pulse (solid black line). The dashed line represents the Fourier-transform limited case ($\Phi_q = 0$).

For this pulse, the determined duration based on the FWM has a duration of 250 as. This compares to 173 as in the transform limited case. However, the contribution from the atomic emission delay τ_I, introduced in Equation (5.2) has been neglected in this reconstruction.

5.4 Angle-resolved RABBIT

So far we have determined the phase difference between different harmonic orders, ignoring the angle-resolved component of the photoelectron momentum distribution by simply integrating across the angle. However, the angular distribution of the photoelectron emission contains information on the ionization channel.

Neon has a $2p^6$ electron configuration in its ground state. Following dipole selection rules, photoionization allows for two continuum states: an ϵs state with angular mo-

mentum $\lambda = 0$, and an ϵd state with $\lambda = 2$. Each electron wave packet accumulates a specific phase during photoionization that is due to the atomic potential, including the short-range Coulomb interaction and the centrifugal potential.

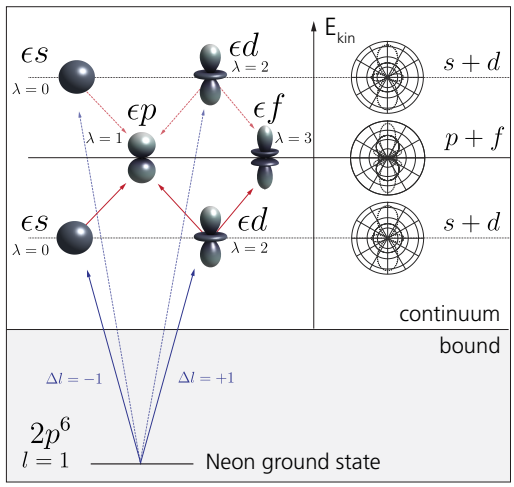

Figure 5.8: Angular channels for neon photoionization. Neon is ionized by the XUV photon (blue arrow) in either an ϵs or ϵd continuum state (for m = 0). The additional interaction with an IR photon (red arrow) allows additional pathways into ϵp and ϵf continuum states. The interference of the different channels (dashed lines) changes the PAD as a function of delay between XUV and IR. Modified from [159]

The ionization channels are further distinguished by the magnetic quantum number $m = 0, \pm 1$ in the ground state. For $m = 0$, there are two channels $2p \rightarrow \epsilon s$ $(\lambda = 0)$, and $2p \rightarrow \epsilon d$ $(\lambda = 2)$ whose contributions interfere coherently. For $m = \pm 1$ there is only a single channel $2p \rightarrow \epsilon d$ $(\lambda = 2)$, which contributes incoherently. As the channels interfere, the Photoelectron Angular Distribution (PAD) changes. Figure 5.8 indicates these ionization pathways with the blue arrows indicating the single-photon ionization pathways.

The one-photon angular distribution can be expressed as an expansion of Legendre polynomials [160, 161]

$$I_{\mathrm{HH}}(\theta) = h_0 + h_2 P_2(\cos\theta), \tag{5.4}$$

where h_0 and h_2 are coefficients of expansion that hold information on photoionization dynamics, and P_2 is the second-order Legendre polynomial.

This single-photon ionization process, however, only results in a static photoelectron intensity distribution, allowing the retrieval of direct phase information but lacking the amplitude of the individual angular momentum channels.

Analogous to the RABBIT technique, the interaction with an additional IR-photon introduces extra ionization pathways (Figure 5.8 , red arrows) that add complexity and create interferences, oscillating with the delay between the XUV and IR field. These delay-dependent interferences encode the amplitude information of the single-photon ionization process.

As the sidebands originate from a two-photon process, it follows a more complex description that also varies with the delay τ, following [161, 162]:

$$I_{\mathrm{SB}}(\theta,\tau) = h_0(\tau)P_0(\cos\theta) + h_2(\tau)P_2(\cos\theta) + h_4(\tau)P_4(\cos\theta) \tag{5.5}$$

with $h_i(\tau)$ being the delay-dependent coefficients. The Legendre polynomials for the first, second and fourth order are written out to

$$P_0(x) = 1, \qquad P_2(x) = \frac{3x^2-1}{2}, \qquad P_4(x) = \frac{35x^4-30x^2+3}{8}. \tag{5.6}$$

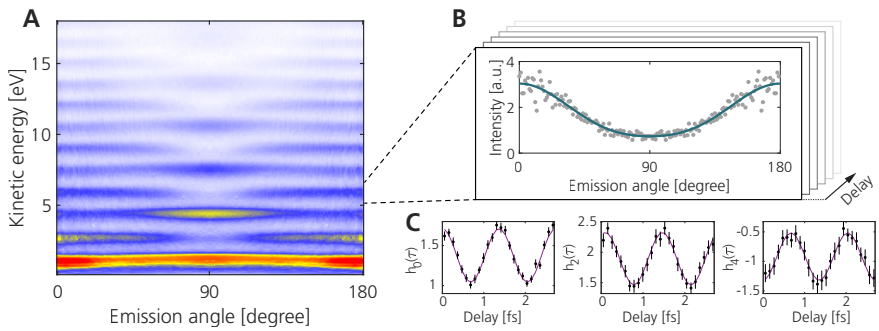

Figure 5.9: Data extraction principle for an angle resolved delay scan. (A) Angle-resolved photoelectron spectrum. **(B)** The signal (grey dots) is extracted by integrating across the energy region of one sideband. The fit function (blue) that determines the parameters is applied to the data. This procedure is repeated for all the delay steps. **(C)** Extracted $h_i(\tau)$ parameters as a function of delay for sideband 18. Panel (C) modified from [163]

The three coefficients $h_i(\tau)$ describe the anisotropy in the angular emission pattern averaged over all izionization channels and are retrieved from fitting the experimental data. The first coefficient $h_0(\tau)$ represents the angle-independent (isotropic) part of the electron emission. The second coefficient $h_2(\tau)$ is associated with the primary anisotropic term arising from interference between partial waves differing by $\Delta\lambda = 2$. For single-photon ionization, this corresponds to ϵs-ϵd wave interference, while in the two-photon (sideband) region, it includes ϵp-ϵf wave interference. Finally, the h_4 coefficient reflects higher-order angular structures, that arise from two-photon ionization channel interferences, capturing fine details of the angular emission pattern.

Figure 5.9 A shows the angle-resolved photoelectron spectrum. The sideband signal is extracted and a fit with equation 5.5 is performed for every delay step (Panel B).

The $h_i(\tau)$ coefficients are determined as a function of delay for all sidebands in the photoelectron spectrum (Panel C). Using the coefficients that have been retrieved and the phases from the XUV only case, the one-photon scattering phases and amplitudes of the angular momentum channels are extracted, and the results being compared to theoretical simulations, shown in Paper V.

For a complete derivation elaborating on the connection between the $h_i(\tau)$ coefficients and single photon amplitude, the interested reader is referred to the supplementary material of Paper V or the thesis by Jasper Peschel [159].

5.4.1 Data outlook

Similarly to the angle-resolved XUV–IR delay scan that have been used to present the analysis in Paper V, a large number of scans have been acquired for three other noble gases: argon, krypton, and xenon. Figure 5.10 shows the XUV-only signal (upper row) repeated from Figure 5.3 and the XUV–IR ionization signal (lower row) for the three gases after inversion, each folded into one quadrant. In argon and krypton, sidebands are clearly visible; however, in xenon, the distinction is less clear due to the blending of sidebands with the spin-orbit split.

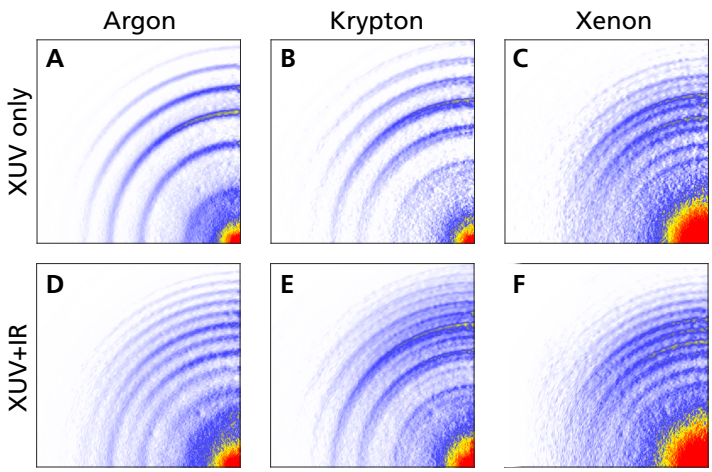

Figure 5.10: XUV and XUV+IR VMI for selected noble gases. (A-C) XUV-only VMI with argon, krypton and neon as target gas **(D-F)** XUV and IR VMI's show additional sidebands between the harmonic orders. The spin-orbit splitting in krypton and xenon is clearly visible. In xenon, the sidebands overlap with the level splitting.

In a preliminary analysis, the scans, spanning 10–20 fs with a resolution of 0.1 fs, have been individually binned into one oscillation cycle consisting of 20 bins and then inverse Abel transformed scan-by-scan. Multiple scans were combined post-inversion

to improve the SNR. Similar to the analysis in neon, the coefficients h_0, h_2 and h_4 were determined as functions of delay. Figure 5.11 shows the image sums of the scans, transformed into energy-over-angle form, with the coefficients extracted as functions of delay for the three gases.

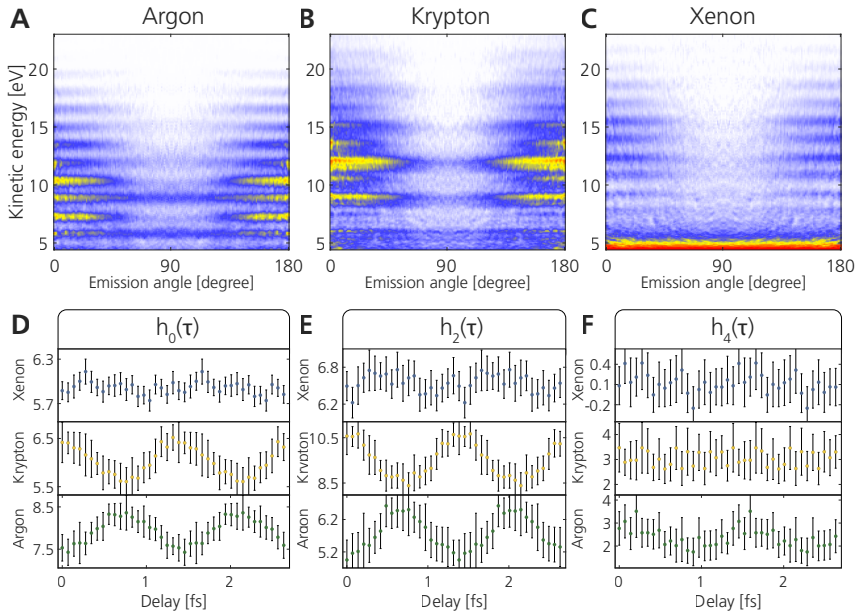

Figure 5.11: Angle-resolved VMIS images and coefficient extraction. (A-C) Angle-resolved VMIS images for argon, krypton and xenon respectively, combined scan image. **(D-F)** Delay dependence of the coefficients $h_i(\tau), i = 0, 2, 4$ for sideband 18, for the three noble gases.

The analysis of argon reveals clear oscillations in all three coefficients, highlighting a strong signal contrast. In krypton, however, the signal yield is lower. Additionally, spin-orbit splitting spreads the signal over a broader energy range, weakening the visibility of sideband oscillations and subsequently the oscillations in the h_4 coefficient, making the analysis of the two-photon channel interferences more challenging. For xenon, these challenges are even greater, as no clear oscillations are observed. The sidebands blend significantly with the spin-orbit split, making their separation difficult in the energy domain.

In this preliminary analysis, scans lasting 10–20 fs were binned into one oscillation cycle, but the current workflow combines scans only after they have been individually inverted. This approach does not leverage the potential improvement in the Abel inversion process that could come from combining data before inversion. Furthermore, the presented analysis only includes a subset of the available data, with 2 out of 33 scans analyzed for argon, 3 out of 29 for krypton, and 4 out of 9 for xenon. Xenon

remains particularly challenging due to its relatively low photoelectron signal yield, requiring longer scans with more acquisitions per step. A more sophisticated analysis incorporating all data subsets, capable of characterizing the phase and amplitude of the photoionization process—similar to what was performed in Paper V—is currently underway.

5.5 Non-linear XUV pump–XUV probe

XUV-pump XUV-probe schemes utilize two attosecond XUV pulses, one as the pump and the other as the probe. This allows for the direct observation of the underlying processes, in contrast to XUV–IR pump-probe schemes, where the IR pulse can induce additional dynamics that differ from those caused by XUV excitation. Specifically, XUV–IR interactions often involve multiphoton processes, adding complexity to the interpretation of the observed dynamics, whereas purely XUV-based methods rely on single-photon interactions, providing a more direct approach. To enter the nonlinear regime in which two XUV photons are absorbed, a high XUV intensity is required. Achieving this is inherently challenging, as HHG is already a nonlinear process with low conversion efficiency in the XUV range. Hence, reaching sufficiently high XUV intensities for nonlinear interactions necessitates both a high XUV flux and tight focusing on the target.

Historically, large-scale facilities such as Free Electron Laser (FEL) have been the primary sources capable of delivering sufficiently high intensities to reach the nonlinear XUV regime. However, FELs generally lack the same level of spatial and temporal coherence as HHG sources. This limitation arises from the self-amplified spontaneous emission (SASE) process in traditional FELs, which leads to lower coherence.

Additionally, most FELs do not produce pulses short enough to compete with attosecond pulses in duration. Advancements in seeded FELs have enabled sub-femtosecond pulse generation [164], but their limited shot-to-shot temporal stability and synchronization precision remain challenges for attosecond science applications [165]. Furthermore, the photon energy ranges accessible with short-duration FELs are typically in the X-ray regime, differing from those achieved with HHG sources. This makes the two technologies complementary as they are suited for investigating different processes. Because of this background, several beamlines have been designed to deliver a particularly high XUV intensity from HHG [133, 166, 167].

Neon is particularly interesting as a target for performing nonlinear XUV–XUV pump-probe experiments on HHG beamlines. The first ionization potential of neon is 21.56 eV, and the second ionization potential is $40.96\,\mathrm{eV}$, meaning that at least $62.52\,\mathrm{eV}$

is required to achieve double ionization. This double-ionization threshold often lies above the harmonic cutoff energy typically achieved in the experiment, which for the Intense XUV Beamline is below 50 eV under standard operating conditions.

This leaves the following ionization pathways, illustrated in Figure 5.12 A:

1. Two-photon Direct Double Ionization (DDI): This process requires the simultaneous absorption of two photons, $\mathrm{Ne} \xrightarrow{2\gamma} \mathrm{Ne}^{2+}$, with their combined energy satisfying $E_1 + E_2 \geq 62.52\,\mathrm{eV}$.
2. Sequential Double Ionization (SDI): Neon is first ionized to its singly charged state, $\mathrm{Ne} \xrightarrow{\gamma} \mathrm{Ne}^{+}$, by absorbing a photon with energy $E_1 \geq 21.56\,\mathrm{eV}$. While Ne^{+} remains in this ionized state, a second photon with energy $E_2 \geq 41\,\mathrm{eV}$ further ionizes it into the doubly charged state $\mathrm{Ne}^{+} \xrightarrow{\gamma} \mathrm{Ne}^{2+}$. Due to the relatively high threshold of the second ionization, the SDI channel can be effectively suppressed by reducing the harmonic cutoff energy by, e.g., adjusting the IR intensity in the generation medium [84].

Both processes involve the absorption of two photons, causing the double ionization yield to scale with the intensity squared, as expressed by $\mathrm{Ne}^{2+} \propto I^2$, in accordance with perturbation theory [43]. However, the ionization processes differ in their cross sections. The cross section for single ionization of neon is estimated to $\sigma_{\mathrm{I}}^{(1)} \approx 8 \times 10^{-18}$ cm^2 [168], while the cross section for ionization from the first to the second ionization state is slightly lower, at $\sigma_{\mathrm{II}}^{(1)} = 7 \times 10^{-18}$ cm^2 [84, 169].

In contrast, the direct double-ionization (DDI) process has a much smaller cross section because it requires the simultaneous absorption of two photons. This is reflected in the estimated cross section for DDI, which is on the order of $\sigma_{\mathrm{d}}^{(2)} \approx 1.6 \times 10^{-50}\,\mathrm{cm}^4$ s [169], and thus much smaller than the product of the two sequential ionization cross sections.

Sequential double ionization with a two-photon second-step ionization, as illustrated in Figure 5.12 A, refers to the ionization from the first to the second ionization threshold via a two-photon process. However, this process has an extremely low cross section as it involves three photons of which two have to coincide in time, and consequently a very low yield, making it negligible under typical experimental conditions.

To accurately assess the sequential ionization process, we introduce the concept of equivalent pulse duration, which represents the integrated duration of attosecond pulses within an entire driving laser pulse. To estimate the effective time window in which attosecond pulse trains are generated, we apply the earlier introduced power-law scaling (see Equation (4.19)). For a 9 fs driving laser pulse in argon, we can cal-

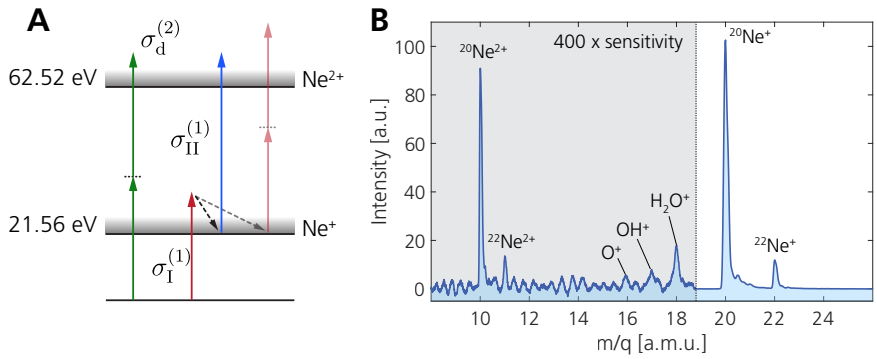

Figure 5.12: Double ionization of neon–principle and measurement. (A) Energy level scheme of Neon, indicating direct double ionization and sequential double ionization. **(B)** Mass-to-charge ratio retrieved from a ToF measurement in neon. The mass-to-charge ratios until ≈ 19 a.m.u features a high sensitivity signal resolving the Ne^{2+} peak, while the scale above this value showcase the Ne^+ ions with less measurement sensitivity. Between the two sides is an amplification factor of 400. The other peaks are identified as the typical background residuals in vacuum, such as water and oxygen.

culate an APT duration $\tau_{\mathrm{APT}} = 9\,\mathrm{fs}/\sqrt{2.6} \approx 5.6\,\mathrm{fs}$. Within this time, four attosecond pulses are emitted within the train. Since each attosecond pulse has a duration of $\approx 300\,\mathrm{as}$, the equivalent pulse duration is estimated to be $\tau = 1.2\,\mathrm{fs}$.

In the 2016 paper by Manschwetus et al. [84], the cross section of the second sequential ionization step was determined by measuring the ratio between the Ne^2+ and the Ne^+ yields $\mathcal{N}_s^{2+}/\mathcal{N}^+$. Under the assumption that sequential ionization is the dominant channel for Ne^{2+} production, the yield ratio is given by

$$\frac{\mathcal{N}_s^{2+}}{\mathcal{N}^+} = \frac{\sigma_{\mathrm{II}}^{(1)} F_{\mathrm{II}}}{2}\tau, \tag{5.7}$$

where F_{II} is the photon flux above $40.96\,\mathrm{eV}$. We can now use this relationship to compare the XUV flux of the new laser system with that of the old system.

Figure 5.12 B shows both the Ne^+ and Ne^{2+} signal using the OPCPA laser system. The ratio between the two peaks was calculated to be $\mathcal{N}_s^{2+}/\mathcal{N}^+ = 0.14\,\%$, which is $40\,\%$ of the value reported in 2016 ($0.35\,\%$). While the ratio appears significantly lower, it is important to account for the difference in equivalent pulse durations between the two systems.

The equivalent pulse duration in 2016 was estimated to be $\tau = 4.5\,\mathrm{fs}$, approximately four times longer than the pulse duration with the new laser system. Comparing how the pulse durations and yield ratio scale for both laser systems, it can be estimated that the flux of photons with $E_{\mathrm{ph}} \geq 40.96\,\mathrm{eV}$ has increased by a factor of ~ 1.5 with the new laser system.

However, this calculation must be interpreted with caution, as the ionization yields

exhibit different scaling behavior. While the yield of the DDI process is expected to scale linearly with the effective pulse duration, the yield of the SDI process scales quadratically [75, 76, 84]:

$$\frac{\mathcal{N}_s^{2+}}{\mathcal{N}_d^{2+}} = \frac{\left(\sigma_{\mathrm{I}}^{(1)} F\tau\right)\left(\sigma_{\mathrm{II}}^{(1)} F\tau\right)}{2\sigma_d^{(2)} F^2 \tau} = \frac{\sigma_{\mathrm{I}}^{(1)}\sigma_{\mathrm{II}}^{(1)}}{2\sigma_d^{(2)}}\tau. \tag{5.8}$$

This implies that there is an effective pulse duration τ at which the DDI surpasses the SDI. Theoretical calculations suggest that the transition between the two regimes is around 1 fs [170]. This could place the system in a regime where the contribution of the DDI channel becomes significant and cannot be ignored.

The implementation of the SDU to perform time- and/or XUV-intensity-resolved experiments has been a recurring focus throughout the work of this thesis. Promising progress was made up until the very last experiments conducted with the CPA laser system, as well as since the OPCPA laser system became operational. However, maintaining spatial overlap of both XUV beams over extended periods and across the scan range has proven challenging. With the new laser system's increased repetition rate and enhanced stability, significant advancements and meaningful results are expected in the near future.

Chapter 6

Summary and Outlook

This thesis focuses on the generation and application of an intense XUV attosecond light source. A major aspect of the work was improving the Intense XUV Beamline in Lund, which serves as the primary experimental setup. Systematic studies of the properties of HHG radiation were conducted, leading to strategies for minimizing chromatic aberrations and enabling high-intensity refocusing. This is particularly important for photoionization studies, especially in the nonlinear regime of the XUV spectral region. The key contributions of this thesis can be categorized into three main areas: setup improvement, characterization of HHG properties, and photoionization studies. These contributions are summarized below.

Setup improvement

Significant effort was devoted to upgrading the setup and adapting the beamline to be compatible with the specifications of the new laser system. Alongside numerous smaller modifications, a major contribution was the design of a chirped mirror compressor, as well as its integration and commissioning.

Additionally, alignment methods were refined, generation conditions optimized, and data analysis improved. These enhancements led to higher HHG yield, more stable experimental conditions, and overall improved data quality.

Characterization of HHG properties

Various aspects of high-order harmonic properties were investigated. By complementing experimental results with simulations based on the γ-model, Paper III explored

how the focusing properties of HHG can be optimized by controlling the generation conditions. In Paper I, the model was further extended to describe an astigmatic driver, and simulations based on experimental parameters demonstrated that complex patterns in the harmonic far-field spatial profile arise from astigmatism in the driving laser. This underscores the necessity of precise wavefront control and careful optimization of the generation conditions.

Paper II further demonstrated the strong relationship between the driving laser and HHG properties, showing that chromatic aberrations can be reduced by shaping the intensity profile of the fundamental field.

Finally, measurements at the Intense XUV Beamline in Lund and the SYLOS GHHG LONG beamline in Szeged confirmed the presence of two phase-matching regimes in HHG conversion efficiency, supporting the hyperbolic phase-matching theory previously developed by Weissenbilder et al. [36].

Photoionization studies

The generated pulses were used in photoionization experiments, where photoelectron energy and angular distributions were recorded for two-color ionization. These measurements were performed as a function of the delay between the XUV and an IR pulse. The study of neon shows that the variation of angular photoelectron emission in XUV–IR delay scans allows the characterization of single-photon ionization channels in neon, as described in Paper V. Beyond this, a large dataset involving other target gases was acquired, with a detailed analysis still underway.

Nonlinear two-photon double-ionization experiments in neon demonstrated that the beamline intensity in the target interaction region had indeed improved by a factor of approximately 1.5 compared to the decommissioned laser system. This places the setup in a parameter range where the XUV intensity is sufficient to comfortably access the nonlinear regime.

6.1 Outlook

During the completion of this work, several ideas and concepts emerged that have potential for further exploration but fall outside the immediate scope of this thesis. Two of these involve additional optimizations of the experimental setup, one pertains to improving data analysis, and one involves carrying out measurements that have yet to be successfully demonstrated.

Out-of-focus generation

Although out-of-focus geometry is discussed in this thesis, a systematic experimental investigation has not been carried out at the Intense XUV Beamline. A comprehensive study of out-of-focus generation would involve phase-matching simulations to determine whether macroscopic effects might favor a particular generation region before or after the focus. Subsequently, these findings should be validated experimentally—an investigation well-suited to the Intense XUV Beamline due to its adaptable focusing capabilities via the deformable mirror.

Semi-infinite gas cell

This thesis has also touched on the possibility of achieving high harmonic conversion efficiency by operating in a regime with lower gas density but a longer generation medium. Moreover, creating a plasma channel that regulates phase-matching conditions can effectively gate the pulse shape toward an isolated attosecond pulse [171]. However, the Intense XUV Beamline does not yet exploit this approach because such a gas medium poses technical challenges in maintaining a sharp gradient at the edges when transitioning into vacuum [172].

For this reason, work is underway to develop the design of a semi-infinite gas cell. To address large pressure gradients at the medium's edges, the use of chopper wheels has been proposed. If successful, this setup could provide a long generation medium with uniform gas density and well-defined boundaries, ultimately supporting the generation of isolated attosecond pulses.

Applying artificial intelligence for data analysis

The field of Artificial Intelligence (AI) has advanced rapidly in the past years, with tools increasingly available to the wider community. As a result, many areas of research are undergoing rapid transformation.

Data processing and result analysis in experiments could benefit significantly from deep learning. One example is the Abel inversion of electron velocity map images, as illustrated in Figure 6.1. The relationship between a velocity map image and the radial cross-section of the electron momentum distribution is well-defined and can be modeled via Monte Carlo simulations to create a comprehensive dataset. Experimental images and their classically inverted counterparts can also be incorporated into a large training set for such a model. Once the model has been trained, it can be applied to experimental velocity map images to retrieve the momentum distribution.

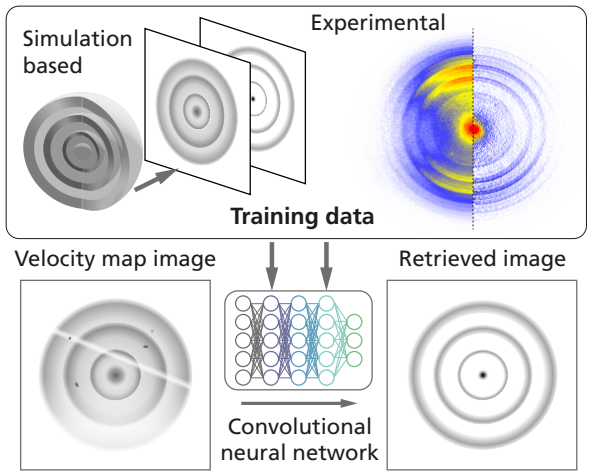

Figure 6.1: Example application for deep learning in velocity map image inversion. Simulations and experimentally inverted data (upper panel) can be used to train the model. Once trained, the model can invert future VMIS measurements significantly faster and with higher quality.

A well-trained deep learning model capable of retrieving inverted images would offer three key benefits:

1. **Pattern completion**: Deep learning models can predict missing or incomplete patterns in the data, even if the original dataset has low statistics.
2. **Distinguishing features and noise reduction**: A well-trained model can distinguish between real electron signals and background noise—such as scattered photons, hot/dark spots on the Micro-Channel Plate (MCP), or other artifacts—thereby improving data quality and the fidelity of reconstructed momentum distributions.
3. **Faster retrieval speed**: After training, the model can perform inversions orders of magnitude faster than conventional algorithms.

These advantages make a deep learning approach particularly appealing for velocity map image inversion and have the potential to significantly enhance both the speed

and accuracy of photoelectron spectroscopy. Indeed, other research areas have already demonstrated the feasibility and benefits of applying deep learning to Abel inversion [173].

Time-resolved nonlinear XUV-measurements

Despite extensive efforts and notable progress toward higher intensity, there remains room for further setup improvement. In the final weeks before the shutdown and decommissioning of the CPA laser system, time-resolved XUV–XUV scans were performed. Unfortunately, that period was too brief to acquire sufficient statistics for conclusive results.

The installation of the new laser system introduced additional challenges that required shifting the experimental focus. Overall, the transition proceeded smoothly, but a few issues persist—such as achieving sufficient target gas densities at the higher repetition rate. Spatiotemporal alignment of the two XUV-beams and scanning procedures are challenging, requiring careful coordination of multiple system parameters to maintain stability over extended measurement periods while ensuring clear signals and high-statistics data. Nevertheless, the experimental setup is close to being fully optimized, and obtaining reliable measurements may only be a matter of a few months [174].

Acknowledgements

Beginning with my master's project in 2019, I have spent quite some time in the Attogroup during which I have met and worked with many bright and pleasant people. This thesis represents contributions from all of them, and I am thankful for all the exchanges, discussions, and collaborations that led to it.

First, I'd like to thank my main supervisor, Per Eng-Johnsson, for the continuous support over the years. Per, your calm and optimistic attitude—even when the lab was flooded—has made a huge difference. Whenever things didn't go as planned, you found a way to shift the perspective, see it as progress, and explore a creative way to approach it from another angle. That said, the sheer number of times we've coincidentally run into each other for a spontaneous coffee at 9:00 on Monday mornings is statistically suspicious and possibly concerning.

I would like to thank my co-supervisors Anne L'Huillier and Cord Arnold. Cord, your knowledge is truly impressive. Thank you for the constructive conversations, your advice on optics questions, and for looking after Jupiter. Your role as the Attogroup's talent scout is crucial. Though the number of Germans in the group is getting pretty low, maybe you can do something about that! Anne, you are a person of integrity and have never lost your curiosity throughout your scientific career. It meant a lot to feel recognized when you stopped by the labs in the evenings to see what was going on—though it was sometimes at unfortunate moments, like when the laser refused to work or when questionable music was playing at a questionable volume.

I am very grateful for the people I have worked closely with. Elisa, thank you for your kindness and for keeping an overview that helped move things forward when they weren't on my radar. You have exciting times ahead, and I am (h)appy for you! Vénus, thank you for the time in the lab and the random talks. It was always a pleasure to turn the light back on when you accidentally switched it off. Keep up with all your hobbies—it's fun watching you dive into something new every week. Aishwarya, thank you for joining the team, and all the best for your PhD! Fuoco nel fuoco, Federico, Master Chief. Uuh, those legendary nights when we were fighting for a

better sideband signal and saving Reach from the Covenant were among the best nights of my PhD. You are a guy with extraordinary capabilities and will have a bright future in science. Jasper, thank you for your support when I started my Master's and for becoming a friend. You sparked many interests and ideas in me. We created the best-looking office at AF and lowered Limhamn's age average. I miss our aviation talks and booking discussions.

A huge thanks to the co-workers who were part of the journey on the Intense XUV beamline: Ammar Bin Wahid, Jan Lahl, Hampus Wikmark, Sylvain Maclot, Giada Cantono, and Hugo Dacasa. Maria Hoflund, thank you for getting the boat together. I wouldn't want to miss the time on the sea. To the bachelor's, master's, and internship students: Nils Weber, Robert Petersen, Artemiy Khoptyar, and Erik Leijon—never lose your curiosity; it's what drives research. You can't imagine how much I learned from watching you learning.

I would like to thank everyone in the Attogroup who make this workplace an extraordinary one! Ivan, you are a true friend, and I'm glad we took that bold step of crossing the door into Kvarters Krog, which that day gained a loyal customer for their pizzas. Thank you for the time together at Eriksdalsgatan. Chen Guo, thank you for your great sense of humor and our nice conversations about all kinds of interesting stuff! My travel companions in the US and A(sia): (Jasper), Anka, Robin, and David. Taking an Uber from Orlando to Miami, sailing to the Bahamas, and riding through the island on the back of a pickup truck is something I'll remember for life. It wouldn't have happened if you weren't such easygoing and spontaneous people. The same goes for our trips to Korea and the Philippines. Nothing beats jumping into the crystal-clear Dayhag Falls with you guys. As for the car, Anka, at one point, I really thought we were going to get stranded in those mountains, but it was worth every kilometer.

Thanks to all the other fantastic people in the Attogroup with whom I had the pleasure of spending time and having legendary PhD defense parties. Anne-Lise, Caroline, Daniel, Edoardo, Gaspard, Mattias, Melvin, Nedjma, Praveen, Yuman, and the many others who have been part of the group before.

There are also many people in the division with whom I worked, taught, chatted, and had a good time. Anders Persson, thank you for always bringing us the brightest light and enriching the lab days with fun laser stories. No matter what breaks, you always fix it! Mathieu, merci pour nos conversations sur tout et rien, toujours un plaisir! I'm glad you picked up the pump. Thank you, Claes-Göran for diving through the DM electronics. I would have given up without your persistence. Thank you, Åke, for keeping the IT running, and the discussion about fine electronics, Johan Renders, for being Jupiter's hero, Eric Nilsson, who climbs like there is no gravity and the High-intensity Beamline team that is always just a door-knock away: Cornelia Gustafsson,

Andrea Angella, Erik Löfquist, Flanish D´Souza and Olle Lundh.

I would like to thank the HELIOS people in Hamburg, namely, Francesca Calegari and Stefanie Tille. It is an excellent graduate school, and I feel fortunate to have been in the first generation of students.

I want to thank all my friends outside work for their advice, emotional support and encouragement during the time of my PhD. First of all, Bernardo Paul, who has been a constant in my life since I moved to Sweden! Philip Aussem and Felix Bos, we don´t meet that often, but it's a good feeling to know you're close. Ludvig, thank you for your support. You have changed a lot, and I wouldn´t be who I am without you. I thank Corinna Vonau, Chefin der Herzen, for convincing me to begin studying physics. You believed in me more than I did– Always. Danke für *Kaffee warm* und *Trümmer*. Dir, Alexander und Jens alles Gute. Michael Scharwaechter, ohne den Zusammenhalt im Grundstudium hätte ich vermutlich frustriert die Segel gestrichen. Die Straße ist gekehrt.

Ich bedanke mich bei meiner Familie für die stetige Unterstützung auf meinem Werdegang, ohne deren Zutun diese Arbeit nicht ermöglicht worden wäre.

Finally, I would like to thank Eva for her unwavering support throughout this journey. I am happy our paths crossed during this beamtime. You are a wonderful person, partner and friend to me, and I am grateful to have you in my life.

No dogs were harmed during the production of this thesis.

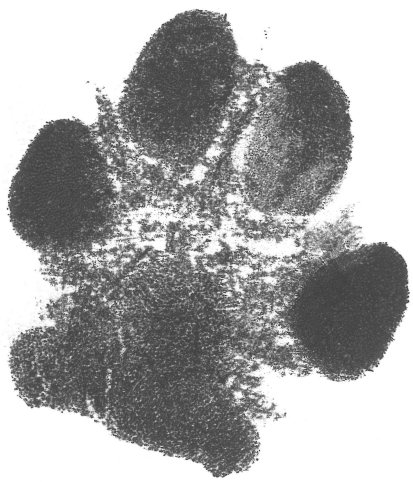

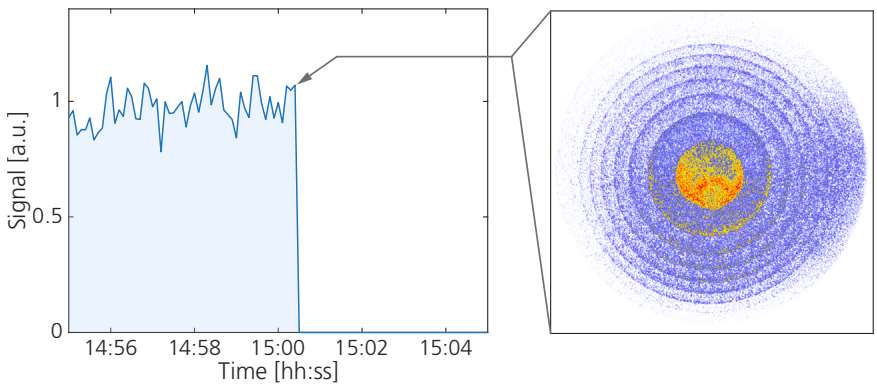

Figure 6.2: Last photons generated by the old Terawatt laser. Left: VMIS signal on the final day of the TW laser system operation (Monday, May 8, 2023). Right: Very last photoelectrons generated by the Terawatt laser light. Thank you for shining bright for 32 years.

References

[1] A. Simon, M. Rapacioli, G. Rouaut, G. Trinquier, and F. X. Gadéa, «Dissociation of polycyclic aromatic hydrocarbons: molecular dynamics studies», Philosophical Transactions of the Royal Society A: Mathematical, Physical and Engineering Sciences **375**, 20160195 (2017).

[2] D. M. Carey and G. M. Korenowski, «Measurement of the raman spectrum of liquid water», The Journal of chemical physics **108**, 2669 (1998).

[3] T. H. Maiman et al., «Stimulated optical radiation in ruby», (1960).

[4] F. J. McClung and R. W. Hellwarth, «Giant optical pulsations from ruby», Applied Optics **1**, 103 (1962).

[5] L. Hargrove, R. L. Fork, and M. Pollack, «Locking of he–ne laser modes induced by synchronous intracavity modulation», Applied Physics Letters **5**, 4 (1964).

[6] S. Svanberg, J. Larsson, A. Persson, and C. .-. Wahlström, «Lund high-power laser facility – systems and first results», Physica Scripta **49**, 187 (1994).

[7] A. DeMaria, D. Stetser, and H. Heynau, «Self mode-locking of lasers with saturable absorbers», Applied Physics Letters **8**, 174 (1966).

[8] C. Shank and E. Ippen, «Subpicosecond kilowatt pulses from a mode-locked cw dye laser», Applied Physics Letters **24**, 373 (1974).

[9] R. Fork, B. Greene, and C. V. Shank, «Generation of optical pulses shorter than 0.1 psec by colliding pulse mode locking», Applied Physics Letters **38**, 671 (1981).

[10] D. Strickland and G. Mourou, «Compression of amplified chirped optical pulses», Optics communications **55**, 447 (1985).

[11] P. Maine, D. Strickland, P. Bado, M. Pessot, and G. Mourou, «Generation of ultrahigh peak power pulses by chirped pulse amplification», IEEE Journal of Quantum electronics **24**, 398 (1988).

[12] D. E. Spence, P. N. Kean, and W. Sibbett, «60-fsec pulse generation from a self-mode-locked ti: sapphire laser», Optics letters **16**, 42 (1991).

[13] A. Dubietis, G. Jonušauskas, and A. Piskarskas, «Powerful femtosecond pulse generation by chirped and stretched pulse parametric amplification in bbo crystal», Optics Communications **88**, 437 (1992).

[14] M. Nisoli, S. De Silvestri, O. Svelto, R. Szipöcs, K. Ferencz, C. Spielmann, S. Sartania, and F. Krausz, «Compression of high-energy laser pulses below 5 fs», Optics letters **22**, 522 (1997).

[15] P.-M. Paul, E. S. Toma, P. Breger, G. Mullot, F. Augé, P. Balcou, H. G. Muller, and P. Agostini, «Observation of a train of attosecond pulses from high harmonic generation», Science **292**, 1689 (2001).

[16] R. Lopez-Martens, K. Varjú, P. Johnsson, J. Mauritsson, Y. Mairesse, P. Salieres, M. B. Gaarde, K. J. Schafer, A. Persson, S. Svanberg, et al., «Amplitude and phase control of attosecond light pulses», Physical Review Letters **94**, 033001 (2005).

[17] G. Sansone, E. Benedetti, F. Calegari, C. Vozzi, L. Avaldi, R. Flammini, L. Poletto, P. Villoresi, C. Altucci, R. Velotta, S. Stagira, S. D. Silvestri, and M. Nisoli, «Isolated single-cycle attosecond pulses», Science **314**, 443 (2006).

[18] E. Goulielmakis, M. Schultze, M. Hofstetter, V. S. Yakovlev, J. Gagnon, M. Uiberacker, A. L. Aquila, E. Gullikson, D. T. Attwood, R. Kienberger, et al., «Single-cycle nonlinear optics», Science **320**, 1614 (2008).

[19] K. Zhao, Q. Zhang, M. Chini, Y. Wu, X. Wang, and Z. Chang, «Tailoring a 67 attosecond pulse through advantageous phase-mismatch», Optics letters **37**, 3891 (2012).

[20] J. Li, X. Ren, Y. Yin, K. Zhao, A. Chew, Y. Cheng, E. Cunningham, Y. Wang, S. Hu, Y. Wu, et al., «53-attosecond x-ray pulses reach the carbon k-edge», Nature communications **8**, 186 (2017).

[21] T. Gaumnitz, A. Jain, Y. Pertot, M. Huppert, I. Jordan, F. Ardana-Lamas, and H. J. Wörner, «Streaking of 43-attosecond soft-x-ray pulses generated by a passively cep-stable mid-infrared driver», Optics express **25**, 27506 (2017).

[22] P. F. Moulton, «Spectroscopic and laser characteristics of ti: al 2 o 3», JOSA B **3**, 125 (1986).

[23] C. Radier, O. Chalus, M. Charbonneau, S. Thambirajah, G. Deschamps, S. David, J. Barbe, E. Etter, G. Matras, S. Ricaud, et al., «10 pw peak power femtosecond laser pulses at eli-np», High Power Laser Science and Engineering **10**, e21 (2022).

[24] Y. Peng, Y. Xu, L. Yu, X. WANG, Y. LI, X. LU, C. WANG, J. LIU, C. ZHAO, Y. LIU, et al., «Overview and status of station of extreme light toward 100 pw», The Review of Laser Engineering **49**, 93 (2021).

[25] J. Hecht, «Short history of laser development», Optical engineering **49**, 091002 (2010).

[26] A. McPherson, G. Gibson, H. Jara, U. Johann, T. S. Luk, I. A. McIntyre, K. Boyer, and C. K. Rhodes, «Studies of multiphoton production of vacuum-ultraviolet radiation in the rare gases», J. Opt. Soc. Am. B **4** (1987).

[27] M. Ferray, A. L'Huillier, X. F. Li, L. A. Lompre, G. Mainfray, and C. Manus, «Multiple-harmonic conversion of 1064 nm radiation in rare gases», Journal of Physics B: Atomic, Molecular and Optical Physics **21**, L31 (1988).

[28] A. L'Huillier and P. Balcou, «High-order harmonic generation in rare gases with a 1-ps 1053-nm laser», Physical Review Letters **70**, 774 (1993).

[29] K. Kulander, K. Schafer, and J. Krause, «Dynamics of short-pulse excitation, ionization and harmonic conversion», Super-intense laser-atom physics, 95 (1993).

[30] P. B. Corkum, «Plasma perspective on strong field multiphoton ionization», Physical review letters **71**, 1994 (1993).

[31] M. Lewenstein, P. Balcou, M. Y. Ivanov, A. L'huillier, and P. B. Corkum, «Theory of high-harmonic generation by low-frequency laser fields», Physical Review A **49**, 2117 (1994).

[32] P. Antoine, A. L'huillier, and M. Lewenstein, «Attosecond pulse trains using high–order harmonics», Physical Review Letters **77**, 1234 (1996).

[33] M. Hentschel, R. Kienberger, C. Spielmann, G. A. Reider, N. Milosevic, T. Brabec, P. Corkum, U. Heinzmann, M. Drescher, and F. Krausz, «Attosecond metrology», Nature **414**, 509 (2001).

[34] S. Grundmann, D. Trabert, K. Fehre, N. Strenger, A. Pier, L. Kaiser, M. Kircher, M. Weller, S. Eckart, L. P. H. Schmidt, et al., «Zeptosecond birth time delay in molecular photoionization», Science **370**, 339 (2020).

[35] The Royal Swedish Academy of Sciences, *The nobel prize in physics 2023 - summary*, Accessed: 2025-01-07, 2023, `https://www.nobelprize.org/prizes/physics/2023/summary/`.

[36] R. Weissenbilder, S. Carlström, L. Rego, C. Guo, C. Heyl, P. Smorenburg, E. Constant, C. Arnold, and A. L'huillier, «How to optimize high-order harmonic generation in gases», Nature Reviews Physics **4**, 713 (2022).

[37] J. L. Krause, K. J. Schafer, and K. C. Kulander, «High-order harmonic generation from atoms and ions in the high intensity regime», Physical Review Letters **68**, 3535 (1992).

[38] C. Kan, C. Capjack, R. Rankin, and N. Burnett, «Spectral and temporal structure in high harmonic emission from ionizing atomic gases», Physical Review A **52**, R4336 (1995).

[39] M. Lewenstein, P. Salieres, and A. L'huillier, «Phase of the atomic polarization in high-order harmonic generation», Physical Review A **52**, 4747 (1995).

[40] K. Varjú, Y. Mairesse, B. Carré, M. B. Gaarde, P. Johnsson, S. Kazamias, R. López-Martens, J. Mauritsson, K. Schafer, P. Balcou, et al., «Frequency chirp of harmonic and attosecond pulses», Journal of Modern Optics **52**, 379 (2005).

[41] R. Weissenbilder, «Optimization of high-order harmonic generation for attosecond science», PhD thesis (Lund University, 2023).

[42] A. Saenz and P. Lambropoulos, «Theoretical two-, three-and four-photon ionization cross sections of helium in the xuv range», Journal of Physics B: Atomic, Molecular and Optical Physics **32**, 5629 (1999).

[43] B. E. Saleh and M. C. Teich, «Beam optics», in *Fundamentals of photonics, second edition* (John Wiley & Sons, Ltd, 2007) Chap. 21, pp. 873–935.

[44] C. Winterfeldt, C. Spielmann, and G. Gerber, «Colloquium: optimal control of high-harmonic generation», Reviews of Modern Physics **80**, 117 (2008).

[45] J. Eberly, Q. Su, and J. Javanainen, «Nonlinear light scattering accompanying multiphoton ionization», Physical review letters **62**, 881 (1989).

[46] K. Kulander and B. Shore, «Calculations of multiple-harmonic conversion of 1064-nm radiation in xe», Physical review letters **62**, 524 (1989).

[47] A. L'Huillier, K. J. Schafer, and K. C. Kulander, «Theoretical aspects of intense field harmonic generation», Journal of Physics B: Atomic, Molecular and Optical Physics **24**, 3315 (1991).

[48] M. Lewenstein, P. Balcou, M. Y. Ivanov, A. L'huillier, and P. B. Corkum, «Theory of high-harmonic generation by low-frequency laser fields», Physical Review A **49**, 2117 (1994).

[49] K. Amini, J. Biegert, F. Calegari, A. Chacón, M. F. Ciappina, A. Dauphin, D. K. Efimov, C. F. de Morisson Faria, K. Giergiel, P. Gniewek, et al., «Symphony on strong field approximation», Reports on Progress in Physics **82**, 116001 (2019).

[50] M. B. Gaarde, F. Salin, E. Constant, P. Balcou, K. Schafer, K. Kulander, and A. L'Huillier, «Spatiotemporal separation of high harmonic radiation into two quantum path components», Physical Review A **59**, 1367 (1999).

[51] C. Guo, A. Harth, S. Carlström, Y.-C. Cheng, S. Mikaelsson, E. Marsell, C. Heyl, M. Miranda, M. Gisselbrecht, M. B. Gaarde, et al., «Phase control of attosecond pulses in a train», Journal of Physics B: Atomic, Molecular and Optical Physics **51**, 034006 (2018).

[52] H. Wikmark, C. Guo, J. Vogelsang, P. W. Smorenburg, H. Coudert-Alteirac, J. Lahl, J. Peschel, P. Rudawski, H. Dacasa, S. Carlström, S. Maclot, M. B. Gaarde, P. Johnsson, C. L. Arnold, and A. L'Huillier, «Spatiotemporal coupling of attosecond pulses», Proceedings of the National Academy of Sciences **116**, 4779 (2019).

[53] H. Mashiko, S. Gilbertson, C. Li, S. D. Khan, M. M. Shakya, E. Moon, and Z. Chang, «Double optical gating of high-order harmonic generation with carrier-envelope phase stabilized lasers», Phys. Rev. Lett. **100**, 103906 (2008).

[54] F. Ferrari, F. Calegari, M. Lucchini, C. Vozzi, S. Stagira, G. Sansone, and M. Nisoli, «High-energy isolated attosecond pulses generated by above-saturation few-cycle fields», Nature Photonics **4**, 875 (2010).

[55] E. J. Takahashi, P. Lan, O. D. Mücke, Y. Nabekawa, and K. Midorikawa, «Infrared two-color multicycle laser field synthesis for generating an intense attosecond pulse», Physical review letters **104**, 233901 (2010).

[56] K. T. Kim, C. M. Kim, M.-G. Baik, G. Umesh, and C. H. Nam, «Single sub-50-attosecond pulse generation from chirp-compensated harmonic radiation using material dispersion», Physical Review A—Atomic, Molecular, and Optical Physics **69**, 051805 (2004).

[57] K. T. Kim, K. S. Kang, M. N. Park, T. Imran, G. Umesh, and C. H. Nam, «Self-compression of attosecond high-order harmonic pulses», Physical review letters **99**, 223904 (2007).

[58] D. H. Ko, K. T. Kim, J. Park, J.-h. Lee, and C. H. Nam, «Attosecond chirp compensation over broadband high-order harmonics to generate near transform-limited 63 as pulses», New Journal of Physics **12**, 063008 (2010).

[59] A. Wonisch, U. Neuhäusler, N. M. Kabachnik, T. Uphues, M. Uiberacker, V. Yakovlev, F. Krausz, M. Drescher, U. Kleineberg, and U. Heinzmann, «Design, fabrication, and analysis of chirped multilayer mirrors for reflection of extreme-ultraviolet attosecond pulses», Applied optics **45**, 4147 (2006).

[60] M. Hofstetter, M. Schultze, M. Fieß, B. Dennhardt, A. Guggenmos, J. Gagnon, V. S. Yakovlev, E. Goulielmakis, R. Kienberger, E. M. Gullikson, et al., «Attosecond dispersion control by extreme ultraviolet multilayer mirrors», Optics Express **19**, 1767 (2011).

[61] Y. Mairesse, A. De Bohan, L. Frasinski, H. Merdji, L. Dinu, P. Monchicourt, P. Breger, M. Kovacev, R. Taïeb, B. Carré, et al., «Attosecond synchronization of high-harmonic soft x-rays», Science **302**, 1540 (2003).

[62] K. Kovács and V. Tosa, «Macroscopic attosecond chirp compensation», Optics Express **27**, 21872 (2019).

[63] M. Ferray, A. L'Huillier, X. F. Li, L. A. Lompre, G. Mainfray, and C. Manus, «Multiple-harmonic conversion of 1064 nm radiation in rare gases», Journal of Physics B: Atomic, Molecular and Optical Physics **21** (1988).

[64] T. T. Luu, Z. Yin, A. Jain, T. Gaumnitz, Y. Pertot, J. Ma, and H. J. Wörner, «Extreme–ultraviolet high–harmonic generation in liquids», Nature communications **9**, 3723 (2018).

[65] S. Ghimire, A. D. DiChiara, E. Sistrunk, P. Agostini, L. F. DiMauro, and D. A. Reis, «Observation of high-order harmonic generation in a bulk crystal», Nature physics **7**, 138 (2011).

[66] S. Ghimire and D. A. Reis, «High-harmonic generation from solids», Nature physics **15**, 10 (2019).

[67] W. M. Haynes, ed., *Crc handbook of chemistry and physics*, 95th (CRC Press, Boca Raton, FL, 2014), pp. 10–197.

[68] T. N. Olney, N. Cann, G. Cooper, and C. Brion, «Absolute scale determination for photoabsorption spectra and the calculation of molecular properties using dipole sum-rules», Chemical physics **223**, 59 (1997).

[69] P. Maker, R. Terhune, M. Nisenoff, and C. Savage, «Effects of dispersion and focusing on the production of optical harmonics», Physical review letters **8**, 21 (1962).

[70] E. Constant, D. Garzella, P. Breger, E. Mével, C. Dorrer, C. Le Blanc, F. Salin, and P. Agostini, «Optimizing high harmonic generation in absorbing gases: model and experiment», Physical Review Letters **82**, 1668 (1999).

[71] M. B. Gaarde, J. L. Tate, and K. J. Schafer, «Macroscopic aspects of attosecond pulse generation», Journal of Physics B: Atomic, Molecular and Optical Physics **41**, 132001 (2008).

[72] C. Heyl, C. L. Arnold, A. Couairon, and A. L'Huillier, «Introduction to macroscopic power scaling principles for high-order harmonic generation», Journal of Physics B: Atomic, Molecular and Optical Physics **50**, 013001 (2016).

[73] B. E. Saleh and M. C. Teich, «Beam optics», in *Fundamentals of photonics, second edition* (John Wiley & Sons, Ltd, 2007) Chap. 3, pp. 74–101.

[74] N. Papadogiannis, L. Nikolopoulos, D. Charalambidis, G. D. Tsakiris, P. Tzallas, and K. Witte, «On the feasibility of performing non-linear autocorrelation with attosecond pulse trains», Applied Physics B **76**, 721 (2003).

[75] P. Tzallas, E. Skantzakis, L. Nikolopoulos, G. D. Tsakiris, and D. Charalambidis, «Extreme-ultraviolet pump–probe studies of one-femtosecond-scale electron dynamics», Nature Physics **7**, 781 (2011).

[76] I. Orfanos, E. Skantzakis, A. Nayak, M. Dumergue, S. Kühn, G. Sansone, M. F. Kling, H. Schröder, B. Bergues, J. Csontos, et al., «Two-xuv-photon double ionization of neon», Physical Review A **106**, 043117 (2022).

[77] M. Kretschmar, A. Hadjipittas, B. Major, J. Tümmler, I. Will, T. Nagy, M. Vrakking, A. Emmanouilidou, and B. Schütte, «Attosecond investigation of extreme-ultraviolet multi-photon multi-electron ionization», Optica **9**, 639 (2022).

[78] E. J. Takahashi, Y. Nabekawa, and K. Midorikawa, «Low-divergence coherent soft x-ray source at 13 nm by high-order harmonics», Applied physics letters **84**, 4 (2004).

[79] E. Takahashi, Y. Nabekawa, T. Otsuka, M. Obara, and K. Midorikawa, «Generation of highly coherent submicrojoule soft x rays by high-order harmonics», Physical Review A **66**, 021802 (2002).

[80] J.-F. Hergott, M. Kovacev, H. Merdji, C. Hubert, Y. Mairesse, E. Jean, P. Breger, P. Agostini, B. Carré, and P. Salières, «Extreme-ultraviolet high-order harmonic pulses in the microjoule range», Physical Review A **66**, 021801 (2002).

[81] C. Heyl, J. Güdde, A. L'Huillier, and U. Höfer, «High-order harmonic generation with μj laser pulses at high repetition rates», Journal of Physics B: Atomic, Molecular and Optical Physics **45**, 074020 (2012).

[82] J. Rothhardt, M. Krebs, S. Hädrich, S. Demmler, J. Limpert, and A. Tünnermann, «Absorption-limited and phase-matched high harmonic generation in the tight focusing regime», New Journal of Physics **16**, 033022 (2014).

[83] C. M. Heyl, H. Coudert-Alteirac, M. Miranda, M. Louisy, K. Kovács, V. Tosa, E. Balogh, K. Varjú, A. L'Huillier, A. Couairon, et al., «Scale-invariant nonlinear optics in gases», Optica **3**, 75 (2016).

[84] B. Manschwetus, L. Rading, F. Campi, S. Maclot, H. Coudert-Alteirac, J. Lahl, H. Wikmark, P. Rudawski, C. Heyl, B. Farkas, et al., «Two-photon double ionization of neon using an intense attosecond pulse train», Physical Review A **93**, 061402 (2016).

[85] ELI-ALPS, *SYLOS GHHG LONG Beamline Overview*, https://up.eli-laser.eu/equipment/sylos-ghhg-long-562069531, Accessed: 2024-12-13.

[86] T. R. S. A. of Sciences, *The nobel prize in physics 2018*, https://www.nobelprize.org/prizes/physics/2018/summary/, Accessed: 2024-12-21, 2018.

[87] M. Zavelani-Rossi, F. Lindner, C. Le Blanc, G. Chériaux, and J. Chambaret, «Control of thermal effects for high-intensity ti: sapphire laser chains», Applied Physics B **70**, S193 (2000).

[88] D. B. Joyce and F. Schmid, «Progress in the growth of large scale ti: sapphire crystals by the heat exchanger method (hem) for petawatt class lasers», Journal of crystal growth **312**, 1138 (2010).

[89] T. Kobayashi, «Femtosecond noncollinear parametric amplification and carrier-envelope phase control», in *Femtosecond optical frequency comb: principle, operation, and applications*, edited by J. Ye and S. T. Cundiff (Springer US, Boston, MA, 2005), pp. 133–175.

[90] A. Y. Naumov, D. Villeneuve, and H. Niikura, «High conversion efficiency of an optical parametric amplifier pumped by 1 khz ti: sapphire laser pulses for tunable high-harmonic generation», Optics Express **28**, 4088 (2020).

[91] L. Conversion, *Topas prime-he high-energy opa*, https://lightcon.com/product/topas-prime-high-energy-opa/, Accessed: 2024-12-21.

[92] C.-G. Wahlström, J. Larsson, A. Persson, T. Starczewski, S. Svanberg, P. Salieres, P. Balcou, and A. L'Huillier, «High-order harmonic generation in rare gases with an intense short-pulse laser», Physical Review A **48**, 4709 (1993).

[93] *Private conversation with Anders Persson*, Jan. 2025.

[94] C. Gustafsson, E. Löfquist, K. Svendsen, A. Angella, A. Persson, and O. Lundh, «Combined plasma lens and rephasing stage for a laser wakefield accelerator», Scientific Reports **14**, 26286 (2024).

[95] Amplitude Laser, *Dazzler Product Sheet*, https://amplitude-laser.com/products/femtosecond-lasers/instrumentation-lasers-femtosecondes/dazzler/, Accessed: 2024-12-22.

[96] S. L. Shapiro and D. H. Auston, *Ultrashort light pulses: picosecond techniques and applications* (Springer, 1977), pp. 83–122.

[97] D. Kane and R. Trebino, «Characterization of arbitrary femtosecond pulses using frequency-resolved optical gating», IEEE Journal of Quantum Electronics **29**, 571 (1993).

[98] R. Trebino and D. J. Kane, «Using phase retrieval to measure the intensity and phase of ultrashort pulses: frequency-resolved optical gating», JOSA A **10**, 1101 (1993).

[99] C. Iaconis and I. A. Walmsley, «Spectral phase interferometry for direct electric-field reconstruction of ultrashort optical pulses», Optics letters **23**, 792 (1998).

[100] M. Miranda, T. Fordell, C. Arnold, A. L'Huillier, and H. Crespo, «Simultaneous compression and characterization of ultrashort laser pulses using chirped mirrors and glass wedges», Optics express **20**, 688 (2011).

[101] M. Miranda, C. L. Arnold, T. Fordell, F. Silva, B. Alonso, R. Weigand, A. L'Huillier, and H. Crespo, «Characterization of broadband few-cycle laser pulses with the d-scan technique», Optics express **20**, 18732 (2012).

[102] M. Louisy, C. Guo, L. Neoričić, S. Zhong, A. L'Huillier, C. L. Arnold, and M. Miranda, «Compact single-shot d-scan setup for the characterization of few-cycle laser pulses», Applied Optics **56**, 9084 (2017).

[103] I. Sytcevich, C. Guo, S. Mikaelsson, J. Vogelsang, A.-L. Viotti, B. Alonso, R. Romero, P. T. Guerreiro, Í. J. Sola, A. L'Huillier, et al., «Characterizing ultrashort laser pulses with second harmonic dispersion scans», Journal of the Optical Society of America B **38**, 1546 (2021).

[104] I. Sytcevich, «Generation, characterization and application of infrared few-cycle light pulses», (2022).

[105] J. A. Nelder and R. Mead, «A simplex method for function minimization», The computer journal **7**, 308 (1965).

[106] E. Escoto, A. Tajalli, T. Nagy, and G. Steinmeyer, «Advanced phase retrieval for dispersion scan: a comparative study», Journal of the Optical Society of America B **35**, 8 (2017).

[107] S. Kleinert, A. Tajalli, T. Nagy, and U. Morgner, «Rapid phase retrieval of ultrashort pulses from dispersion scan traces using deep neural networks», Optics letters **44**, 979 (2019).

[108] F. Brizuela, C. Heyl, P. Rudawski, D. Kroon, L. Rading, J. M. Dahlström, J. Mauritsson, P. Johnsson, C. Arnold, and A. L'Huillier, «Efficient high-order harmonic generation boosted by below-threshold harmonics», Scientific reports **3**, 1410 (2013).

[109] P. Rudawski, C. Heyl, F. Brizuela, J. Schwenke, A. Persson, E. Mansten, R. Rakowski, L. Rading, F. Campi, B. Kim, et al., «A high-flux high-order harmonic source», Review of Scientific Instruments **84** (2013).

[110] O. Svelto, in *Principles of lasers*, 5th (Springer, Boston, MA, 2010) Chap. 12.5.1, pp. 536–541.

[111] N. Bonod and J. Neauport, «Diffraction gratings: from principles to applications in high-intensity lasers», Advances in Optics and Photonics **8**, 156 (2016).

[112] AttoTech, *Gro01 product page*, Accessed: 2024-12-28, 2024, `https://attotech.se/GR001.html`.

[113] H. Coudert-Alteirac, H. Dacasa, F. Campi, E. Kueny, B. Farkas, F. Brunner, S. Maclot, B. Manschwetus, H. Wikmark, J. Lahl, et al., «Micro-focusing of broadband high-order harmonic radiation by a double toroidal mirror», Applied Sciences **7**, 1159 (2017).

[114] H. Wikmark, *Spatial and temporal aspects of intense attosecond pulses for pump-probe experiments* (PhD thesis, Department of Physics, Lund University, 2019).

[115] B. E. A. Saleh and M. C. Teich, *Fundamentals of photonics*, 2nd, Chapter: Fourier Optics (Wiley, Hoboken, NJ, USA, 2007) Chap. Fourier Optics, pp. 121–127.

[116] F. Campi, H. Coudert-Alteirac, M. Miranda, L. Rading, B. Manschwetus, P. Rudawski, A. L'Huillier, and P. Johnsson, «Design and test of a broadband split-and-delay unit for attosecond xuv-xuv pump-probe experiments», Review of Scientific Instruments **87** (2016).

[117] H. Coudert-Alteirac, «Spatial and temporal metrology of intense attosecond pulses», PhD thesis (Lund University, 2018).

[118] H. Wolter, «Spiegelsysteme streifenden einfalls als abbildende optiken für röntgenstrahlen», Annalen der Physik **445**, 94 (1952).

[119] B. Henke, E. Gullikson, and J. Davis, «X-ray interactions: photoabsorption, scattering, transmission, and reflection at e=50-30000 ev, z=1-92», Atomic Data and Nuclear Data Tables **54**, 181 (1993).

[120] Thales SESO, *Wolter 75° System Inspection Report*, Inspection Report, Unpublished technical report (Thales SESO, Feb. 2013).

[121] A. T. Eppink and D. H. Parker, «Velocity map imaging of ions and electrons using electrostatic lenses: application in photoelectron and photofragment ion imaging of molecular oxygen», Review of Scientific Instruments **68**, 3477 (1997).

[122] L. Rading, J. Lahl, S. Maclot, F. Campi, H. Coudert-Alteirac, B. Oostenrijk, J. Peschel, H. Wikmark, P. Rudawski, M. Gisselbrecht, and P. Johnsson, «A versatile velocity map ion-electron covariance imaging spectrometer for high-intensity xuv experiments», Applied Sciences **8**, `10 . 3390 / app8060998` (2018).

[123] U. Even, «The even-lavie valve as a source for high intensity supersonic beam», EPJ Techniques and Instrumentation **2**, 1 (2015).

[124] U. Even, «Pulsed supersonic beams from high pressure source: simulation results and experimental measurements», Advances in Chemistry **2014**, 636042 (2014).

[125] *Hitachi aberration-corrected concave gratings for flat-field spectrographs*, `https://www.hitachi-hightech.com/products/images/9797/ana-grating_05.pdf`, Product Data Sheet: Hitachi 001-0639.

[126] S. Bajt, J. B. Alameda, T. W. Barbee Jr, W. M. Clift, J. A. Folta, B. Kaufmann, and E. A. Spiller, «Improved reflectance and stability of mo-si multilayers», Optical engineering **41**, 1797 (2002).

[127] A.-S. Morlens, R. López-Martens, O. Boyko, P. Zeitoun, P. Balcou, K. Varjú, E. Gustafsson, T. Remetter, A. L'Huillier, S. Kazamias, et al., «Design and characterization of extreme-ultraviolet broadband mirrors for attosecond science», Optics letters **31**, 1558 (2006).

[128] C. Bourassin-Bouchet, Z. Diveki, S. de Rossi, E. English, E. Meltchakov, O. Gobert, D. Guénot, B. Carre, F. Delmotte, P. Salières, et al., «Control of the attosecond synchronization of xuv radiation with phase-optimized mirrors», Optics express **19**, 3809 (2011).

[129] C. Bourassin-Bouchet, S. de Rossi, and F. Delmotte, in *Optical technologies for extreme-ultraviolet and soft x-ray coherent sources*, edited by F. Canova and L. Poletto (Springer Berlin Heidelberg, Berlin, Heidelberg, 2015) Chap. 8, pp. 151–173.

[130] National Institute of Standards and Technology (NIST), *Aluminum oxide euv photodetector transfer standard*, Accessed: 2025-01-16, 2015, `https://www.nist.gov/laboratories/tools-instruments/aluminum-oxide-euv-photodetector-transfer-standard`.

[131] National Institute of Standards and Technology, *Calibration report calib1355*, tech. rep. CALIB1355, Unpublished (National Institute of Standards and Technology (NIST), May 2016).

[132] Andor Technology Ltd., *Ikon-l so ccd camera*, `https://andor.oxinst.com/products/high-energy-detection/ikon-l-so`, Accessed: 2025-01-06.

[133] S. Kühn, M. Dumergue, S. Kahaly, S. Mondal, M. Füle, T. Csizmadia, B. Farkas, B. Major, Z. Várallyay, E. Cormier, et al., «The eli-alps facility: the next generation of attosecond sources», Journal of Physics B: Atomic, Molecular and Optical Physics **50**, 132002 (2017).

[134] M. Hoflund, J. Peschel, M. Plach, H. Dacasa, K. Veyrinas, E. Constant, P. Smorenburg, H. Wikmark, S. Maclot, C. Guo, C. Arnold, A. L'Huillier, and P. Eng-Johnsson, «Focusing properties of high-order harmonics», Ultrafast Science, 10.34133/2021/9797453 (2021).

[135] V. Lakshminarayanan and A. Fleck, «Zernike polynomials: a guide», Journal of Modern Optics **58**, 545 (2011).

[136] K. Niu and C. Tian, «Zernike polynomials and their applications», Journal of Optics **24**, 123001 (2022).

[137] R. Weissenbilder, S. Carlström, L. Rego, C. Guo, C. Heyl, P. Smorenburg, E. Constant, C. Arnold, and A. L'huillier, «How to optimize high-order harmonic generation in gases», Nature Reviews Physics **4**, 713 (2022).

[138] B. Major, K. Kovács, E. Svirplys, M. Anus, O. Ghafur, K. Varjú, M. Vrakking, V. Tosa, and B. Schütte, «High-order harmonic generation in a strongly overdriven regime», Physical Review A **107**, 023514 (2023).

[139] M. Kretschmar, E. Svirplys, M. Volkov, T. Witting, T. Nagy, M. J. Vrakking, and B. Schütte, «Compact realization of all-attosecond pump-probe spectroscopy», Science Advances **10**, eadk9605 (2024).

[140] A. L'Huillier, P. Balcou, S. Candel, K. J. Schafer, and K. C. Kulander, «Calculations of high-order harmonic-generation processes in xenon at 1064 nm», Physical Review A **46**, 2778 (1992).

[141] P. Agostini, F. Fabre, G. Mainfray, G. Petite, and N. K. Rahman, «Free-free transitions following six-photon ionization of xenon atoms», Physical Review Letters **42**, 1127 (1979).

[142] W. Becker, F. Grasbon, R. Kopold, D. Milošević, G. Paulus, and H. Walther, in *Advances in atomic, molecular, and optical physics*, Vol. 48 (Elsevier, 2002), pp. 35–98.

[143] G. Paulus, W. Nicklich, H. Xu, P. Lambropoulos, and H. Walther, «Plateau in above threshold ionization spectra», Physical review letters **72**, 2851 (1994).

[144] L. Dimauro and P. Agostini, in *Advances in atomic, molecular, and optical physics*, Vol. 35 (Elsevier, 1995), pp. 79–120.

[145] F. Krausz and M. Ivanov, «Attosecond physics», Reviews of modern physics **81**, 163 (2009).

[146] B. Yang, K. Schafer, B. Walker, K. Kulander, P. Agostini, and L. DiMauro, «Intensity-dependent scattering rings in high order above-threshold ionization», Physical review letters **71**, 3770 (1993).

[147] M. P. Hertlein, P. H. Bucksbaum, and H. Muller, «Evidence for resonant effects in high-order ati spectra», Journal of Physics B: Atomic, Molecular and Optical Physics **30**, L197 (1997).

[148] R. Kopold, W. Becker, and M. Kleber, «Quantum path analysis of high-order above-threshold ionization», Optics communications **179**, 39 (2000).

[149] S. Goreslavski, G. Paulus, S. Popruzhenko, and N. Shvetsov-Shilovski, «Coulomb asymmetry in above-threshold ionization», Physical review letters **93**, 233002 (2004).

[150] M. Li, J.-W. Geng, H. Liu, Y. Deng, C. Wu, L.-Y. Peng, Q. Gong, and Y. Liu, «Classical-quantum correspondence for above-threshold ionization», Physical review letters **112**, 113002 (2014).

[151] H. Offerhaus, C. Nicole, F. Lepine, C. Bordas, F. Rosca-Pruna, and M. Vrakking, «A magnifying lens for velocity map imaging of electrons and ions», Review of scientific instruments **72**, 3245 (2001).

[152] M. J. Vrakking, «An iterative procedure for the inversion of two-dimensional ion/photoelectron imaging experiments», Review of Scientific Instruments **72**, 4084 (2001).

[153] V. Dribinski, A. Ossadtchi, V. A. Mandelshtam, and H. Reisler, «Reconstruction of abel-transformable images: the gaussian basis-set expansion abel transform method», Review of Scientific Instruments **73**, 2634 (2002).

[154] G. A. Garcia, L. Nahon, and I. Powis, «Two-dimensional charged particle image inversion using a polar basis function expansion», Review of Scientific Instruments **75**, 4989 (2004).

[155] D. D. Hickstein, S. T. Gibson, R. Yurchak, D. D. Das, and M. Ryazanov, «A direct comparison of high-speed methods for the numerical abel transform», Review of Scientific Instruments **90** (2019).

[156] National Institute of Standards and Technology (NIST), *NIST Standard Reference Database 108*, Summarized Data. Last Update: November 2013, 2013, `https://dx.doi.org/10.18434/T4FW23`.

[157] K. Klünder, J. Dahlström, M. Gisselbrecht, T. Fordell, M. Swoboda, D. Guenot, P. Johnsson, J. Caillat, J. Mauritsson, A. Maquet, et al., «Probing single-photon ionization on the attosecond time scale», Physical Review Letters **106**, 143002 (2011).

[158] E. Toma and H. Muller, «Calculation of matrix elements for mixed extreme-ultraviolet–infrared two-photon above-threshold ionization of argon», Journal of Physics B: Atomic, Molecular and Optical Physics **35**, 3435 (2002).

[159] J. G. C. M. Peschel, «Atomic and molecular dynamics probed by intense extreme ultraviolet pulses», PhD thesis (Lund University, 2021).

[160] J. Cooper and R. N. Zare, «Angular distribution of photoelectrons», The Journal of chemical physics **48**, 942 (1968).

[161] K. L. Reid, «Photoelectron angular distributions», Annual review of physical chemistry **54**, 397 (2003).

[162] E. Arnous, S. Klarsfeld, and S. Wane, «Angular distribution in the two-quantum atomic photoeffect», Physical Review A **7**, 1559 (1973).

[163] J. Peschel, D. Busto, M. Plach, M. Bertolino, M. Hoflund, S. Maclot, J. Vinbladh, H. Wikmark, F. Zapata, E. Lindroth, et al., «Attosecond dynamics of multi-channel single photon ionization», Nature Communications **13**, 5205 (2022).

[164] E. Prat, A. Malyzhenkov, C. Arrell, P. Craievich, S. Reiche, T. Schietinger, and G. Wang, «Coherent sub-femtosecond soft x-ray free-electron laser pulses with nonlinear compression», APL Photonics **8** (2023).

[165] P. K. Maroju, C. Grazioli, M. Di Fraia, M. Moioli, D. Ertel, H. Ahmadi, O. Plekan, P. Finetti, E. Allaria, L. Giannessi, et al., «Attosecond pulse shaping using a seeded free-electron laser», Nature **578**, 386 (2020).

[166] B. Bergues, D. Rivas, M. Weidman, A. Muschet, W. Helml, A. Guggenmos, V. Pervak, U. Kleineberg, G. Marcus, R. Kienberger, et al., «Tabletop nonlinear optics in the 100-ev spectral region», Optica **5**, 237 (2018).

[167] I. Makos, I. Orfanos, A. Nayak, J. Peschel, B. Major, I. Liontos, E. Skantzakis, N. Papadakis, C. Kalpouzos, M. Dumergue, et al., «A 10-gigawatt attosecond source for non-linear xuv optics and xuv-pump-xuv-probe studies», Scientific reports **10**, 3759 (2020).

[168] J. Bizau and F. Wuilleumier, «Redetermination of absolute partial photoionization cross sections of he and ne atoms between 20 and 300 ev photon energy», Journal of electron spectroscopy and related phenomena **71**, 205 (1995).

[169] A. Sorokin, M. Wellhöfer, S. Bobashev, K. Tiedtke, and M. Richter, «X-ray-laser interaction with matter and the role of multiphoton ionization: free-electron-laser studies on neon and helium», Physical Review A—Atomic, Molecular, and Optical Physics **75**, 051402 (2007).

[170] J. Feist, S. Nagele, R. Pazourek, E. Persson, B. I. Schneider, L. A. Collins, and J. Burgdörfer, «Probing electron correlation via attosecond xuv pulses in the two-photon double ionization of helium», Physical review letters **103**, 063002 (2009).

[171] F. Vismarra, M. Fernández-Galán, D. Mocci, L. Colaizzi, V. W. Segundo, R. Boyero-García, J. Serrano, E. Conejero-Jarque, M. Pini, L. Mai, et al., «Isolated attosecond pulse generation in a semi-infinite gas cell driven by time-gated phase matching», Light: Science & Applications **13**, 197 (2024).

[172] J. R. Sutherland, E. Christensen, N. Powers, S. Rhynard, J. Painter, and J. Peatross, «High harmonic generation in a semi-infinite gas cell», Optics Express **12**, 4430 (2004).

[173] Y. Duann, L. C. Chang, C.-Y. Lin, Y.-C. Hsieh, Y.-C. Wen, C. C. Lin, and J.-Y. Liu, «A methodology of retrieving volume emission rate from limb-viewed airglow emission intensity by combining the techniques of abel inversion and deep learning», Atmosphere **14**, 74 (2022).

[174] `https://www.youtube.com/watch?v=dQw4w9WgXcQ`.

Author Contributions

Paper I: Spatial Aberrations in High-Order Harmonic Generation

This paper investigates the impact of astigmatism in the driving laser on the far-field profile of HHG, using a Gaussian model to describe the harmonic dipole phase (γ-model) to simulate experimental observations. We demonstrate that aberrations can be corrected, highlighting the importance of precise control over the driving laser wavefront.

I contributed to building the setup, implementing and conducting the measurements and analyzing the data. I contributed to the writing, and creating the figures. This work was conducted in close collaboration with F. Vismarra, with whom I share first authorship.

Paper II: Chromatic aberrations correction of attosecond high-order harmonic beams by flat-top spatial shaping of the fundamental beam

This paper examines the influence of flat-top driving lasers on chromatic aberrations in high-order harmonics by measuring the intensity and wavefront of individual harmonic orders near refocusing for Gaussian and flat-top intensity profiles. Experimental results are compared with TDSE-based simulations, demonstrating that chromatic aberrations are reduced with flat-top drivers compared to Gaussian drivers.

I contributed to building the setup, conducting the measurements, and participated in writing, figure creation, and revising the manuscript. This publication represents a shared first authorship with K. Veyrinas.

Paper III: Focusing Properties of High-Order Harmonics

This paper determines the waist and position of harmonic foci using a knife-edge technique and investigates how the generation position (i.e., the laser focus relative to the gas medium) influences these parameters. Measurements are compared with simulations based on the γ-model. It is demonstrated that chromatic aberrations upon refocusing are minimized when the generation medium is located at or beyond the laser focus.

I contributed to setting up and performing the measurements and participated in writing the article and creating a figure.

Paper IV: Two phase-matching regimes in high-order harmonic generation

This study explores the relationship between gas pressure, medium length, and harmonic yield, identifying two regimes that favor efficient HHG. Experimental results from the Intense XUV Beamline in Lund and the SYLOS GHHG Long beamline at ELI-ALPS in Szeged are compared to macroscopic propagation simulations to evaluate phase matching.

I contributed to building the setup and conducting measurements at the Intense XUV Beamline in Lund. I also participated in beamtime at ELI-ALPS, manuscript discussions, and created a figure of the experimental setup.

Paper V: Attosecond dynamics of multi-channel single photon ionization

This publication investigates the phase and amplitude of angular momentum channels in neon's outer-shell photoionization using two-photon RABBIT interferometry. It reveals the effects of channel interference and short-range, Coulomb, and centrifugal potentials on photoionization dynamics.

I contributed to building the setup, performing the experiments, and participated in scientific discussions during the writing of the article.

Part II: Publications

Printed by Media-Tryck, Lund 2025 NORDIC SWAN ECOLABEL 3041 0903

Faculty of Engineering, LTH
Department of Physics

Lund Reports on Atomic Physics, LRAP 607 (2025)
ISBN 978-91-8104-396-9
ISSN 0281-2762